Electronic order

Topology in crystals and symmetry-breaking from interactions

Henke, J.G.B.

Publication date
2022

Document Version
Final published version

ELECTRONIC ORDER

TOPOLOGY IN CRYSTALS AND SYMMETRY-BREAKING FROM INTERACTIONS

JANS HENKE

Electronic order:
Topology in crystals and symmetry-breaking from interactions

ACADEMISCH PROEFSCHRIFT

ter verkrijging van de graad van doctor

aan de Universiteit van Amsterdam

op gezag van de Rector Magnificus

prof. dr. ir. K.I.J. Maex

ten overstaan van een door het College voor Promoties ingestelde commissie,

in het openbaar te verdedigen in de Agnietenkapel

op woensdag 18 mei 2022, te 13.00 uur

door Jans Ganga Bahini Henke

geboren te Nijmegen

Promotiecommissie

Promotor:	dr. J. van Wezel	Universiteit van Amsterdam
Copromotor:	prof. dr. M.S. Golden	Universiteit van Amsterdam
Overige leden:	prof. dr. N.E. Hussey	Radboud Universiteit
	dr. F. Flicker	Cardiff University
	dr. F.K. Kunst	Max Planck Institute for the Science of Light
	dr. A. Isaeva	Universiteit van Amsterdam
	dr. A. de Visser	Universteit van Amsterdam
	prof. dr. P.R. Corboz	Universiteit van Amsterdam
	prof. dr. J.S. Caux	Universiteit van Amsterdam

Faculteit der Natuurwetenschappen, Wiskunde en Informatica

Ph.D. Thesis, University of Amsterdam, 2022
Electronic order: Topology in crystals and symmetry-breaking from interactions
Jans Henke

Cover design by Jans Henke.

ISBN 978-90-832468-0-2

The work described in this thesis was performed between January 2018 and February 2022 at the University of Amsterdam, Science Park 104, 1098 XH Amsterdam, the Netherlands.

A digital version of this thesis is available at https://dare.uva.nl/.

List of publications

This thesis includes work described in three publications, listed below in order of appearance:

J. Henke, M. Kurttutan, J. Kruthoff, and J. van Wezel, *Topological invariants of rotationally symmetric crystals*, Phys. Rev. B **104**, L201110 (2021).

J. Henke, F. Flicker, J. Laverock, and J. van Wezel, *Charge order from structured coupling in VSe_2*, SciPost Phys. **9**, 56 (2020).

R. Chua, J. Henke, S. Saha, Y. Huang, J. Gou, X. He, T. Das, J. van Wezel, A. Soumyanarayanan, and A. T. S. Wee, *Coexisting charge-ordered states with distinct driving mechanisms in monolayer VSe_2*, ACS Nano **16**, 783–791 (2022).

These form the basis of Chapters 3, 5 and 6, respectively.

Other publications by the author are listed below, in reverse chronological order:

X. Guo, A. Kogar, J. Henke, S. X.-L. Sun, I. Khayr, Y. Peng, S. Lee, M. J. Krogstad, D. Robinson, S. Rosenkranz, R. Osborn, J. P. C. Ru, D. B. Lioi, G. Karapetrov, D. J. Campbell, J. Paglione, J. van Wezel, T.-C. Chiang, and P. Abbamonte, *In-plane anisotropy of charge density wave fluctuations in $1T$-$TiSe_2$*, in preparation (2022).

X. Feng, J. Henke, C. Morice, C. J. Sayers, E. Da Como, J. van Wezel, and E. van Heumen, *Signatures of the charge density wave collective mode in the infrared optical response of VSe_2*, Phys. Rev. B **104**, 165134 (2021).

S. V. Ramankutty, J. Henke, A. Schiphorst, R. Nutakki, S. Bron, G. Araizi-Kanoutas, S. K. Mishra, L. Li, Y. K. Huang, T. K. Kim, M. Hoesch, C. Schlueter, T. L. Lee, A. de Visser, Z. Zhong, J. van Wezel, E. van Heumen, and M. S. Golden, *Electronic structure of the candidate 2D Dirac semimetal $SrMnSb_2$: a combined experimental and theoretical study*, SciPost Phys. **4**, 010 (2018).

A. Nikitin, V. Grinenko, R. Sarkar, J.-C. Orain, M. Salis, J. Henke, Y. Huang, H.-H. Klauss, A. Amato, and A. de Visser, *Macroscopic phase separation of superconductivity and ferromagnetism in $Sr_{0.5}Ce_{0.5}FBiS_{2-x}Se_x$ revealed by μSR*, Sci. Rep. **7**, 1–7 (2017).

S. de Haro, J. Henke, and D. Tang, *A. Cappelli, E. Castellani, F. Colomo and P. Di Vecchia (Eds.): The Birth of String Theory*, Found. Phys. **45**, 657–660 (2015).

Contents

1

Introduction

Electrons in a piece of material are very different from their lonesome counterparts considered in particle physics. In being surrounded by billions of other electrons and atomic cores, they may change their effective mass, charge, and spin. More interestingly, along the lines of the Aristotelian cliché that the whole is greater than the sum of its parts, the collective behaviour of electrons (and atoms) is much richer than that of the individual particles. All electronics used today rely on this collective behaviour, and society is always on the look-out for new functional devices which are more efficient, smaller, and/or have new functionalities. This is one of the motivations for the multitude of research in spintronics [10–13], functional heterostructures [14–16], multiferroics [17–24], and high-temperature superconductivity [25–31]. Importantly, interesting electronic phases of matter can be found even in the absence of more exotic features like magnetism or superconductivity.

All of these functional phases are demonstrated most clearly in materials with a nicely ordered atomic structure, called crystals. In this thesis, we ask the fundamental question of what the effect is of the interplay between electrons and the atomic lattice they reside in. What types of electronic order do they induce?

In Part I, we delve into how the symmetries of a crystal determine how electronic wavefunctions can be 'twisted' into distinct configurations, and allow for exotic phases with symmetry-protected electron states that are bound to the edges or corners of the material. These states are determined by the inherent topology of the system, something that will be explained in detail in Chapter 2. At present, the field of topology in condensed matter is edging towards completing the full topological classification of crystalline insulators, including the topological phases stabilised by lattice symmetries. While at this point it is known how many topological phases are possible, we still have not found a way to distinguish between all of them. In Chapter 3, we present a unifying

framework with which we believe all crystalline topological invariants may be identified. We demonstrate it for two-dimensional insulators with three-fold rotational symmetry, and discuss the generalisation of our method to other crystal symmetries.

In Part II, we move away from topological insulators and instead consider how the interactions between electrons and the crystal lattice they reside in can lead to symmetry-breaking ordered electronic phases. In these phases, valence electrons spontaneously form standing waves called *charge density waves* (CDWs), with wavelengths on the order of a few lattice parameters. The interactions between the electrons and the lattice result in the electrons overcoming their mutual Coulombic repulsion, something you'd never expect for the bare electrons discussed in particle physics. Upon the transition to a CDW state, materials change their atomic structure and their conductivity, which may be relevant for applications. In Chapter 4 we introduce the most common mechanism driving charge order, and demonstrate the limitations of the conventional wisdom in this field, which is primarily derived from a simple, one-dimensional toy model. We also introduce a generally applicable field-theoretical method for describing charge order, which we use in Chapters 5 and 6 to analyse the CDWs in the real material VSe_2.

Whether crystal symmetries are tying electronic states into topological knots, or electrons interacting with the lattice break symmetries by settling into a joint ground state, it is the unique environment provided by the crystal that allows for electronic order on a macroscopic scale. Conceptually, this is a beautiful manifestation of quantum mechanics made noticable on a large scale by symmetry. More practically, almost all 'useful' electronic phases of matter that may lead to novel functional devices also rely on a crystalline environment. Understanding the more complex phases of matter arising in the presence of multiple types of interactions starts with understanding how to tackle the most fundamental types of order arising from the interplay between electrons and the lattice: topology and charge order.

I

Lattice symmetries and topology

2

Introduction to topology

Topology studies whether objects can be transformed continuously into each other. In the field of geometry, one can imagine objects made out of a soft clay; in this case, 'continuous transformations' include squeezing and indenting the clay, but not sticking two parts together or poking a hole through it.[1] In this way, a ball and a bowl are topologically equivalent, because indenting the ball transforms it into a bowl shape. This is different from a mug, because forming the ear of the mug requires forming a hole in the clay. Because changing the number of holes can only be done by what we define to be a non-continuous transformation, we can distinguish between different topological phases of clay objects by counting the number of holes they have; this number constitutes a *topological invariant*. Note that an invariant is necessarily something countable, or quantised, because this enforces that one cannot go smoothly from one topological phase to another.

In the context of quantum physics, we can instead ask whether the Hamiltonians of two quantum systems are topologically equivalent. As a simple example, consider a small, 'zero-dimensional' quantum object[2] with N electronic energy levels. Its Hamiltonian is then an $N \times N$ matrix that is Hermitian ($H = H^\dagger$) whose real eigenvalues E_n correspond to the allowed electron energies:

$$H\,|n\rangle = E_n\,|n\rangle\,, \tag{2.1}$$

with corresponding eigenstates $|n\rangle$. Since these are electronic states, they can only host a single electron of each spin type,[3] and at zero temperature the electronic states will be occupied until the Fermi energy E_F. We can compare

[1] Transformations that leave the shape of an object intact – such as rotating it in space, or even reflecting it in a mirror – also leave the topology unchanged.

[2] This could be an atom, molecule, or quantum dot.

[3] We do not explicitly include the spin label here, but assume that n counts all individual states for both spins; an atom with M atomic orbitals will have $N = 2M$ states.

the Hamiltonian of one such quantum object to the Hamiltonian of another with the same total number of states. One way to topologically distinguish the two systems is to simply count the number of occupied states, *i.e.* the number of states below E_{F}. Changing the number of occupied states in an isolated quantum system entails adding or removing electrons, something that we do not consider to be a continuous transformation. In contrast, any changes in positions of energy levels that do not cross E_{F} do not change the topological phase.

What distinguishes condensed matter physics from pure quantum mechanics is that the systems we consider consist of many particles. This allows for much richer (topological) structures, because the systems in question may have internal symmetries that strongly affect the structure of the electronic states. Importantly, the atoms in crystalline materials are arranged in a periodic lattice. This means crystals are translationally symmetric in a discrete manner: shifting the whole material by one unit cell returns the exact same atomic structure. Energy eigenstates for an electron in a crystalline lattice can be described by Bloch states:

$$|\psi_{n\mathbf{k}}(\mathbf{r})\rangle = e^{i\mathbf{k}\cdot\mathbf{r}}\,|u_{n\mathbf{k}}(\mathbf{r})\rangle \tag{2.2}$$

where $|u_{n\mathbf{k}}(\mathbf{r})\rangle$ is a periodic function with the same periodicity as the lattice, n is the electronic band index, and $\mathbf{k}$ is the crystal momentum which arises from taking the Fourier transform of the real-space position [32]. Notably, $|\psi_{n\mathbf{k}}(\mathbf{r})\rangle = |\psi_{n\mathbf{k}}(\mathbf{r}+\mathbf{R})\rangle$, where $\mathbf{R}$ is a lattice vector. The Bloch states $|\psi_{n\mathbf{k}}(\mathbf{r})\rangle$ are eigenstates of the Bloch Hamiltonian $h(\mathbf{k})$.[4] Rather than a series of energy levels labelled only by n, the electronic states in a crystal may now also vary as a function of $\mathbf{k}$. Correspondingly, the eigenvalues of $h(\mathbf{k})$ define n energy bands ($E_n(\mathbf{k})$) that collectively form a periodic-in-$\mathbf{k}$ band structure. In direct analogy with the zero-dimensional quantum systems discussed before, we could use the number of occupied bands as a topological invariant, as long as no band crosses E_{F} for any $\mathbf{k}$. In this case, we say that the electronic spectrum is gapped, and the material is an insulator. While there is much to be said about the topology of metals (see *e.g.* [33]), we will only discuss insulating systems in this Part of the thesis.

At this point, topology might seem like a rather abstract concept that is either trivial or something that only mathematicians may need to worry about. However, we will see in this chapter that topology in condensed matter systems can have very real and physical concequences. There are two main reasons for this. First, what we have not considered thus far is the phase that any quantum-mechanical state may have. This is an inherent gauge freedom in quantum mechanics; adding a phase factor to any Bloch state $e^{i\theta}\,|\psi_{n\mathbf{k}}(\mathbf{r})\rangle$ will not change the associated eigenenergy $E_n(\mathbf{k})$. While this is generally in-

[4] We use a lower-case 'h' for the Bloch Hamiltonian to distinguish it from the full Hamiltonian, which includes a sum over all crystal momenta $\mathbf{k}$. Throughout this thesis, we will denote vectors in **bold**.

consequential for single particles,[5] the periodicity of the crystal momentum can enforce certain restrictions on the variation of this phase, which in turn determine the allowed topological phases. Second, there may be symmetries present that pose additional constraints on the electronic band structure and the associated eigenvectors. These, in turn, determine how many different topological phases there are, in the sense that topologically distinct Hamiltonians cannot be continuously transformed into one another; in this case, continuous transformations are those that do not close the energy gap at E_{F} nor break a symmetry of the Hamiltonian. A topologically non-trivial insulating crystal is called a *topological insulator*. Excitingly, when two finite-sized crystals with different topological indices are brought together, the difference in topology may enforce a local gap closing at the interface between them. These interface states are then topologically *protected* by the symmetries of the two crystals. The same holds for a topological insulator coming in contact with the (always topologically trivial) vacuum.

In the following sections, we will elucidate this step by step. First, in Section 2.1 we introduce the concepts of a Berry connection and Berry curvature. We will use these concepts to define the Chern number, which is perhaps the most famous topological invariant, and is related to the Integer Quantum Hall Effect (IQHE) and the Quantum Anomalous Hall Effect (QAHE). In Section 2.2, we describe how time-reversal, particle-hole and chiral symmetries prescribe the famous 'tenfold way' classification of topological insulators and superconductors. In Section 2.3 we explain how to generalise the Chern number to time-reversal invariant systems. Lastly, in Section 2.4 we discuss the additional constraints imposed by lattice symmetries, and the classification scheme derived in refs. [35, 36].

Before moving on, we would like to give a shout out to ref. [37], which offers an excellent pedagogical introduction to topology in condensed matter, and which inspired much of this chapter. Aside from this, refs. [38–40] are also excellent introductory resources on topological insulators and the concept of the Berry connection.

2.1. The Berry connection

A central concept of topology in condensed matter systems, and one that makes a direct link to the mathematical field of algebraic topology, is that of a geometric phase. This is a purely path-dependent type of phase factor that an object acquires when adiabatically transported over a cycle in parameter space. A simple classical example of this phenomenon can be seen by considering a vector tangential to the surface of a sphere. Taking a path where the vector is moved – without rotating with respect to the surface – from the north pole to the equator, then moving one fourth of the way along the equator, and then back to the north pole, the vector will have rotated by 90° in the tangent plane

[5] With the exception of some interference effects such as that of Aharonov-Bohm [34].

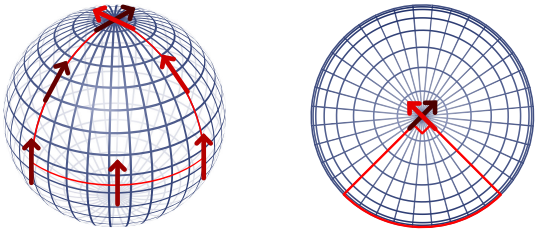

Figure 2.1: A classical example of a geometric phase. Parallel transporting a tangent vector (dark red to red arrows) along the surface of the sphere along a closed path (red curves) will rotate it by a Hannay angle (90° in this example). The right image shows the top view of the left image, with the initial and final arrows showing. The left sphere wireframe is taken from [42].

(see Figure 2.1). You can try this yourself by holding out your arm with your thumb pointing perpendicular to your arm; rotating your arm from the shoulder in a closed loop allows you to rotate the direction of your thumb without ever moving your wrist or elbow. The angle rotated over is called the *Hannay angle* [41]. In general, it captures the curvature enclosed by the path of a parallel transported tangential vector on any closed manifold living in $\mathbb{R}^3$. What the vectors and manifold represent physically depends on the system at hand.

In fact, the classical Hannay angle was described only *after* the discovery of the quantum-mechanical geometric phase known as the *Berry phase*.[6] As already mentioned above, quantum-mechanical eigenvectors are only defined up to a phase. While this phase amounts to a gauge freedom, a geometric phase may be found when a quantum state is adiabatically transported over a closed cycle. In this sense, Bloch states are interesting because they are defined in $\mathbf{k}$-space, which happens to be a periodic, closed manifold. The 'unit cell' of this space is called the Brillouin zone (BZ). We can identify the BZ with a circle in spatial dimension $d = 1$; a torus in $d = 2$; and a hypertorus in $d = 3$. If you vary a single component of $\mathbf{k}$ far enough, you will necessarily return to a point that is equivalent to your starting location: you will have made a closed loop. Below, we will demonstrate how this leads to a Berry phase, largely following the derivation in ref. [40].

To begin with, imagine moving along a path in $\mathbf{k}$-space in a single, isolated band $E_n(\mathbf{k})$. If we divide the path up into small enough step sizes $d\mathbf{k}$, the overlap between neighbouring Bloch states along this path is approximately unity times a phase factor corresponding to the phase difference of the states $\Delta\theta$:

$$e^{-i\Delta\theta} = \langle u_n(\mathbf{k}_1)|u_n(\mathbf{k}_2)\rangle, \tag{2.3}$$

[6] The quantum-mechanical geometric phase is commonly known as the Berry phase or Zak phase, as it was described by Berry in 1984 in the context of a quantum particle travelling adiabatically through (real) space [43], and first applied to the context of crystalline materials by Zak, a few years later [44]. However, the phenomenon of a geometric phase had already been independently discovered many years earlier by Kato in 1950 [45], Pancharatnam in 1956 [46] and Longuet-Higgins *et al.* in 1958 [47].

where $\mathbf{k}_2 = \mathbf{k}_1 + d\mathbf{k}$. This becomes exact in the continuum limit, where $d\mathbf{k} \to 0$ or equivalently the number of steps along the path taken goes to infinity. The above quantity is gauge-dependent, but if the path we consider is a closed loop, any gauge-dependent phases will cancel out and only a gauge-independent, geometric phase (γ) may remain:

$$e^{i\gamma_n} = \prod_{l=1}^{L} e^{-i\Delta\theta_l} = \prod_{l=1}^{L} \langle u_n(\mathbf{k}_l)|u_n(\mathbf{k}_{l+1})\rangle, \tag{2.4}$$

where $\mathbf{k}_1 = \mathbf{k}_{L+1}$ up to a reciprocal lattice vector. We include the minus sign to stay in line with the convention used in [40].

To obtain the geometric phase itself, we must take the log of Equation 2.4. Let us first do this for a single element of the discrete product above. We take the continuum limit, and parameterise the wavevectors in the path by a real-valued parameter λ, such that $|u_n(\lambda)\rangle$ traverses the path as λ evolves from 0 to 1. We assume that $|u_n(\lambda)\rangle$ are smooth and differentiable functions of λ. Then, we can Taylor expand the log of a single inner product as follows:

$$\begin{aligned} \ln \langle u_n(\lambda)|u_n(\lambda + d\lambda)\rangle &= \ln \langle u_n(\lambda)| \left(|u_n(\lambda)\rangle + d\lambda \frac{d\,|u_n(\lambda)\rangle}{d\lambda} + \mathcal{O}(d\lambda^2) \right) \\ &= \ln \left(1 + d\lambda \,\langle u_n(\lambda)|\, \partial_\lambda |u_n(\lambda)\rangle + \mathcal{O}(d\lambda^2) \right) \\ &= d\lambda \,\langle u_n(\lambda)|\, \partial_\lambda |u_n(\lambda)\rangle + \mathcal{O}(d\lambda^2). \end{aligned} \tag{2.5}$$

In taking the continuum limit, all terms of second order and higher in $d\lambda$ can be discarded. We used that to first order, $\ln(1+x) = x$. What we have derived is that the imaginary part of the log of a single inner product in Equation 2.4 is equal to

$$\mathbf{A}_n(\mathbf{k}) = -\mathrm{Im}\left[\langle u_n(\mathbf{k})|\, \nabla_{\mathbf{k}}\, |u_n(\mathbf{k})\rangle \right] = i \,\langle u_n(\mathbf{k})|\, \nabla_{\mathbf{k}}\, |u_n(\mathbf{k})\rangle\,, \tag{2.6}$$

now written in its general vector-form. This is known as the *Berry connection*. 'Connection' is a term taken from differential geometry, but $\mathbf{A}(\mathbf{k})$ can also be interpreted as a vector potential in analogy to the one known from electromagnetism. We can also write $\mathbf{A}_n(\mathbf{k})$ back in terms of a set of discrete steps, as

$$\mathbf{A}_n(\mathbf{k}) = \lim_{d\mathbf{k}\to 0} i\, \frac{\langle u_n(\mathbf{k})|u_n(\mathbf{k}+d\mathbf{k})\rangle - \langle u_n(\mathbf{k})|u_n(\mathbf{k})\rangle}{d\mathbf{k}}. \tag{2.7}$$

In terms of this potential, the geometric phase is given by the closed-loop integral

$$\gamma_n = \oint_{\mathcal{C}} \mathbf{A}_n(\mathbf{k}) \cdot d\mathbf{k}. \tag{2.8}$$

By Stokes' theorem, we can rewrite the above again as an integral over the surface enclosed by loop $\mathcal{C}$:

$$\gamma_n = \int_S \mathbf{F}_n(\mathbf{k}) \cdot d^2\mathbf{k}, \tag{2.9}$$

where the gauge-invariant field $\mathbf{F}(\mathbf{k}) = \nabla_{\mathbf{k}} \times \mathbf{A}(\mathbf{k})$ is called the *Berry curvature*. By analogy to electromagnetism, the curvature is similar to a magnetic field, and a non-zero curvature can be related to a kind of flux perpendicular to the surface integrated over. Of course, the curl is strictly only defined in three dimensions ($\mathbb{R}^3$), where $\mathbf{F}(\mathbf{k})$ is a vector. The concept of curvature does not exist for one-dimensional ($d = 1$) systems, although Equation 2.8 still applies. In two dimensions, the curvature is given by the scalar $\partial_y A_x - \partial_x A_y$ where x and y label the components of $\mathbf{k}$ and $\mathbf{A}(\mathbf{k})$; in this case, $F(\mathbf{k}) = \gamma_{\mathbf{k}}$ where the latter is calculated using Equation 2.8 for an infinitesimal loop enclosing a single $\mathbf{k}$-point.

Having defined the Berry phase, one can immediately see the connection with the classical Hannay angle: the classical tangent vector that was transported over a curved two-dimensional manifold is replaced by $\mathbf{A}(\mathbf{k})$, and the curvature of the classical manifold is replaced by the Berry curvature, which is a type of curvature within the phase of the quantum-mechanical wavefunction. From the fact that γ and $\mathbf{F}(\mathbf{k})$ are gauge-independent, it follows that they should be measurable. Any non-zero value indicates an anholonomy in the parallel transport of the vector $|u_{n\sigma}(\mathbf{k})\rangle$: when transported along a closed loop in $\mathbf{k}$-space, the state does not return to itself.[7] One can then ask the question if they can constitute a topological invariant. As already mentioned, topological invariants are necessarily quantised. A quantised Berry phase indicates that the geometric phase is only allowed to wind a certain amount across the closed loop in question; because of this, we can say that we are looking for a quantised *winding number*. In the absence of other symmetries, γ for a generic closed loop in the BZ will not be quantised.[8] However, by Chern's theorem [48], the Berry curvature integrated over a closed two-dimensional manifold such as the BZ (in $d = 2$) is necessarily quantised in units of 2π. This defines the so-called (first) *Chern number* of the n^{th} band:

$$W_n = \frac{1}{2\pi} \int_{\text{BZ}} F_n(\mathbf{k}) \cdot d^2\mathbf{k} \in \mathbb{Z}. \tag{2.10}$$

The Chern number is not just a mathematical curiosity; it also leads to physically relevant effects. Another name for it is the TKNN invariant, after Thouless, Kohmoto, Nightingale and den Nijs, who identified it as the invariant describing the number of chiral edge channels participating in (and dominating) the transport in the *Integer Quantum Hall Effect* (IQHE) [49].[9] This effect arises when a two-dimensional electron gas is placed in a strong out-of-plane magnetic field at low temperatures. It originally came as an experimental

[7] Something is anholonomic when its state depends on the path taken in order to achieve it.

[8] γ will be quantised in the presence of some symmetries. An example is inversion symmetry in a 1D crystal [44], where $\gamma_n = 0$ or π. We will discuss the role of crystal symmetries in Section 2.4.

[9] The original derivation by Thouless *et al.* was for non-interacting Bloch electrons, but it was later shown to be valid also for general multi-particle Schrödinger Hamiltonians, even in the presence of electron-electron interactions or without a lattice periodicity [50].

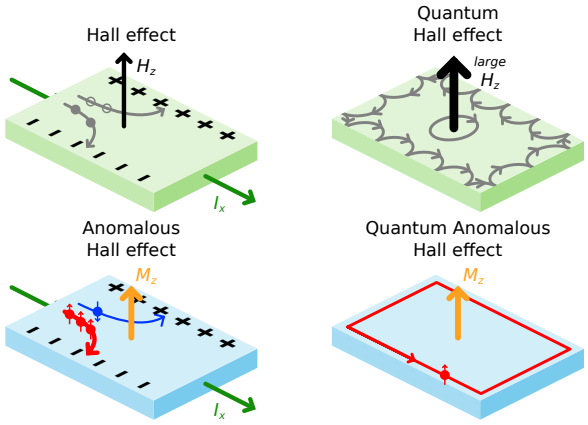

Figure 2.2: A comparison of several types of 'Hall effect' in 2D materials. The original (top left) describes the charge accumulation on opposite sides of a metal, in the presence of an out-of-plane magnetic field H_z and in-plane current I_x. The transverse Hall voltage V_y that builds up is linearly proportional to H_z. For large H_z, electrons in the bulk are localised in Landau levels, and only chiral edge currents contribute to the quantized transverse Hall conductivity σ_{xy} (top right). In magnetic materials, a Hall voltage may be induced by the intrinsic magnetisation M_z, giving the Anomalous Hall Effect (bottom left). Spin-orbit coupling in magnetic topological insulators induces the Quantum Anomalous Hall Effect (bottom right), in which quantised chiral edge currents dominate σ_{xy}.

surprise, measured by von Klitzing *et al.*, that the Hall conductance – this is the conductance perpendicular to both the magnetic field direction and the direction in which an in-plane electric field is applied to the piece of material – showed discrete steps [51]:

$$\sigma_{xy} = \frac{e^2}{h}\nu = \frac{e^2}{h}\sum_{N_{\text{occ}}} W_n. \tag{2.11}$$

Because of the strong out-of-plane magnetic field, the electronic states are no longer plane-wave-like Bloch states, instead being forced into quantised cyclotron orbits known as Landau levels. When E_{F} lies between two Landau levels, the bulk carriers are localised, but electrons can still propagate along the edges of the sample. ν describes the number of Landau levels that are occupied, or equivalently the number of chiral edge states contributing to the Hall conductance.

While the setup for von Klitzing's experiment – which requires a strong magnetic field – might seem awfully specific, the same chiral edge states may be found in 2D ferromagnetic insulators without the presence of an external magnetic field. In this case, it is called the *Quantum Anomalous Hall Effect* (QAHE). These types of topological insulators have a magnetization $\mathbf{M} = \mathbf{M}_{\text{spin}} + \mathbf{M}_{\text{orb}}$, made up of a (usually dominating) spin component which describes the excess population of spin-up versus spin-down electrons, as well as an orbital component that can be thought of (semi-classically) as arising

from the circular currents of electrons orbiting around the atoms in the crystal. The latter effect can be induced by spin-orbit coupling (SOC), with the effective form $H_{\mathrm{SOC}} = \xi \mathbf{L} \cdot \mathbf{S}$ where $\mathbf{L}$ and $\mathbf{S}$ are the orbital and spin angular momentum operators on each site. An orbital magnetisation will result in a surface current $\mathbf{I}_{\mathrm{surf}} = c\mathbf{M}_{\mathrm{orb}} \times \hat{\mathbf{n}}$, where $\hat{\mathbf{n}}$ is the surface normal and the speed of light c arises from using Gaussian units [40]. Because $\mathbf{M}_{\mathrm{orb}}$ is a well-defined bulk property of the material, the surface (or edge, in $d = 2$) currents that it generates are independent of the specific way that the crystal is cut or terminated. Additionally, we call these currents 'chiral' because the SOC enforces that electrons of opposite spin circulate the boundary in opposite directions. This feature protects the currents from back-scattering, because such a process would require flipping the electron spin. $\sum_{N_{\mathrm{occ}}} W_n$ describes the difference in the number of left- and right-circulating edge currents. We can say that the edge currents are protected by the topology of the bulk, making them robust against dissipation. This relation between a bulk and surface property is known as the *bulk-boundary correspondence*.

A famous, Nobel prize-winning two-band tight-binding model demonstrating the QAHE is the Haldane model [52]. Its mathematical simplicity has made this model a kind of 'hydrogen atom of the topological insulators' [40]. The model replaces the external magnetic field by an imaginary second-nearest-neighbour hopping on a honeycomb lattice.[10] This imaginary hopping acts like a local magnetic field: an effective M_z. In its simplest form, the second quantised Hamiltonian in real space is given by

$$H_{\mathrm{Hal}} = m \sum_i (-1)^{\tau_i} c_i^\dagger c_i + t_1 \sum_{\langle ij \rangle} \left(c_i^\dagger c_j + c_j^\dagger c_i \right) + i t_2 \sum_{\langle\langle ij \rangle\rangle} \left(c_i^\dagger c_j + c_j^\dagger c_i \right), \quad (2.12)$$

where i, j label the unit cells, m is an on-site potential known as the Haldane mass which breaks the sublattice symmetry, $\tau_i = \{1, 2\}$ is the sublattice index within the unit cell, t_1 is the nearest-neighbour hopping amplitude and t_2 the second-nearest neighbour hopping amplitude. Importantly, at the high-symmetry points $K = \frac{1}{3}\mathbf{b}_1 + \frac{2}{3}\mathbf{b}_2$ and $K' = \frac{2}{3}\mathbf{b}_1 + \frac{1}{3}\mathbf{b}_2$ with $\mathbf{b}_i$ the reciprocal lattice vectors, the contribution of t_1 to the Bloch Hamiltonian drops out, and the two states above and below E_{F} at these locations are purely of $\tau = 1$ and $\tau = 2$ character, respectively. The eigenenergies at these points are given by

$$E_{\mathbf{k}} = \pm \begin{cases} m - 3\sqrt{3} t_2 & \text{at } K \\ m + 3\sqrt{3} t_2 & \text{at } K' \end{cases} \quad (2.13)$$

from which it is clear that by tuning t_2, we can close and reopen a gap selectively at either the K or the K' point, thereby also switching the sublattice character of the states above and below E_{F}. Remember that by closing the band gap we

[10] This is the lattice of the famous 2D material graphene, and that of boron nitride. It has two atoms per unit cell, making it a bipartite lattice.

can change the topological state of our system; this kind of *band inversion* is what leads to the formation of a chiral edge state.

Despite having a theoretical understanding of the QAHE since the 1980s, it took until 2013 to experimentally realise this phase [53]. An important reason that it has proven so difficult to find material realisations of a topological Chern insulator is that it requires magnetism. 2D insulators with a ferromagnetic moment perpendicular to the plane are exceedingly rare, and the additional requirement of a strong SOC to induce a band inversion (as seen in the Haldane model) reduces the number of candidates further [54].

To conclude, we've seen that we can use the Berry connection to define a topological invariant for 2D magnetic systems which determines the number of chiral edge states that the system hosts. This explains the IQHE in strong magnetic fields as well as the QAHE ferromagnetic insulators. Most materials are not magnetic, which means they have the extra symmetry known as *time-reversal symmetry* (TRS). We cannot describe these systems with a Chern number, but we will demonstrate in Section 2.3 that a similar Berry curvature-based invariant exists for TRS systems. First, let us discuss the general effect that symmetries have on topology.

2.2. The tenfold way

Usually, one considers a Hamiltonian to have a symmetry if there is a unitary operator U that commutes with the Hamiltonian:

$$UHU^\dagger = H \qquad \text{where } UU^\dagger = UU^{-1} = 1. \tag{2.14}$$

The presence of such a symmetry implies that the Hamiltonian is subject to a conservation law, and can be broken down into a block-diagonal form. This is useful because it means we need only study a single block, reducing the dimension of the problem at hand. However, even when all unitary symmetries have been used to reduce a Hamiltonian to an *irreducible* form, there are three other types of fundamental symmetries that may impose further constraints. They are described by the following symmetry operators:

- T is an anti-unitary operator which commutes with the Hamiltonian: $THT^{-1} = H^*$
- P is an anti-unitary operator which anti-commutes with the Hamiltonian: $PHP^{-1} = -H^*$
- C is a unitary operator which anti-commutes with the Hamiltonian: $CHC^{-1} = -H$

These three fundamental symmetries have a stong influence on topology. Let us introduce them one by one, before moving on to how these define ten symmetry classes which strongly constrain topology.

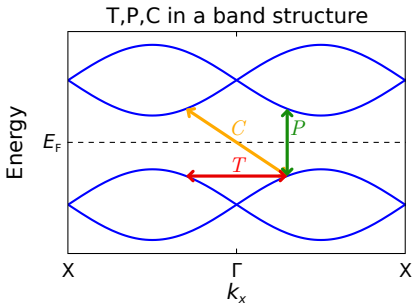

Figure 2.3: An example of an electronic band structure $E_n(k_x, 0, 0)$ with all three fundamental symmetries present: time-reversal (T), particle-hole (P) and chiral (C). E_F is the Fermi energy. On the k_x-axis we mark the high-symmetry TRIMs $\Gamma = (0, 0, 0)$ and $\mathrm{X} = (\pi/a, 0, 0)$ with lattice parameter a.

Let us consider T first, which describes the previously mentioned *time-reversal symmetry* (TRS). This symmetry operator is generically given by $T = U\mathcal{K}$, where $\mathcal{K}$ is the operator of complex conjugation. For systems of spin-half particles (like electrons), $T = i\sigma_y\mathcal{K}$ with Pauli matrix σ_y in spin space, from which it is clear that it flips the electron spin. $T^2 = -1$ for spin-half particles and $T^2 = 1$ for spinless particles. Aside from flipping the spin, T acting on a Bloch state will send $\mathbf{k}$ to $-\mathbf{k}$. However, at certain high-symmetry points in the BZ, known as time-reversal invariant momenta (TRIMs), $\mathbf{k} = -\mathbf{k}$, such that spin-up and spin-down electron states must be degenerate at these points.[11] This means that electron bands come in *Kramers pairs* (see Figure 2.3) [55]. This is problematic for the Chern number we discussed in the previous section, because (1) our derivation assumed the bands to be separated and, more importantly, (2) two bands in a Kramers pair will necessarily have equal and opposite Chern numbers, such that they cancel out exactly. We will return to this point in the next section. In the absence of magnetism or an external magnetic field, crystals typically have TRS.

Next, we have $P = U\mathcal{K}$, which describes *particle-hole symmetry* (PHS). This symmetry exchanges electrons and holes, enforcing the electronic dispersion to be mirrored in E_F. This is seen in superconducting systems, in which only the parity of the particle number is conserved because the Hamiltonian allows for the creation and annihilation of bounded pairs of electrons called Cooper pairs. While effective model Hamiltonians may have PHS, this symmetry is rarely (possibly never) truly satisfied by real insulating crystals when all Bloch bands are considered. Just like with TRS, a Hamiltonian can behave in three ways under P: it either doesn't have this symmetry, or $P^2 = \pm 1$.

Finally, C describes a *chiral symmetry*. This type of symmetry is not entirely independent of TRS and PHS; if a Hamiltonian has both of these sym-

[11] In the presence of SOC, Bloch states generically will not have a well-defined spin-up or spin-down character; the Hamiltonian will not be block-diagonal. At TRIMs, however, the SOC necessarily goes to zero, and there will necessarily be a degenerate pair of states.

symmetry	symmetries			spatial dimensions			
class	T	P	C	0	1	2	3
A				$\mathbb{Z}$		$\mathbb{Z}$	
AI	1			$\mathbb{Z}$			
AII	-1			$2\mathbb{Z}$		$\mathbb{Z}_2$	$\mathbb{Z}_2$
AIII			1		$\mathbb{Z}$		$\mathbb{Z}$
BDI	1	1	1	$\mathbb{Z}_2$	$\mathbb{Z}$		
CII	-1	-1	1		$2\mathbb{Z}$		$\mathbb{Z}_2$
D		1		$\mathbb{Z}_2$	$\mathbb{Z}_2$	$\mathbb{Z}$	
C		-1				$2\mathbb{Z}$	
DIII	-1	1	1		$\mathbb{Z}_2$	$\mathbb{Z}_2$	$\mathbb{Z}$
CI	1	-1	1				$2\mathbb{Z}$

Table 2.1: The periodic table of topological insulators, also called the tenfold way [61, 62]. The first column indicates the symmetry class in the Cartan nomenclature for symmetric spaces. The next three rows show whether these classes have time-reversal (T), particle-hole (P) and/or chiral (C) symmetry, and whether these symmetry operators square to plus or minus one. The remaining rows show the homotopy groups, related to the type of topological index per spatial dimension.

metries, then it automatically has chiral symmetry $C = P \cdot T$ (see Figure 2.3). Conversely, if a system has exactly one of the other two symmetries, it *cannot* have a chiral symmetry. On the other hand, if neither of the other two symmetries are present, then the system may or may not have a chiral symmetry. Unlike P and T, a Hamiltonian may have multiple anti-commuting unitary symmetries. Also unlike the other two, C always squares to $+1$. A common example of a chiral symmetry is a *sublattice symmetry* in a bipartite lattice.

These three fundamental symmetries together define ten distinct symmetry classes. Historically, three classes were initially identified, based on the presence or absence of TRS and spin rotation symmetry (which determines whether $T^2 = \pm 1$) [56, 57]. Next, chiral classes were identified in the context of QCD Dirac operators [58, 59], which extended the number of symmetry classes to six. Finally, the tenfold classification was completed by Altland and Zirnbauer [60], who found the remaining classes by considering a model system of a metallic quantum dot in contact (via a barrier) with a superconductor. These ten symmetry classes are listed in order of their discovery in Table 2.1.

This classification was found to be particularly useful for identifying what topological phases are possible, given the symmetry class of a Hamiltonian. That is, it specifies the number of topologically distinct ground states that are possible for non-interacting systems of particles. To identify the topological phases, a link is made between the homotopy group of the different classes – used in algebraic topology to classify topological spaces – and the allowed topological invariant distinguishing Hamiltonians with these symmetries [61, 62].

These homotopy groups are given either by $\mathbb{Z}$ (any integer); $2\mathbb{Z}$ (any even integer); or $\mathbb{Z}_2 = \mathbb{Z}/2\mathbb{Z}$ (any integer modulo 2, *i.e.* 0 or 1). The full 'periodic table of topological insulators and superconductors' was built up by considering massive Dirac Hamiltonians[12] in arbitrary spatial dimensions d [61, 62], but generalises to any gapped Bloch Hamiltonian. Different dimensionalities are linked, because one can always add a new momentum k_{d+1} to the Hamiltonian in such a way that the gap does not close for any value of k_{d+1} in the BZ. This way the topological invariant should remain the same, while adding a momentum may change the symmetry class. In this way, the topological classification of different groups for different value of d can be derived. A mathematically beautiful feature is that the entire periodic table is periodic over 8 dimensions, but spatial dimensions beyond $d = 3$ are usually not relevant in the context of condensed matter physics.

2.3. Topology with TRS

Now that we have identified the allowed homotopy groups per symmetry class, let us consider what these actually mean in terms of topological invariants. In the top row of the table, in class A, we can already identify the $\mathbb{Z}$-valued Chern number for $d = 2$. As already mentioned in the previous section, real materials are not expected to have true PHS; this is because Bloch electron bands can be understood to arise from linear combinations of atomic orbitals centred on atoms in the crystal [63], and there is no reason for these orbitals to have PHS. Meanwhile, any non-magnetic material can be expected to have TRS. Adding TRS and no other symmetries means that we go from class A to class AII. As already mentioned, TRS enforces bands to come in Kramers pairs, within which the bands necessarily have equal and opposite Chern numbers. In $d = 2$ (and $d = 3$), the invariant is $\mathbb{Z}_2$, different from the $\mathbb{Z}$ Chern number. The question then, is how to generalise the concept of a Chern number to class AII.

The $\mathbb{Z}_2$ invariant we use is conventionally known as the FKM invariant, after Fu, Kane and Mele, who defined it as a product over all TRIMs ($\mathbf{k} = \Gamma_i$) in the 2D or 3D BZ of a parameter called δ_i:

$$(-1)^\nu = \prod_{i=1}^{\text{TRIMs}} \delta_i \tag{2.15}$$

In 2D the BZ has four TRIMs while in 3D there are eight.[13] In the original works, the parameter was defined in two ways. The first employs a unitary matrix relating time-reversed wavefunctions $w_{mn}(\mathbf{k}) = \langle u_m(-\mathbf{k})| T |u_n(\mathbf{k})\rangle$, which

[12] A Dirac Hamiltonian has a linear-in-$\mathbf{k}$ dispersion, and describes relativistic particles. Adding an independent-of-$\mathbf{k}$ mass term opens a gap at the Dirac point $\mathbf{k} = 0$.

[13] In three dimensions, one can identify one 'strong' topological invariant, given by Equation 2.15, and three 'weak' topological invariants corresponding to products taken over TRIMs in three sets of perpendicular planes within the BZ [64]. We will not go into the weak invariants here.

is anti-symmetric at $\mathbf{k} = \Gamma_i$ [64, 65]. The second way is valid for any system with inversion symmetry, whose operator I relates a state at $\mathbf{k}$ to a state at $-\mathbf{k}$ without affecting the spin, and whose eigenvalues at the TRIMs equal δ_i [66]. These two definitions are given by

$$\delta_i = \frac{\sqrt{\det[w(\Gamma_i)]}}{\mathrm{Pf}[w(\Gamma_i)]} = \prod_n^{N_{\mathrm{occ}}/2} \langle u_{2n}(\Gamma_i)| I |u_{2n}(\Gamma_i)\rangle = \pm 1. \tag{2.16}$$

Later, it was shown that the FKM invariant for 2D systems can be equivalently found using an integral over a *non-Abelian* Berry connection, given by [67–70]:

$$\begin{aligned} \mathbf{A}_{mn}(\mathbf{k}) &= i \langle u_m(\mathbf{k})| \nabla_{\mathbf{k}} |u_n(\mathbf{k})\rangle \\ &= \lim_{d\mathbf{k}\to 0} i \frac{\langle u_m(\mathbf{k})|u_n(\mathbf{k}+d\mathbf{k})\rangle - \langle u_m(\mathbf{k})|u_n(\mathbf{k})\rangle}{d\mathbf{k}}, \end{aligned} \tag{2.17}$$

where m and n are band labels. The second line shows the discrete form of the gradient. In the case of N bands that are entirely isolated from one another, only Abelian Berry connections $\mathbf{A}_{nn}(\mathbf{k})$ will be non-zero. However, when bands cross one another, curvature in the Berry connection may be exchanged, and off-diagonal terms (where $m \neq n$) will appear. Using the non-Abelian Berry connection, one can define a $U(N_{\mathrm{occ}})$ matrix known as a *Wilson loop* by integrating the non-Abelian Berry connection over a closed loop $\mathcal{C}$:

$$\mathcal{W}[\mathcal{C}] = \mathcal{P} \exp\left(i \oint_{\mathcal{C}} \mathbf{A} \cdot d\mathbf{k} \right), \tag{2.18}$$

where $\mathcal{P}$ indicates path ordering. Much like the Berry phase, the eigenvalues of the Wilson loop are equal to gauge-invariant phase factors $e^{i\theta_j}$. The fact that the eigenvalues are phases means that the spectrum is only defined modulo 2π. In fact, in most cases one can continuously transform a TRS Hamiltonian – without going through a topological phase transition – such that all Kramers pairs are separate from each other,[14] and we can consider the $U(2)$ Wilson loop per (occupied) Kramers pair. This means we need only consider two eigenvalues at a time, which is easier to work with than N_{occ} eigenvalues; from now on we will consider only such $U(2)$ Wilson loops. The eigenvalues of a generic loop will not be quantised, but if the loop taken is invariant under TRS, then each Kramers pair will necessarily have a degenerate pair of phases θ.

To obtain the FKM invariant, we have to somehow integrate $\mathbf{A}_{mn}(\mathbf{k})$ over the 2D BZ, rather than just across a single loop. One way to do this is to consider a set of loops $\mathcal{C}_{k_x}$ that cycle over the BZ along k_y from $-\pi$ to π through 0,[15] at a fixed values of k_x. Plotting the Wilson loop eigenvalues as a function of

[14] Only some special symmetries, such as non-symmorphic lattice symmetries, are able to stick Kramers pairs together.

[15] We assume the lattice parameter is unity here.

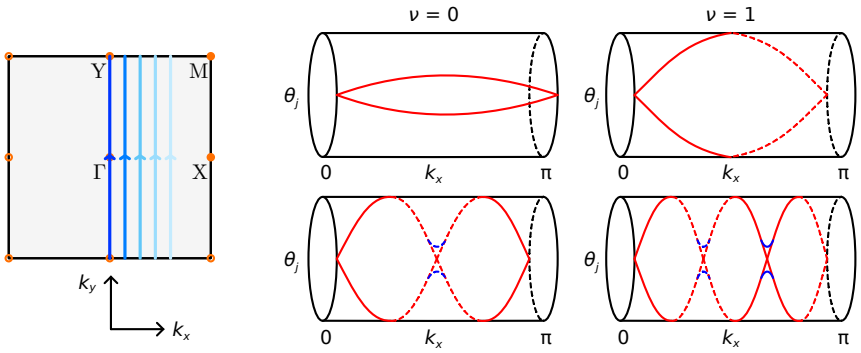

Figure 2.4: Example $U(2)$ Wilson loop spectra, showing the eigenvalues θ_j of $\mathcal{W}[\mathcal{C}_{k_x}]$ with the loops going from $k_y = -\pi$ to π at fixed values of k_x. On the left, we show the relevant series of $\mathcal{C}_{k_x}$ (in blue) for an example BZ with a two-fold lattice symmetry. On the right, we plot the θ_j on a cylinder (gluing $\theta_j = \pi$ and $-\pi$ together) for k_x ranging from 0 to π. The symmetries present ensure that eigenvalues are degenerate at the ends of the cylinders. Away from these values of k_x, crossings of the eigenvalues are not protected by TRS, and may be gapped as shown in blue. The FKM invariant ν is given by the parity of the winding of θ_j around the cylinder; $\nu = 0$ for the left two spectra, and 1 for the right two spectra. We have set all lattice parameters to unity here.

k_x for a whole series of these loops, we obtain a *Wilson loop spectrum* (WLS). If we consider a system with TRS and any two-fold unitary symmetry that sends $k_y \to -k_y$ – such as two-fold rotation, a mirror, or inversion symmetry – then the loops at $k_x = 0$ or $\pm\pi$ are invariant under the symmetries, and the eigenvalues of those Wilson loops are necessarily degenerate [68–70]. This is useful, because it means we can ensure that our WLS starts and ends with degenerate eigenvalues. In this case, the series of Wilson loops need to cover only half of the BZ, because the symmetries ensure that the other half will be the same. As k_x is varied, then, the eigenvalues may wind, or not. Any crossing between eigenvalue pairs for $\mathcal{C}_{k_x}$ away from $k_x = 0$ or $\pm\pi$ are not protected by any symmetries, and may open up a gap upon a smooth deformation of the Hamiltonian [68–70]. This means that in the absence of additional symmetries, only the parity of the winding of the Wilson loop eigenvalues matters, and this parity equals the FKM invariant (ν) as given by Equation 2.15. This may be demonstrated by plotting θ_j on a cylinder (gluing together $\theta_j = \pi$ and $-\pi$) as shown in Figure 2.4.

That a non-zero FKM invariant may have physical implications was also demonstrated by Kane and Mele [71, 72]. In this case, we find a Quantum Spin Hall (QSH) insulator, which hosts an odd number of pairs of opposite-spin edge states that are topologically protected in the sense that they are robust against backscattering (which would require a spin flip) and small perturbations. Kane and Mele demonstrated this QSH effect using a model based on two time-reversed copies of the Haldane model. Unlike in the IQHE and QAHE, the edge spin-Hall conductivity σ^s_{xy} is not generally quantised. We can express it

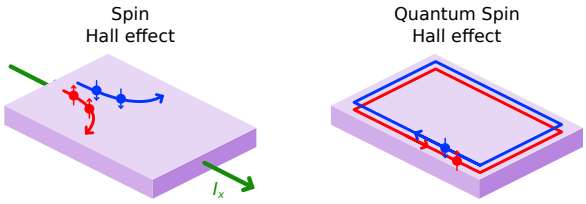

Figure 2.5: Two types of 'spin Hall effect' in 2D materials. The normal effect (left) describes the spin accumulation on opposite sides of a material with an in-plane current I_x, due to spin-dependent Mott scattering or an intrinsic spin-orbit interaction. The Quantum Spin Hall (QSH, right) effect is a topological phase where two edge currents of opposite spin flow in opposite directions. A QSH insulator can be understood as being composed of two time-reversed copies of a QAH insulator (Figure 2.2). The currents are not necessarily quantised.

as

$$\sigma_{xy}^{s} = \frac{e}{h}\left(\langle S_z\rangle_L - \langle S_z\rangle_R\right)\Big|_{E_F}, \tag{2.19}$$

where $\langle S_z\rangle_L$ corresponds to the spin expectation value (along the z-axis) for left-moving edge states, and R labels the right-moving edge states. Because the edge states are not necessarily eigenstates of S_z, the difference need not be an integer.[16] Nonetheless, the topological protection of these spin-dependent edge states makes them an interesting candidate for spintronic applications (see *e.g.* [73]). The QSH effect was first experimentally detected by König *et al.* in a HgTe/CdTe quantum well structure in 2007 [74], after being predicted theoretically by Bernevig, Hughes and Zhang the year before [75].

2.4. The importance of lattice symmetries

Now, let us consider the role of lattice symmetries. These include point-group symmetries (rotations, reflections, inversions) as well as non-symmorphic symmetries (glide planes and screw axes). That these symmetries may constrain the topology can be made clear by some examples. In the absence of TRS, the Chern number is necessarily zero in the presence of a reflection symmetry, due to the anti-symmetric nature of the Berry curvature [76]; for a 2D crystal with a mirror plane along x, we find that $F_n(k_x, -k_y)$ is equal to $-F_n(k_x, k_y)$ such that the integral of the Berry curvature over the entire BZ gives exactly zero. With TRS present, the relation between topology and lattice symmetries is exemplified by the fact that the FKM invariant may be expressed in terms of the eigenvalues of the inversion operator at high-symmetry points (Equation 2.16). This procedure can be generalised to include any space group symmetry in two and three spatial dimensions [77]. In many cases, the extra constraints that lattice symmetries impose lead to the possibility of new topological invariants, protected by the symmetries of the lattice. These invariants cannot be changed without breaking a (lattice) symmetry or closing a gap at the Fermi level, and

[16] Note that TRS ensures that the sum $\langle S_z\rangle_L + \langle S_z\rangle_R = 0$.

go beyond the classification given by the tenfold way. This has lead to the concept of 'topological crystalline insulators' [78]. Excitingly, the fact that lattice symmetries may be broken at some surfaces and edges of crystals, but protected at others, allows for exotic surface, edge and corner states, leading to higher-order and hybrid-order topological phases [79–84].

Recent years have seen various efforts to expand and complete the classification of crystalline topological phases [77, 85–88]. A mathematically robust way to determine what phases are allowed is to use what is known as (twisted equivariant) K-theory [88–92]. However, in class AII, K-theoretic calculations are exceedingly difficult to perform except for a few specific cases [91]. Instead, we will outline here the more intuitive classification scheme outlined by refs. [35, 36].

To begin with, it is useful to make the distinction between two types of invariants, which we will call *torsion invariants* and *representations*. The first describes the invariants derived from curvature in the Berry connection, and includes the Chern number and FKM invariants. The second is a set of integers that characterise the representation of the occupied bands of a topological phase in the corresponding crystal symmetry group.[17] To understand the latter, note that the Bloch functions on the BZ must transform under crystal symmetries in a particular way, in a manner which depends on the value of $\mathbf{k}$ [93]. The crystal symmetries in real space do not apply to all $\mathbf{k}$-points in the BZ, instead being restricted to certain high-symmetry points and lines. At such high-symmetry locations, the transformations of the Bloch functions must satisfy certain gluing conditions, as determined by the crystal symmetries that are present.

As an example, consider a square lattice with lattice spacing $a = 1$ in wallpaper group *p4mm* (in the Hermann-Mauguin notation [94]), or equivalently dihedral point group D_4. This is the symmetry group generated by a reflection t about the x-axis and an in-plane 90° rotation r. Because of these symmetries, many regions of the BZ map onto one another, and to describe it we need only consider the fundamental BZ domain, shown in Figure 2.6. The high-symmetry points $\Gamma = (0, 0)$ and $\mathrm{M} = (\pi, \pi)$ are left invariant by all operations in D_4. The point $X = (\pi, 0)$ is only left invariant by the little co-group $G^{\mathrm{X}} = \{1, r^2, t, r^2t\}$, which can be specified by two binary numbers $\mathbb{Z}_2 \times \mathbb{Z}_2$. The high-symmetry lines l_i have a lower symmetry, described by $\mathbb{Z}_2$ little co-groups: $G^{l_1} = \{1, t\}$; $G^{l_2} = \{1, r^2t\}$; $G^{l_3} = \{1, rt\}$. Finally, any other generic point in the interior of the fundamental domain is only invariant under the identity operation.

Importantly, the little co-groups may necessitate bands at high-symmetry points to become degenerate. This can be seen by considering the action of the

[17] The number of occupied states in $d = 0$ is also a type of representation invariant. This is simply $\mathbb{Z}$-valued, because there are no internal symmetries that allow for more than one representation.

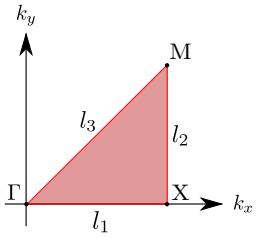

Figure 2.6: The fundamental BZ domain (shaded red) in wallpaper group $p4mm$. It contains only points that are not related to each other by transformations in the point group D_4. Γ, X and M label high-symmetry points, and l_i label high-symmetry lines. Figure taken from [35].

crystal symmetries on the Bloch Hamiltonian:

$$\begin{aligned} \rho(R)h(\mathbf{k})\rho(R)^{-1} &= h(R\cdot\mathbf{k}); \\ [\rho(R), h(\mathbf{k})] &= 0 \qquad \text{if } R\cdot\mathbf{k} = \mathbf{k}, \end{aligned} \tag{2.20}$$

where $\rho(R)$ is a matrix representation of the point group element R. $h(\mathbf{k})$ commutes with the little co-group at high-symmetry points and lines, such that the eigenstates of the Bloch Hamiltonian are also eigenstates of the elements of the little co-group. This means that the collection of occupied Bloch states at momentum $\mathbf{k}$ forms a representation of the the little co-group $G^{\mathbf{k}}$, consisting of irreducible representations of $G^{\mathbf{k}}$. These representations are the eigenvalues of symmetry operators in $G^{\mathbf{k}}$; for a $\mathbb{Z}_2$ group, these are just equal to ± 1, so eigenstates may be either even $(+)$ or odd $(-)$ under the symmetry transformations.

We can now write down a set of integers $n_i^{\mathbf{k}}$, indicating the number of bands at some momentum $\mathbf{k}$ with symmetry representations i, *e.g.* n_1^{X} is the number of bands at the X-point with the set of symmetry eigenvalues labelled by 1. Importantly, the representations along high-symmetry lines l_i must connect continuously to representations at their end-points. This means that the eigenvalue of a certain symmetry transformation is conserved along all high-symmetry lines, and restricts the choice of representations on the high-symmetry points, where multiple l_i meet. These restrictions relate different $n_i^{\mathbf{k}}$ together, and provide a recipe for constructing the entire set of occupied bands at high-symmetry locations. In the case of wallpaper group $p4mm$, we end up with five independent relations between 14 integers $n_i^{\mathbf{k}}$, such that we need to specify nine integers in total to completely characterise the set of valence bands; the representation is thus classified by elements of $\mathbb{Z}^9$.

In ref. [35], Kruthoff *et al.* use this method to obtain the complete topological classification for all 17 wallpaper groups (2D crystal symmetry groups) in class A, listed in Table 2.2, and note that this classification scheme can be extended to all three-dimensional crystals. The torsion invariant in this case is the Chern number, which can only be non-zero in wallpaper groups without any reflection symmetries present [76]; this is why all groups with a mirror

group	$p1$	$p2$	pm	pg	cm	$p2mm$	$p2mg$	$p2gg$	$c2mm$
reps	$\mathbb{Z}$	$\mathbb{Z}^5$	$\mathbb{Z}^3$	$\mathbb{Z}$	$\mathbb{Z}^2$	$\mathbb{Z}^9$	$\mathbb{Z}^4$	$\mathbb{Z}^3$	$\mathbb{Z}^6$
Chern no.	$\mathbb{Z}$	$\mathbb{Z}$	0	0	0	0	0	0	0

group	$p4$	$p4mm$	$p4gm$	$p3$	$p3m1$	$p31m$	$p6$	$p6mm$
reps	$\mathbb{Z}^8$	$\mathbb{Z}^9$	$\mathbb{Z}^6$	$\mathbb{Z}^7$	$\mathbb{Z}^5$	$\mathbb{Z}^5$	$\mathbb{Z}^9$	$\mathbb{Z}^8$
Chern no.	$\mathbb{Z}$	0	0	$\mathbb{Z}$	0	0	$\mathbb{Z}$	0

Table 2.2: The complete classification of topological phases in class A (without any anti-commuting or anti-unitary symmetries), for all 2D crystals [35]. The first and fourth rows list the 17 wallpaper groups in Hermann-Mauguin notation [94]. The rows labelled by 'reps' list the number of integers that need to be specified to classify the representation of the occupied bands. The remaining rows indicate whether a Chern number is present. The full classification is given by the direct sum of the representation and the Chern number invariants.

plane (indicated by m) or non-symmorphic glide reflections (g) have zero as their Chern number index. The full classification is given by the direct sum of the representation invariants and the Chern number. From this we learn that the number of topological indices needed to classify the topological phase in 2D materials without TRS varies from $\mathbb{Z}$ in wallpaper group pg, to $\mathbb{Z}^{10}$ in $p6$. Clearly, the lattice symmetry matters!

Of course, many materials have TRS, and therefore belong to class AII. The classification for this class is determined in ref. [36]. An important difference is that in this class, all bands must come in Kramers pairs composed of states related by TRS, and the transformations of a Kramers pair under (lattice) symmetry operations now produce a pairs of related eigenvalues. This greatly reduces the number of allowed representations; in the example of $p4mm$, TRS reduces the number or representation invariants from nine to three.

More interestingly, in class AII there are more allowed types of torsion invariants. We have already introduced the FKM invariant, but the presence of lattice symmetries also allows for additional 'line invariants' which describe integrals of the non-Abelian Berry connection along certain high-symmetry directions in the crystal, which are quantised by the combination of (at least two) symmetries that are present. An example in 1D is the LBO invariant introduced by Lau, van den Brink and Ortix [95], which corresponds to the Wilson loop eigenvalues that are quantised by the combination of TRS and a mirror symmetry in the lattice. This invariant may be generalised to 2D, where Wilson loop eigenvalues along lines that are invariant under TRS and any two-fold lattice symmetry are also necessarily quantised [69, 70, 96], as mentioned in the previous section. In fact, this is equivalent to computing the FKM invariant for a subset of TRIM points along a single line 2D or within a single plane in 3D [64, 66].

To determine how many torsion invariants are allowed per wallpaper group, ref. [36] considers the restrictions upon where vortices in the $U(1)$ (Abelian) Berry connection are allowed by the symmetries present. Such vortices cor-

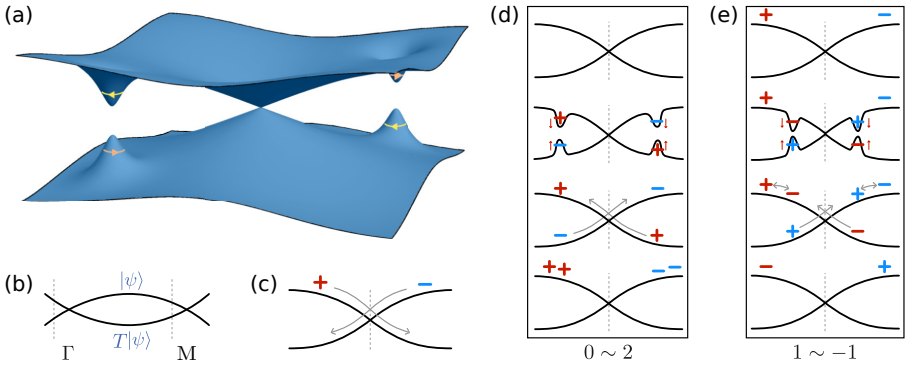

Figure 2.7: (a) The typical band structure of a Kramers pair close to a high-symmetry point. Also shown schematically is two band inversions, related by TRS, which generate vortices in the Berry connection as indicated by the yellow and orange arrows. (b) A more schematic representation of two bands containing states $|\psi\rangle$ and $T|\psi\rangle$, which are necessarily degenerate at the TRIMs Γ and M. (c) Time-reversed pairs of vortices in the Berry connection, depicted by + and −, may be moved throughout the BZ without annihilating. (d) An even number of vortices, generated by band inversions within a single Kramers pair, do not change the topological index, such that having 0 vortices in a band is topologically equivalent to having 2. (e) In the same way, having a single vortex in a band is equivalent to having a single antivortex. Figure taken from [36].

respond to peaks in the Berry curvature, which may be generated by a band inversion. In the absence of TRS, the Chern number simply measures the number of vortices in each individual band. With TRS, any vortex generated by a band inversion at some momentum $\mathbf{k}$ must be associated with an antivortex (which has opposite handedness) at the time-reversed momentum $-\mathbf{k}$. Vortices in TRS materials thus necessarily come in vortex-antivortex pairs, as shown in Figure 2.7, and the total Chern number of any Kramers pair of bands is necessarily zero, as already noted in the previous section. At TRIMs, time-reversed pairs of vortices cannot annihilate, due to the orthogonality of the states [97]. Since band inversions within a single Kramers pair do not close the gap at E_{F}, and do not break any symmetries, we can only distinguish (using the $\mathbb{Z}_2$ FKM invariant) between and odd and an even number of vortices in the $U(1)$ Berry connection of a single band.

Just like TRS, lattice symmetries can impose further restrictions on where and how vortices are allowed to appear in the BZ. In the presence of n-fold rotational symmetries, for example, any vortex in the interior of the BZ must be accompanied by $n-1$ other ones at the symmetry-related momenta. Notice, however, that these symmetry-related vortices all have the same handedness, in contradiction to what is required by TRS. The combination of TRS with any even-fold rotational symmetry actually enforces that vortices in the Berry connection may *only* appear at TRIMs, or at points in the bulk of the BZ where two states are degenerate. Vortices in the bulk of the BZ are usually unimportant to the topological phase, because they necessarily come in pairs

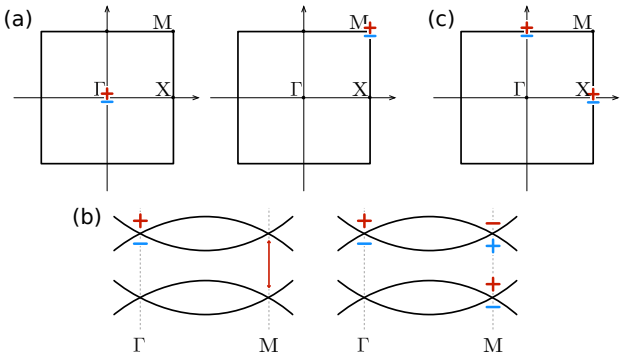

Figure 2.8: (a) Topologically nontrivial vortex configurations with $p4$ symmetry in class AII, with a nontrivial FKM invariant but different line invariants along ΓX. (b) A band inversion between two Kramers pairs may generate extra vortices, but will not change the overall FKM invariant. (c) A different allowed vortex configuration, with trivial FKM invariant but nontrivial line invariants. Figure taken from [36].

group	$p1$	$p2$	pm	pg	cm	$p2mm$	$p2mg$	$p2gg$	$c2mm$
reps	$\mathbb{Z}$	$\mathbb{Z}$	$\mathbb{Z}$	$\mathbb{Z}$	$\mathbb{Z}$	$\mathbb{Z}$	$\mathbb{Z}$	$\mathbb{Z}$	$\mathbb{Z}$
torsion	$\mathbb{Z}_2$	$\mathbb{Z}_2^4$	$\mathbb{Z}_2^2$	$\mathbb{Z}_2$	$\mathbb{Z}_2$	$\mathbb{Z}_2^4$	$\mathbb{Z}_2^2$	$\mathbb{Z}_2^2$	$\mathbb{Z}_2^3$
group	$p4$	$p4mm$	$p4gm$	$p3$	$p3m1$	$p31m$	$p6$	$p6mm$	
reps	$\mathbb{Z}^3$	$\mathbb{Z}^3$	$\mathbb{Z}^2$	$\mathbb{Z}^4$	$\mathbb{Z}^4$	$\mathbb{Z}^3$	$\mathbb{Z}^4$	$\mathbb{Z}^4$	
torsion	$\mathbb{Z}_2^3$	$\mathbb{Z}_2^3$	$\mathbb{Z}_2^2$	$\mathbb{Z}_2^2$	$\mathbb{Z}_2^2$	$\mathbb{Z}_2^2$	$\mathbb{Z}_2^3$	$\mathbb{Z}_2^3$	

Table 2.3: The complete classification of topological phases in class AII (with TRS), for all 2D crystals [36]. The first and fourth rows list the 17 wallpaper groups in Hermann-Mauguin notation [94]. The rows labelled by 'reps' list the number of integers that need to be specified to classify the representation of the occupied bands. The remaining rows indicate the torsion invariants. The full classification is given by the direct sum of the representation and the torsion invariants.

due to TRS, and therefore do not change the parity of the total curvature in the BZ (see Figure 2.7d,e).

Depending on the lattice symmetries present, the problem of identifying what topological phases are possible reduces to the problem of counting the number of distinct ways in which you can place vortex-antivortex pairs in the BZ. Additionally, line invariants (such as LBO) simply count the parity of the number of vortices along a high-symmetry line, which will constitute a topological invariant in the presence of the correct symmetries. Depending on the wallpaper group, there will be a limited number of independent line invariants that one can consider. Figure 2.8 demonstrates some example vortex configurations for wallpaper group $p4$. The resulting complete classification for 2D crystals in class AII is listed in Table 2.3. The generalisation to 3D is also explained in ref. [36], but will not be discussed here.

With the completion of the topological classification of 2D crystals, it be-

came immediately clear that not all topological invariants had been identified. Notably in class AII, wallpaper groups $p2$, $p2mm$, $p4$, $p4mm$, $p3$, $p6$ and $p6mm$ all require an invariant that is not given by the known FKM and LBO invariants. This is the starting point of Chapter 3, in which we demonstrate how to identify a new invariant in $p3$, with a method that is generalisable to the other rotationally symmetric wallpaper groups.

3

The topological invariants of rotationally symmetric crystals

Recent formal classifications of crystalline topological insulators predict that the combination of time-reversal and rotational symmetry gives rise to topological invariants beyond the ones known for other lattice symmetries. Although the classification proves their existence, it does not indicate a way of calculating the values of those invariants. Here, we show that a specific set of concentric Wilson loops and line invariants yields the values of all topological invariants in two-dimensional systems with three-fold rotational symmetry in class AII. The same method can also be applied to other rotation groups. We find a new invariant that relates to the presence of higher-order topology and corner charges. This chapter is based on ref. [1].

As we've demonstrated in Chapter 2, the presence or absence of symmetries in crystalline topological insulators allows for the emergence of a wide variety of topological phases. These are labelled by an equally wide variety of topological invariants, ranging from the Chern number [49], to the Fu-Kane-Mele (FKM) invariants [64–66, 68, 69, 71, 72], the Lau-Brink-Ortix (LBO) or line invariants [95], as well as invariant features of the Wilson loop spectrum describing higher-order and fragile topological insulators [70, 81, 96, 98–101]. A unified, symmetry-based approach describing all of these topological phases was recently proposed [35, 36, 77, 102, 103]. This shows that the FKM, LBO, higher order, and similar invariants may all be extracted from an algorithmic analysis of lattice symmetries and their effect on the structure of Berry curvature. Moreover, being a complete classification of all possible such invariants (as guaranteed by the underlying K-theory), it predicts that additional, as yet unidentified, invariants of the same type exist in various crystals, for example

those with rotational symmetries and time-reversal symmetry (TRS) in two dimensions [36]. Explicitly: in wallpaper groups $p2$, $p3$, $p4$, and $p6$ we expect to find 4, 2, 3, and 3 $\mathbb{Z}_2$ invariants, of which only 3, 1, 2 and 2 invariants are known.

Although the classification predicts the existence of topological invariants for systems with a given symmetry, it does not give a way of identifying or evaluating them in any specific system. Here, we demonstrate how to find all topological invariants for wallpaper group $p3$ in class AII, including the thus far unidentified one. The same method can be applied to all other rotationally symmetric wallpaper groups, if we assume that there are no degenerate states away from time-reversal invariant momenta (TRIMs). Our analysis employs a spectrum of concentric Wilson loops rather than the usual spectrum of parallel Wilson loops [68–70, 96, 104]. The concentric loops are tailored to the rotational symmetry of the crystal lattice, allowing them to capture the full influence of symmetry on the topological structure.

Below, we will first introduce these concentric Wilson loops, their symmetry properties, and how to identify the new invariant. In Section 3.2, we show an example of our analysis in a model based on the Haldane model, which hosts three distinct topological phases. In Section 3.3, we demonstrate that depending on the topological phase, our model Hamiltonian hosts either no in-gap states, topologically protected edge states, or in-gap corner charges. We conclude with a discussion of the implications of our results in Section 3.4.

3.1. The concentric Wilson loop spectrum

The gauge invariant eigenvalues of (non-Abelian) Wilson loops can be interpreted as generalising the (Abelian) Berry phase to systems with internal and lattice symmetries [81]. As a reminder, the eigenvalues of any Wilson loop $\mathcal{W}[\mathcal{C}]$ are restricted to being a pure phase factor $\exp(i\theta_j)$, where j denotes the eigenvalue index. From here on, we use the term 'eigenvalue' to indicate the phase θ_j. A $U(1)$ Wilson loop eigenvalue for a single (isolated) band is equivalent to the Berry phase (γ_n) on a closed loop, as introduced in Section 2.1. Here we consider systems with TRS, in which Bloch states necessarily come in Kramers pairs; because Kramers degeneracies can not be separated from one another, a natural object to consider is the $U(2)$ Wilson loop for two bands within a Kramers pair. We assume here that there are no other symmetries present (like non-symmorphic ones [105]) that enforce degeneracies between different Kramers pairs. Then, one can always continuously deform the Hamiltonian – without going through any topological phase transition – such that all Kramers pairs are separated from one another. We will restrict our attention to the $U(2)$ Wilson loops relevant for TRS crystals from here on.

In Section 2.3, we demonstrated how considering a series of parallel Wilson loops that cycle the Brillouin zone (BZ) torus at a fixed value of k_x gives one a Wilson loop spectrum (WLS) of eigenvalues θ_j, and the parity of the winding of

these eigenvalues is equal to the FKM invariant. As a side note, this winding is only well-defined in the presence of two-fold lattice symmetries, which together with TRS enforce that the Wilson loop eigenvalues along high-symmetry lines are degenerate and quantised. Here, we will introduce a different set of *concentric* loops, which allows us to not only evaluate the generic FKM invariant (for any wallpaper group), but also the newly-predicted invariant specific to topological insulators with rotational symmetry.

In general, a non-Abelian Berry connection is an $N \times N$ skew-Hermitian matrix with vector-valued components defined as $\mathbf{A}_{mn}(\mathbf{k}) = i \langle u_m(\mathbf{k}) | \nabla_k | u_n(\mathbf{k}) \rangle$. Here, $|u_n(\mathbf{k})\rangle$ indicates an occupied Bloch state at momentum $\mathbf{k}$ with band index $n \in \{1, \ldots, N\}$. The Wilson loop $\mathcal{W}[\mathcal{C}]$ on a closed contour $\mathcal{C}$ in the BZ is then given by:

$$\mathcal{W}_{mn}[\mathcal{C}] = \left[\mathcal{P} \exp\left(i \oint_{\mathcal{C}} \mathbf{A} \cdot d\mathbf{k} \right) \right]_{mn}, \tag{3.1}$$

with $\mathcal{P}$ indicating path ordering. This is a $U(N)$ matrix, and satisfies $\mathcal{W}[\mathcal{C}]\mathcal{W}[\mathcal{C}]^\dagger = \mathcal{W}[\mathcal{C}]\mathcal{W}[\mathcal{C}_r] = 1$, with $\mathcal{C}_r$ the orientation-reversed loop. Our goal is to derive (new) topological invariants from a WLS by exploiting the symmetry properties of $\mathcal{W}[\mathcal{C}]$. In the presence of TRS and additional symmetries, two types of $\mathcal{C}$ are noteworthy. These are non-contractible cycles around the BZ seen earlier (the type most commonly considered in the literature [68–70, 96]) and non-contractible[1] loops that enclose high symmetry points (see *e.g.* [70]). Either type can be chosen to be invariant under time-reversal symmetry.

To see how TRS and other symmetries affect the Wilson loop operators along these two types of loops, we first discretise the Wilson loop, implementing the path-ordering explicitly. To do so, we use the discrete form of $\mathbf{A}_{mn}(\mathbf{k})$ (Equation 2.17) to rewrite the Wilson loop operator as

$$\mathcal{W}_{mn}[\mathcal{C}] = \lim_{L \to \infty} \langle u_m(\mathbf{k}_0) | \prod_{l=1}^{L} P(\mathbf{k}_l) | u_n(\mathbf{k}_{L+1}) \rangle, \tag{3.2}$$

where the product is path-ordered around $\mathcal{C}$, and we defined the projectors $P(\mathbf{k}_l) = \sum_j |u_j(\mathbf{k}_l)\rangle \langle u_j(\mathbf{k}_l)|$.[2] For a closed loop, $\mathbf{k}_0 = \mathbf{k}_{L+1}$ up to a reciprocal lattice vector. Expressing the Wilson loop explicitly in terms of Bloch states is useful, because we know how various symmetries act on these states.

Let us first consider the action of TRS on this representation of the Wilson loop. Recall that time-reversal maps states at $\mathbf{k}$ onto states at $-\mathbf{k}$. We may therefore write a Bloch state at $-\mathbf{k}$ in terms of time-reversed Bloch states at $\mathbf{k}$:

$$|u_n(-\mathbf{k})\rangle = \sum_m D_{nm}(\mathbf{k}) T |u_m(\mathbf{k})\rangle . \tag{3.3}$$

[1] The loops around high-symmetry points can be considered non-contractible, because the high-symmetry points are fixed points of the spatial symmetries.

[2] Note the similarity to Equation 2.4!

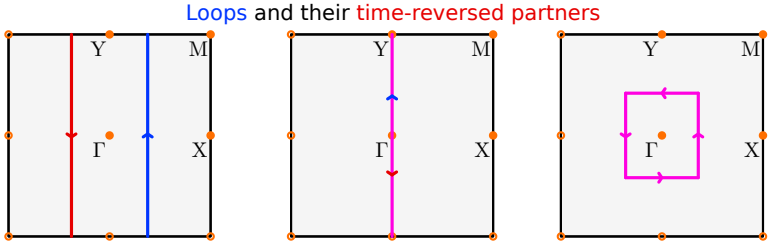

Figure 3.1: Three examples of closed loops in a BZ, and their time-reversed partners. The 'linear' loops (left two diagrams) obey $T\mathcal{W}(\mathbf{k}_0,\mathcal{C})T^{-1} = \mathcal{W}(-\mathbf{k}_0,\mathcal{C}_r) = \mathcal{W}(-\mathbf{k}_0,\mathcal{C})^\dagger$, while the right-most example obeys $T\mathcal{W}(\mathbf{k}_0,\mathcal{C})T^{-1} = \mathcal{W}(-\mathbf{k}_0,\mathcal{C}) = \mathcal{W}(\mathbf{k}_0,\mathcal{C})$.

The time reversal operator T includes complex conjugation and D is a unitary matrix. Using this relation, the projectors P at $-\mathbf{k}$ can also be related to ones at $\mathbf{k}$:

$$\begin{aligned} P(-\mathbf{k}) &= \sum_{j,m,m'} D_{jm}(\mathbf{k}) T \left|u_m(\mathbf{k})\right\rangle \left\langle u_{m'}(\mathbf{k})\right| T^\dagger (D_{m'j})^*(\mathbf{k}) \\ &= -\sum_m T \left|u_m(\mathbf{k})\right\rangle \left\langle u_m(\mathbf{k})\right| T^{-1} \\ &= -TP(\mathbf{k})T^{-1}. \end{aligned}$$

Here we used the fact that T is anti-unitary, such that $T^\dagger = -T^{-1}$. Examples of how different loops transform under TRS are shown in Figure 3.1. If we consider a generic 'linear' loop at constant value of k_x, TRS will reverse the direction of the loop, and move the starting point to $-\mathbf{k}_0$. This tells us that

$$T\mathcal{W}(\mathbf{k}_0,\mathcal{C})T^{-1} = \mathcal{W}(-\mathbf{k}_0,\mathcal{C}_r) = \mathcal{W}(-\mathbf{k}_0,\mathcal{C})^\dagger \tag{3.4}$$

This can be contrasted with a loop $\mathcal{C}$ that encloses Γ in a time-reversal symmetric manner ($T\mathcal{C}T^{-1} = \mathcal{C}$, right-hand plot of Figure 3.1), in which case:

$$T\mathcal{W}(\mathbf{k}_0,\mathcal{C})T^{-1} = \mathcal{W}(-\mathbf{k}_0,\mathcal{C}) = \mathcal{W}(\mathbf{k}_0,\mathcal{C}). \tag{3.5}$$

To see this explicitly, take for example four equally spaced points $\mathbf{k}_j$, $j = [0,3]$, on a unit circle in $\mathbf{k}$-space around $\mathbf{k} = 0$. T then maps $\mathbf{k}_j \to \mathbf{k}_{j+2}$, so the discrete Wilson loop $\mathcal{W} = P(\mathbf{k}_0)P(\mathbf{k}_1)P(\mathbf{k}_2)P(\mathbf{k}_3)$ gets mapped to:

$$\begin{aligned} T\mathcal{W}T^{-1} =& TP(\mathbf{k}_0)T^{-1}TP(\mathbf{k}_1)T^{-1}TP(\mathbf{k}_2)T^{-1}TP(\mathbf{k}_3)T^{-1} \\ =& P(\mathbf{k}_2)P(\mathbf{k}_3)P(\mathbf{k}_0)P(\mathbf{k}_1) = \mathcal{W}. \end{aligned} \tag{3.6}$$

This is the same discrete Wilson loop, with the four points rotated but their order remaining the same.

Unlike TRS, lattice symmetries are always unitary. Under a general unitary symmetry $g \in G$, the Wilson loop matrix elements of a loop $\mathcal{C}$ with base point

$\mathbf{k}_0$ transform as:

$$g : \mathcal{W}_{ij}(\mathbf{k}_0, \mathcal{C}) \to D^l_i(g, \mathbf{k}_0)\mathcal{W}_{lk}(g \cdot \mathbf{k}_0, g \cdot \mathcal{C})D^k_j(g, \mathbf{k}_0)^*. \tag{3.7}$$

Here $D^l_i(g, \mathbf{k}_0)$ is the representation of the symmetry g, which may depend on $\mathbf{k}_0$. Invariance under a unitary symmetry thus means

$$\mathcal{W}_{ij}(\mathbf{k}_0, \mathcal{C}) = D^l_i(g, \mathbf{k}_0)\mathcal{W}_{lk}(g \cdot \mathbf{k}_0, g \cdot \mathcal{C})D^k_j(g, \mathbf{k}_0)^*. \tag{3.8}$$

In the present chapter, we are interested in systems that have a discrete, n-fold rotation symmetry C_n.[3] In this case, we analogously find:

$$C_n \mathcal{W}(\mathbf{k}_0, \mathcal{C}) C_n^{-1} = \mathcal{W}(g \cdot \mathbf{k}_0, g \cdot \mathcal{C}), \tag{3.9}$$

where g is now a rotation operator.

As an example of how we can use these symmetry properties, consider a crystal with TRS in wallpaper group $p3$. The hexagonal Brillouin zone (depicted in Figure 3.2) hosts four time-reversal invariant momenta (TRIMs), namely Γ and M_i (with $i = 1, 2, 3$; mapped onto one another by C_3). The K-points are equivalent and symmetric under C_3, but mapped onto the K′-point under the action of the TRS operator T. Notice that $T^2 = (C_3)^3 = -1$, because of the spin-half nature of electrons. Unlike with any evenfold rotational symmetry, there is no combination of C_3 and T that maps a generic $\mathbf{k}$-point onto itself.[4] Nonetheless, what we demonstrate here generalises to any discrete rotational symmetry C_n.

The symmetry-based classification of crystalline topological insulators predicts two $\mathbb{Z}_2$ invariants[5] for three-fold symmetric systems [36], which is what we would like to extract using a smartly chosen series of Wilson loops. To do so, consider a path $\mathcal{C}_h$, which traces out an equilateral hexagon centered at Γ with side length $|\mathbf{k}_0|$. $\mathcal{C}_h$ is invariant under both C_3 and T, such that we obtain the following constraints on $\mathcal{W}_h(\mathbf{k}_0) = \mathcal{W}(|\mathbf{k}_0|, \mathcal{C}_h)$:

$$T\mathcal{W}_h(\mathbf{k}_0)T^{-1} = \mathcal{W}_h(\mathbf{k}_0); \qquad C_3\mathcal{W}_h(\mathbf{k}_0)C_3^{-1} = \mathcal{W}_h(\mathbf{k}_0). \tag{3.10}$$

We choose a gauge in which $T = i\sigma_y\mathcal{K}$ and $C_3 = e^{\sigma_z i\pi/3}$, and consider the $U(2)$ Wilson loop of a single Kramers pair. $\mathcal{W}_h(\mathbf{k}_0)$ can then be written as:

$$\mathcal{W}_h(\mathbf{k}_0) = \begin{pmatrix} a(\mathbf{k}_0) & b(\mathbf{k}_0) \\ c(\mathbf{k}_0) & d(\mathbf{k}_0) \end{pmatrix}. \tag{3.11}$$

[3] The subscript n should not be confused with the band index!
[4] That is, neglecting trivial combinations such as $C_3^3 T^2$.
[5] This corrects a statement in [36]: although $U(1)$ vortices at K cannot be moved, they can be smeared in a C_3 and time-reversal invariant fashion, leaving two rather than three $\mathbb{Z}_2$ invariants. Note that K is not a TRIM point, and there is no Kramers degeneracy there.

The symmetry constraints on the matrix elements are given by:

$$\begin{aligned} a(\mathbf{k}_0) &= d^*(-\mathbf{k}_0), \qquad & b(\mathbf{k}_0) &= -c^*(-\mathbf{k}_0), \\ a(\mathbf{k}_0) &= a(g\cdot\mathbf{k}_0), \qquad & b(\mathbf{k}_0) &= b(g\cdot\mathbf{k}_0)e^{-2\pi i/3}, \end{aligned} \tag{3.12}$$

where g is the action of the three-fold rotation symmetry on $\mathbf{k}$-space. The first two constraints come from TRS, while the latter two arise from the three-fold rotational symmetry. The Wilson loop under consideration only depends on the length of $\mathbf{k}_0$, and since $|g\cdot\mathbf{k}_0| = |\mathbf{k}_0|$, b must vanish in our chosen gauge. This means c also vanishes, and $d = a^*$. Furthermore, since the matrix $\mathcal{W}(\mathbf{k}_0)$ must be unitary, the $a(|\mathbf{k}_0|)$ must be a pure phase $e^{i\theta(|\mathbf{k}_0|)}$. The Wilson loop operator thus reduces to:

$$\mathcal{W}_h(\mathbf{k}_0) = \begin{pmatrix} e^{i\theta(|\mathbf{k}_0|)} & 0 \\ 0 & e^{-i\theta(|\mathbf{k}_0|)} \end{pmatrix} = e^{i\sigma_z\theta(|\mathbf{k}_0|)}. \tag{3.13}$$

Because the Wilson loop operator is the exponent of only a single Pauli matrix, its eigenvalues are always complex conjugates. This means that choosing a series of concentric hexagonal Wilson loops, which are invariant under both TRS and C_3, enforces that the resulting WLS will necessarily be 'particle-hole' symmetric in the sense that the Wilson loop eigenvalues always have the same magnitude with opposite sign. The cyclic nature of the eigenvalues θ_j impose that they will necessarily be degenerate at $\theta = 0$ and π. Near these crossing points (denoted by $\mathbf{k}_\times$), we can expand the spectrum as

$$\theta(|\mathbf{k}\approx\mathbf{k}_\times|) = A + B(\mathbf{k}-\mathbf{k}_\times) + \dots \tag{3.14}$$

with $A \in \{0, \pm\pi\}$. These crossings can only be gapped by adding additional Pauli matrices that break either the T or C_3 symmetry, or by having the coefficient B vanish. The latter mechanism requires either two linear crossings to merge and annihilate, or a complete vanishing of the $\mathbf{k}$-dependence of $\theta(\mathbf{k})$.

Importantly, a full hexagonal Wilson loop contains redundant information due of the symmetries of the system, such that not all protected degeneracies in its spectrum are relevant. To extract meaningful topological information from a concentric WLS based on these types of loops, we need to consider the concentric WLS of a single fundamental domain of the BZ, as defined by the symmetries.[6] To determine what constitutes a fundamental domain, it is helpful to consider an infinitesimal Wilson loop, whose two eigenvalues describe the $U(2)$ Berry curvature F_j $(j = \{1, 2\})$, at an arbitrary point $\mathbf{k}$ in the BZ. The eigenvalues are not constrained to be particle-hole symmetric. However, three-fold rotational symmetry ensures that $F_j(\mathbf{k}) = F_j(g\cdot\mathbf{k})$, while TRS imposes that $F_j(\mathbf{k}) = F_j(-\mathbf{k})^\dagger = -F_{j+1}(-\mathbf{k})$. That is, the curvature eigenvalues of either of the two states in the Kramers pair considered are three-fold symmetric, and the curvature of one of the two bands is inverted with respect to the

[6] We've demonstrated the concept of a fundamental domain already, in Section 2.4.

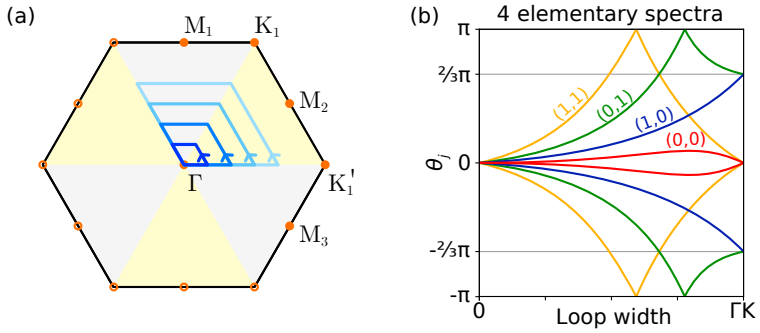

Figure 3.2: (a) Concentric Wilson loops covering the fundamental domain of a three-fold rotationally symmetric BZ. (b) The corresponding four elementary spectra (schematic), with topological indices indicated as $\mathbf{w} = (w_{\mathrm{FKM}}, w_\pi)$. Spectra with higher winding can be reduced to elementary ones upon addition of a topologically trivial Kramers pair with $\mathbf{w} = (0,0)$.

other. It then follows that a series of concentric loops covering two neighbouring sextants of the BZ captures all the symmetry-allowed information. From this we conclude that the fundamental domain of a $p3$ system consists of one third of the BZ, and the relevant topological information can be extracted from a WLS as shown in Figure 3.2. More generally, for a system with (only) n-fold rotational symmetry, the fundamental domain constitutes $1/n^{\mathrm{th}}$ of the BZ. As a side note, considering the full $\mathcal{C}_h$ loops may in some cases be favourable for minimising numerical error. You can determine the 1/3-BZ spectrum from the full-BZ one by unfolding the $\mathcal{C}_h$ spectrum (to access eigenvalues of magnitude larger than $\pm\pi$) and dividing the resulting values by three. The same applies to any T and C_n symmetric loop around Γ in other rotationally symmetric groups.

Now that we have introduced the concept of a concentric WLS, let us summarise their generic features. First, we've already mentioned that the eigenvalues of each of the loops in the spectrum come in pairs of opposite sign. A convenient feature of the loops we consider is that – because they enclose a finite region of the BZ – it is clear that they simply measure the $U(2)$ Berry curvature enclosed. Just like the $U(1)$ Berry curvature for single bands, the total $U(2)$ curvature in the BZ is quantised in multiples of 2π. A concentric WLS will always trivially start at zero (no curvature enclosed), and end at a value corresponding to $\pm(1/n)^{\mathrm{th}}$ of the total $U(2)$ Berry curvature present in the BZ. The total winding of the spectrum, times n, modulo 4π, therefore equals the FKM invariant. Additionally, we have already noted that linear crossings at $\theta_j = \pi$ can only be gapped by pair-wise annihilation. The parity of the number of times the spectrum crosses $\theta_j = \pi$ therefore constitutes a second topological invariant. Crossings through $\theta_j = 0$ do not carry the same protection. To see this, consider a spectrum starting and ending at $\theta_j = 0$ with one additional zero crossing in between. This spectrum may be reduced to a completely flat

full-BZ $U(2)$ WLS winding			invariants	$U(1)$ vortex
naïve	-12π	$+12\pi$	$(w_{\mathrm{FKM}}, w_\pi)$	locations
0	12π	12π	$(0,0)$	0
2π	10π	14π	$(1,0)$	Γ
6π	6π	18π	$(1,1)$	M
8π	4π	20π	$(0,1)$	$\Gamma + \mathrm{M}$

Table 3.1: How the winding of a $U(2)$ full-BZ concentric WLS is allowed to vary in $p3$. Without changing the topological phase, curvature in the bulk of the BZ is allowed to change by a multiple of 12π. On the left, we list three sets of topologically equivalent WLS windings per phase. Because all Wilson loop eigenvalues come in conjugate pairs, only the absolute value has any meaning. The middle column shows the associated invariants, and the right column indicates the corresponding vortices in the $U(1)$ Berry connection at the TRIMs, as discussed in [36].

spectrum ($\theta_j = 0$ for all loops in the spectrum) by transformations of the Hamiltonian that do not break any symmetries or constraints. Because the starting point of a concentric spectrum is fixed to $\theta = 0$, this flattening does not apply to π-crossings.

The right half of Figure 3.2 shows the four distinct types of WLS that one may obtain with the concentric loops indicated on the left half of the figure. We call these 'elementary spectra', because although spectra with higher windings are possible, they do not describe distinct topological phases. This is because in $p3$, $U(2)$ curvature can be created or annihilated within a single Kramers pair in steps of 12π without closing any gaps between distincts Kramers pairs. This does not change the value of the FKM invariant, nor the parity of the number of π-crossings in the 1/3-BZ concentric WLS. In Table 3.1 we list several equivalent amounts of winding, and their corresponding pair of invariants, listed as $\mathbf{w} = (w_{\mathrm{FKM}}, w_\pi)$. We also list the corresponding locations of $U(1)$ vortices at TRIM points, as envisioned in ref. [36]. Although the $U(1)$ curvature is ill-defined in the presence of TRS, and there is no way to measure these supposed $U(1)$ vortices, it is still a valid way of counting the number of distinct topological phases.

So far, we have only considered a single occupied Kramers pair, but the same method of concentric WLS works with multiple occupied Kramers pairs. $U(2)$ Wilson loops are only well-defined if all pairs of bands are separated from each other, but as already mentioned above, we can in principle smoothly deform the Hamiltonian (without closing the gap at E_{F} or breaking any symmetries) such that none of the Kramers pairs overlap, and then simply sum the invariants obtained from the $U(2)$ spectrum per pair. Because occupied Kramers pairs are allowed by symmetry to hybridise, we note that they can also exchange Berry curvature. We can imagine detecting this with a $U(2)$ WLS by comparing the spectrum before and after allowing two separated Kramers pairs to overlap, exhange curvature, and separate again. In this process, they can only exchange discrete amounts of curvature, which is again easiest to count by go-

ing to the framework of vortices in the $U(1)$ Berry connection; each $U(1)$ vortex will add 2π worth of Berry curvature to the BZ (of which our 1/3-BZ concentric WLS would pick up $2\pi/3$). Such an exchange of curvature between occupied Kramers pairs will never change the parity of the sum of the topological invariants, such that our classification is robust. This is in contrast to recently identified 'fragile topology', which describes apparent topological features that are not robust upon the adding of trivial bands [70, 96, 99, 106, 107]. Such features have been identified in for instance (linear) WLS and so-called 'Wannier obstructions', which means that occupied bands cannot be represented in terms of exponentially localised Wannier functions [70, 96, 99, 106, 107]. Their lack of robustness make them both conceptually less interesting, and significantly less likely to be relevant for any practical applications.

3.2. The extended Haldane model

Let us now apply our method to a model Hamiltonian with $p3$ symmetry. As explained in the previous section, we can describe all allowed topological phases in C_3-symmetric class AII systems by pairs of numbers $\mathbf{w} = (w_{\mathrm{FKM}}, w_\pi)$. The first of these corresponds to the FKM invariant, equal to the parity of $3/(2\pi)$ times the winding of the 1/3-BZ concentric WLS value, and a new invariant given by the parity of the number of π crossings in the spectrum. The latter has, to the best of our knowledge, not been identified in any model systems on the basis of phenomenological observations, and the complete and rigorous K-theory classification for TRS systems with three-fold rotational symmetry is also not known.

The Hamiltonian we consider is a TRS generalization of the Haldane model we introduced in Section 2.1, with hopping up to third-nearest neighbours [52, 108, 109]:

$$\begin{aligned} H &= \begin{pmatrix} H_{\mathrm{Hal}}^{+} & 0 \\ 0 & H_{\mathrm{Hal}}^{-} \end{pmatrix} \\ H_{\mathrm{Hal}}^{\pm} &= \sum_{\mathbf{k}} d_1(\mathbf{k})\tau_x + d_2(\mathbf{k})\tau_y + d_3^{\pm}(\mathbf{k})\tau_z \,. \end{aligned} \tag{3.15}$$

Here, τ_i are Pauli matrices for the sublattice degree of freedom, so that for example $\tau_x = a_\sigma^\dagger b_\sigma + b_\sigma^\dagger a_\sigma$, with $a_\sigma^\dagger$ and $b_\sigma^\dagger$ creation operators for electrons

with spin σ on different sublattices. We define

$$\begin{aligned} d_1 &= \sum_{j=1}^{3} [t_1 \cos(\mathbf{k}\cdot\mathbf{a}_j) + t_3 \cos(\mathbf{k}\cdot\mathbf{c}_j)]; \\ d_2 &= \sum_{j=1}^{3} [-t_1 \sin(\mathbf{k}\cdot\mathbf{a}_j) - t_3 \sin(\mathbf{k}\cdot\mathbf{c}_j)]; \\ d_3^{\pm} &= m \pm \sum_{j=1}^{6} t_2 (-1)^j \sin(\mathbf{k}\cdot\mathbf{b}_j). \end{aligned} \tag{3.16}$$

The vectors $\mathbf{a}_j$, $\mathbf{b}_j$ and $\mathbf{c}_j$ connect first, second, and third-nearest neighbours.[7] The inclusion of hopping integrals up to third-nearest neighbours allows for phases of H_{Hal} with Chern numbers larger than one [108, 109]. To lift the degeneracies between time-reversed states away from TRIMs,[8] we add a Rashba-type spin-orbit coupling connecting the time-reversed elements $H_{\mathrm{Hal}}^{\pm}$:

$$H_{\mathrm{R}} = i\lambda_{\mathrm{R}} \sum_{\mathbf{k}} \sum_{j=1}^{3} \sum_{\sigma\neq\sigma'} (\mathbf{c}_j \times \mathbf{s})_z^{\sigma\sigma'} e^{i\mathbf{k}\cdot\mathbf{c}_j} a_\sigma^\dagger b_{\sigma'} + \mathrm{h.c.} \tag{3.17}$$

Here σ is a spin index, $\mathbf{s}$ is the vector of Pauli matrices, and $a^\dagger$ and $b^\dagger$ are again creation operators for electrons on different sublattices. The extended Haldane model Hamiltonian, $H_{p3} = H + H_{\mathrm{R}}$, is invariant under TRS ($T = i\sigma_y \otimes \tau_0 \mathcal{K}$) and three-fold rotational symmetry ($C_3 = \exp\left(i\pi\sigma_z/3\right) \otimes \tau_0$).

To begin with, in Figure 3.3 we plot the $U(2)$ Berry curvature ($F_j(\mathbf{k})$) for this model, for a specific set of parameters. As mentioned in Section 3.1, TRS and C_3 symmetry impose that the curvature is three-fold symmetric and has opposite signs in for the two states in a Kramers pair. We computed the curvature by considering small Wilson loops surrounding a single 'pixel' in our plot, such that we obtain two eigenvalues per pixel. In such a numerical calculation, we cannot *a priori* assign a band label to each eigenvalue. However, by requiring that the Berry curvature is a continuous function (within the resolution of our computation), we can identify which sets of eigenvalues belong together.[9] This results in the figure, which beautifully demonstrates the symmetry-constrained structure of the $U(2)$ curvature.

[7] Explicitly: $\mathbf{a}_j = (R_3)^j(0,1)^{\mathrm{T}}$, $\mathbf{b}_j = (R_6)^j(\sqrt{3},0)^{\mathrm{T}}$ and $\mathbf{c}_j = (R_3)^j(0,-2)^{\mathrm{T}}$, where R_3 and R_6 are three and six-fold rotation matrices, respectively, and the inter-atomic distance is set to unity.

[8] This is not strictly necessary for determining the topological invariants from the concentric WLS, which for $p3$ is valid regardless of the number of degenerate states within a single Kramers pair of bands. However, it is useful for enlarging the gap in the finite-size computations described in Section 3.3.

[9] This is not always easy to do. It is often helpful to compare the magnitude of the $U(2)$ Berry curvature to a concentric WLS, in which this continuity condition is generally easier to identify.

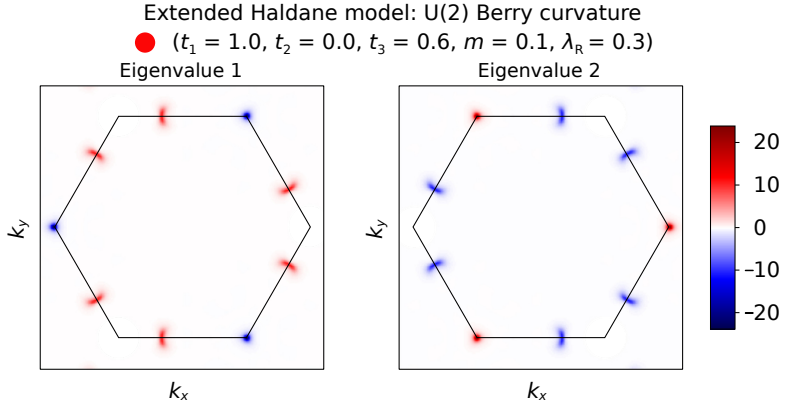

Figure 3.3: $U(2)$ Berry curvature of the extended Haldane model. The black hexagons indicate the size of the BZ. The parameters chosen here correspond to the red circle in Figure 3.4a. The curvature was computed as a grid of 200×200 square Wilson loops covering the area shown above.

We can compare this plot of the $U(2)$ curvature to what we see in a concentric WLS covering 1/3-BZ. The parameter set used in Figure 3.3 corresponds to the red curve in Figure 3.4b. This shows that despite the presence of some curvature in the bulk of the BZ, the total curvature sums to zero, such that the WLS does not wind. In terms of topological indices, this phase corresponds to $\mathbf{w} = (0, 0)$. By varying the second- and third-nearest neighbour hopping amplitudes (t_2 and t_3), we see that the total winding of the WLS changes. This gives us two other topological phases, with topological indices $\mathbf{w} = (1, 0)$ (blue) and $\mathbf{w} = (0, 1)$ (green). The fact that we find topologically non-trivial phases in this model doesn't come as a big surprise, because the underlying Haldane models have non-zero Chern numbers for the same regions of parameter space (aside from some changes induced by H_R) [108, 109]; the Chern numbers equal w_{FKM} modulo 2. The full phase diagram of the extended Haldane model, along with the magnitude of the Chern numbers of the individual $H^{\pm}_{Hal}$ Hamiltonians, is shown in Figure 3.4a.

3.3. Edge states and corner charges

Now that we have demonstrated that we have a model with three distinct topological phases, one might wonder whether they host any interesting physical features. The bulk-boundary correspondence requires edge states to be present in finite-sized materials whose bulk Hamiltonian has a non-trivial FKM invariant. Those derived from subsystems with even (non-zero) Chern numbers ($w_{FKM} = 0$) on the other hand, have no protection against their edge states being gapped. Additionally, a recent proposal suggests a bulk-corner correspondence in rotationally-symmetric topological insulators [84]. Intuitively, one expects a minimal requirement for topological corner charges to appear to

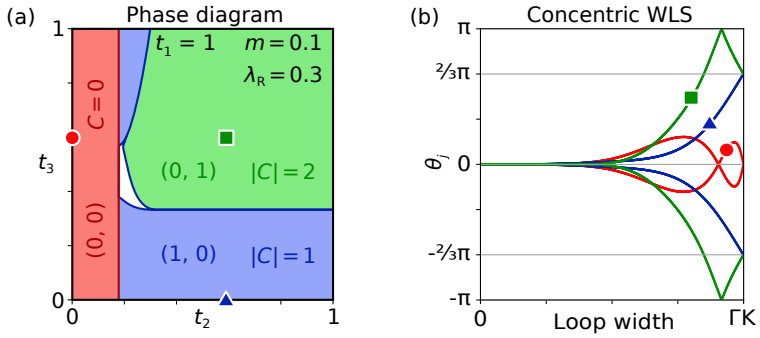

Figure 3.4: (a) The phase diagram of the extended Haldane model H_{p3} with $t_1 = 1$, $m = 0.1$, $\lambda_R = 0.3$. The red phase has trivial values for all topological indices, i.e. $\mathbf{w} = 0$. The blue and green phases are non-trivial with their respective $\mathbf{w} = (w_{\mathrm{FKM}}, w_\pi)$ indicated alongside the magnitude of the Chern numbers for $H^{\pm}_{\mathrm{Hal}}$ in each phase. In the white region the phase could not be unambiguously determined due to (the proximity to) a gap closing. (b) The concentric WLS over one third of the BZ for the three points indicated by corresponding symbols in the phase diagram.

be the presence of a winding WLS – indicating the presence of a non-trivial topology – with a trivial FKM invariant such that there are no protected edge states. Such a situation corresponds precisely to the $(w_{\mathrm{FKM}}, w_\pi) = (0, 1)$ phase as seen in the extended Haldane model. To see if this phase indeed hosts corner charges, we consider the extended Haldane model both on a finite-sized hexagon and in ribbon configurations, for the same sets of parameter values as highlighted by symbols in Figure 3.4. These were computed using the Pybinding Python package [110].

Let us consider the finite-sized case first, shown in Figure 3.5. As expected, the $\mathbf{w} = (0, 0)$ phase is a trivial insulator, and exhibits no edge or corner states. The $(1, 0)$ phase hosts topological edge states, as expected for a non-trivial FKM invariant. Interestingly, infinitely long ribbons with zigzag edges in the $(0, 1)$ phase exhibit fully localised corner charges for the chosen parameter values. However, varying the parameters while staying within the same topological phase demonstrates that in some cases, these states begin to delocalise around the edges of the hexagon. The corner charges are thus demonstrably able to hybridise with other states, and are thereby not entirely robust.

We can gather more insight from ribbon band structures. A 'ribbon' is constructed by making the lattice finite in one real-space direction, while maintaining an infinite lattice (or one with periodic boundary conditions) in the other, leaving a system with well-defined k-values in only one dimension. The honeycomb lattice structure of the model allows for two different (clean) terminations, commonly known as armchair or zigzag edges, which are constructed by breaking translational symmetry along the x or y directions, respectively. This distinction is important to make, because the two atoms in the unit cell (A and B) have different on-site energies ($\pm m$). While armchair edges host equal numbers of each of the A and B atoms on the edge, the two types of

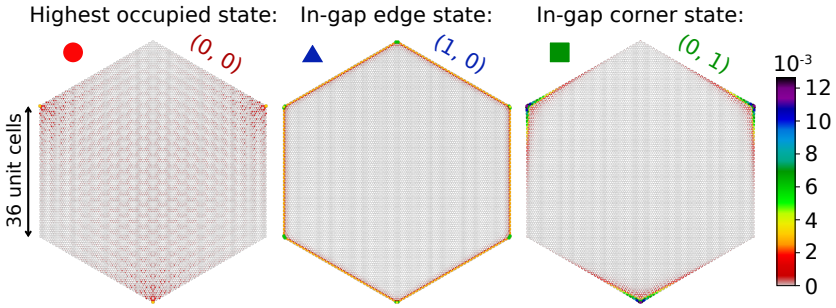

Figure 3.5: Exemplary states of the extended Haldane model in a finite-sized hexagon with armchair edges, for the three topological phases with parameter values as indicated by the symbols in Figure 3.4. The $(0,0)$ phase hosts no in-gap states, while the $(1,0)$ phase hosts in-gap edge states and the $(0,1)$ phase hosts in-gap corner states. The colour scale indicates the local density of states, normalised to one in each panel. The states shown lie at $E/t_1 = -0.2$, 0, and -0.05, respectively.

sites making up the zigzag edge will have different species of outermost atoms, breaking this sublattice symmetry. Figure 3.6 shows numerically evaluated one-dimensional band structures for systems with both armchair and zigzag edges [110], where we considered widths of 49 and 28 unit cells respectively, so that the ribbons have equal real-space width when the lattice geometry is taken into account.

In all three topological phases, the bulk system is an insulator, while edge states should show up in the ribbon geometry as in-gap states. In Figure 3.6, we highlight the four states closest to $E = 0$ in red. In the $\mathbf{w} = (0,0)$ phase, these red states do not cross the gap and act like bulk states. For zigzag-edged ribbons, two of these bands become almost completely flat, which is likely due to charge localisation on the outermost atoms in the zigzag edges. This is made possible by the different on-site energies on A and B-type atoms in the unit cell. In contrast, the $(1,0)$ phase contains edge states crossing the band gap, as expected for a system with non-trivial FKM invariant. Note that these edge states are two-fold degenerate in the armchair-edged ribbons, while this degeneracy is broken in the zigzag-edged ribbons. Finally, in the $(0,1)$ phase, we find that the in-gap armchair edge states become gapped, while the zigzag edge states remain. The energies of corner states seen for this phase in Figure 3.5 lie within the spectral gap between the armchair edge states. However, the corner state energies may be moved away from this small spectral gap and hybridise with other states, allowing them to spread out along the edges and potentially even into the bulk. We conclude from this that even if the system has a gap in both the bulk and edge state spectrum, the existence of corner charges additionally requires their energies to lie within this gap. A non-trivial value of the newly identified invariant ($w_\pi = 1$) thus signals the possibility of corner charges emerging, but whether they are realised in any specific finite-sized system depends on its detailed configuration.

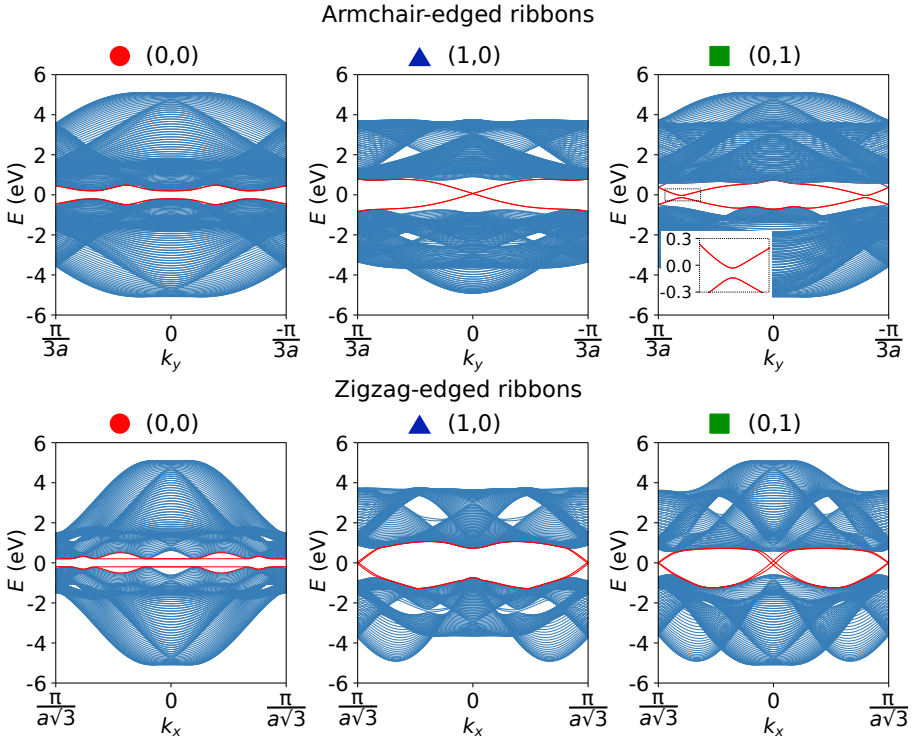

Figure 3.6: Bandstructures for ribbons with armchair or zigzag edges, of the extended Haldane model with parameter values as indicated by the symbols in Figure 3.4. The different parameter choices correspond to three different topological phases, with the indicated topological indices. Highlighted in red are the four states closest to the Fermi level.

An interesting area to further explore would be the protection of edge states against gapping in the various ribbon geometries. For the $(1,0)$ phase, the armchair edge states form a two-fold degenerate crossing, while the breaking of sublattice symmetry in the zigzag-edged ribbon splits the edge states into two non-degenerate crossings. Each such crossing contains two edge states, localised on opposite edges of the ribbon. These crossings are thus protected from opening a gap by the suppression of their overlap due to the large real-space distance between edges. States in different crossings on the other hand, are time-reversed partners, and cannot scatter into one another without breaking time-reversal symmetry. Edge states in the $(1,0)$ phase are thereby always topologically protected.

In the $(0,1)$ phase, the number of zero energy crossings is doubled as compared to the $(1,0)$ phase. In this case, each side of the ribbon hosts two pairs of edge states connected by time-reversal symmetry. If two states on the same side of the ribbon that are not time-reversed partners can be brought together in k_x-space, they can be gapped. This happens in the armchair geometry. For the zigzag-edged ribbon in Figure 3.6, states with the same real-space local-

isation that are not time-reversed partners are still separated in momentum, and therefore not gapped. It may be possible to move the edge state crossings in k_x space by tuning model parameters until they meet and open a gap by hybridising. Similarly, the addition of impurities that break the translational symmetry along the ribbon edge and allow scattering without conserving k_x may also lead to a gap opening in the edge spectrum. In the presence of such a gap, it may be expected that corner charges could be stabilised also for finite hexagon-shaped systems with zigzag edges.

3.4. Discussion and conclusion

To conclude, we have shown that the concentric Wilson loop spectrum serves as a simple diagnostic allowing the simultaneous evaluation of both the well-known FKM invariant, and a new topological invariant given by the parity of the number of π-crossings in the spectrum. The latter was predicted to exist in rotationally symmetric systems based on K-theoretical arguments [36, 91], but this is the first demonstration of an explicit way to calculate it. We demonstrated our method using an extended, time-reversal invariant version of the famous Haldane model with three-fold rotational symmetry, but stress that the approach is general and can also be applied to cases with other rotational symmetries. In even-fold rotationally symmetric systems, we can complement the concentric Wilson loop spectrum with LBO line invariants, which are given by the eigenvalues of Wilson loops along linear high-symmetry lines in the BZ. Combining rotations with additional symmetries, including non-symmorphic ones, may be expected to further enrich the analysis.

In wallpaper group $p3$, we showed our new invariant (w_π) signals the possibility of localised corner charges appearing in finite-sized samples. This may explain the recent observation of corner charges in specific rotationally symmetric systems, which were suggested to be related to a form of fragile topology [84]. Because the parity of π-crossings in the concentric Wilson loop spectrum is unaffected by the addition of topologically trivial Kramers pairs, the present analysis in fact suggests the bulk-corner correspondence in these systems to be stable and described by a true, rather than fragile, topological invariant. While further investigation is required, the existence of this stable invariant is not visible in the usual linear Wilson loop spectrum, underlining the utility of the concentric Wilson loops.

With this, we conclude Part I of this thesis. We have demonstrated that a non-trivial winding of the phase of Bloch wavefunctions in crystalline insulators can lead to topological phases of matter, which can result in interesting effects such as edge states and corner charges via a bulk-boundary correspondence. Historically, our understanding of topology has been predominantly based on the concepts of a geometric Berry phase and Chern number, which are valid for isolated electronic bands. In this chapter, we have focussed on how to generalise these concepts using a non-Abelian form of the Berry connection and $U(2)$ Wilson loops. Additionally, this brings us closer to a more complete

understanding of the role of lattice symmetries, which can strongly constrain the allowed structure of the ($U(1)$ and $U(2)$) Berry curvature.

Of course, we are far from done. The method of concentric Wilson loops presented here generalises to all rotational symmetry groups, but we note that in the presence of an even-fold rotational symmetry, the picture of $U(1)$ vortices as introduced in ref. [36] is complicated by the fact that vortices are allowed to sit at any (accidental) degeneracies within a single Kramers pair, in the bulk of the BZ. In $p3$ this isn't an issue, because TC_3 doesn't map a $\mathbf{k}$-point back onto itself, and therefore one can only introduce or remove two $U(1)$ vortex-antivortex pairs at a time within the fundamental BZ domain; this only allows changes of 12π to the full-BZ WLS winding. In any wallpaper group with C_2 symmetry, the fundamental domain can host single extra $U(1)$ vortex-antivortex pairs, which means the winding in a full-BZ concentric WLS of an n-fold rotationally symmetric system is allowed to change by $2\pi n$. While this won't affect the FKM invariant nor LBO invariants along high-symmetry lines, an extra degeneracy in the BZ bulk may change the value of w_π. As it stands, our new invariant is thus only well-defined in even-fold rotational wallpaper groups in the absence of accidental degeneracies in the BZ bulk. Conversely, one can use a concentric WLS to detect such extra degeneracies, by comparing the FKM and LBO invariants with the winding of the spectrum.

An important next step is to find a way to circumvent such restrictions. Ideally, we would like to have a diagnostic that is directly applicable to the bandstructure of any real material, regardless of how many band crossings there are within individual Kramers pairs and between Kramers pairs. While we can easily compute a full $U(N_{\mathrm{occ}})$ WLS, the symmetry-imposed restrictions on the eigenvalues are much less powerful than the restrictions on $U(2)$ spectra. An important future direction is thus to determine what, if any, topological invariants we can extract from a $U(N_{\mathrm{occ}})$ spectrum. A different, complementary direction is to generalise the present method to wallpaper groups with additional symmetries present, such as reflections and inversion symmetry. Using the same analysis of symmetry constraints as presented in Section 3.1, we expect that concentric WLS will be useful in all two-dimensional crystals. Finally, we would like to generalise our methods to all 230 three-dimensional space groups. Intuitively, one might expect that for a system in *e.g.* space group $P3$, one could simply compute the $U(2)$ concentric WLS for a series of different k_z-values; however, away from high-symmetry planes ($k_z = 0$ and π), the loops will no longer be symmetric under TRS, such that we should be careful when considering the symmetry restrictions. More generally, the assumption that a three-dimensional quantum spin Hall (QSH) insulator may be built up by stacking two-dimensional QSH planes also has some caveats, as demonstrated recently in ref. [111].

All in all, we have found a new topological invariant, which completes the topological classification of wallpaper group $p3$. While the story is far from being done, the general approach of searching for symmetry restrictions on the

($U(2)$) Berry curvature is a clear way forward in this field. Importantly, the use of Wilson loops precludes the need for any gauge-fixing of Bloch states in the BZ (which was an issue for invariants derived from so-called 'partial polarisations' [65, 95]), and establishes a clear, intuitive link between the symmetries of the system and Berry curvature. This paves a way forward in which it is easier to define and compare different types of invariants.

II

Electron-phonon coupling and charge order

4

Introduction to charge order

In Part I of this thesis, we considered the influence of lattice symmetries on the topological phases of electrons in a crystal. The approach used there assumes that electrons do not interact among themselves, nor do they interact directly with the vibrational modes of the lattice (collective excitations known as *phonons*). In this Part, we will move away from topology and consider electronic ordered phases made possible by such interactions. Unlike topological phases, of which there may be many within a single symmetry class, the phases we consider here are always delineated by phase transitions that change the symmetries of the system. Specifically, the transition to a charge-ordered phase always breaks the translational symmetry of the lattice.

Density waves of charge, spin, or orbital occupation play a central role in determining the physical properties of many materials, ranging from elements [7, 112], to cuprate high-T_{CDW} superconductors [113–115], pnictides [116, 117], complex oxides [118–120], and (multi)ferroics [17, 20, 23, 121]. Understanding the mechanisms driving density wave formation is important for understanding their interplay with other types of order, and is key in tuning phases of matter to obtain ideal properties for applications [122–124].

Before moving on to two specific case studies of *charge density waves* (CDWs) in a real material in the next two chapters, this chapter will first introduce the general concept of charge order, and how to describe it. Throughout this chapter, we will focus on the most common mechanism underlying CDW order, based on the combination of an electronic instability and atomic distortions cooperatively driving the CDW formation. To do so, we start by introducing the Peierls model, in Section 4.1. After a brief discussion of the limitations of this model, we continue in Section 4.2 by generalising the Peierls model to a set of models with more than one atom per unit cell. Doing so, we demonstrate

what features allow for CDWs that go beyond the simple Peierls description. Finally, in Section 4.3, we move on to introducing field-theoretical methods that can be used to (quantitatively) describe charge order. It is these methods that we will use in Chapters 5 and 6.

4.1. The Peierls model

Let us begin with the most basic model for charge order, named after Rudolph Peierls. This model is based on the simplest possible one-dimensional (1D) crystal, which Peierls found to be inherently unstable to the formation of a CDW [125, 126]. That is, electrons in this 1D lattice, when coupled to phonons, prefer to spontaneously break the lattice symmetry to form plane waves of charge density. The transition to the CDW state is associated with the opening of an energy gap around the Fermi level in the electronic spectrum, as well as the softening (energy going to zero) of a phonon mode at the wavevector[1] of the CDW.

The 1D lattice considered by Peierls has a single atom per unit cell, and lattice spacing a. It is depicted in Figure 4.1. From a simple tight-binding model in which electrons are allowed to tunnel from one atomic site to a neighbouring atom, we obtain the 'bare' electron Hamiltonian[2]

$$H_{\mathrm{e}} = \sum_j \left[\mu\, c_j^\dagger c_j - t\left(c_j^\dagger c_{j+1} + c_{j+1}^\dagger c_j\right)\right]. \tag{4.1}$$

Here, $c_j^\dagger$ creates an electron on site j, μ is the on-site potential and t is the hopping amplitude. We can diagonalise this Hamiltonian by applying the Fourier transform $c_j = (1/\sqrt{N})\sum_k e^{ikja} c_k$, from which we obtain the bare electron energies

$$\epsilon_k = -2t\cos(ka) + \mu. \tag{4.2}$$

From here on, we will set $\mu = 0$, such that the single electronic band is half-filled and crosses the Fermi level (E_{F}) at $k_{\mathrm{F}} = \pm\frac{\pi}{2a}$.

Above, we implicitly used the Born-Oppenheimer approximation, in which the atomic cores that make up the lattice are assumed to be unaffected by the motion of electrons, and so remain stationary. Conversely, we can consider the classical equation of motion for the atomic cores from a simple ball-and-spring model:

$$M\frac{\partial^2 u_j}{dt^2} = K\left[\left(u_{j+1} - u_j\right) + \left(u_{j-1} - u_j\right)\right], \tag{4.3}$$

with M the mass of the atoms, K the effective spring constant of the chemical bonds connecting them, and u_j the displacement along the chain of atom j.

[1] In 1D, the CDW technically has a wave*number* rather than a wavevector. Because much of the present discussion will generalise to systems of higher dimensions, I prefer to use the term 'wavevector' throughout.

[2] By 'bare' we mean non-interacting, free. In the presence of interactions, quasiparticles get 'dressed' and fields get 'renormalised'.

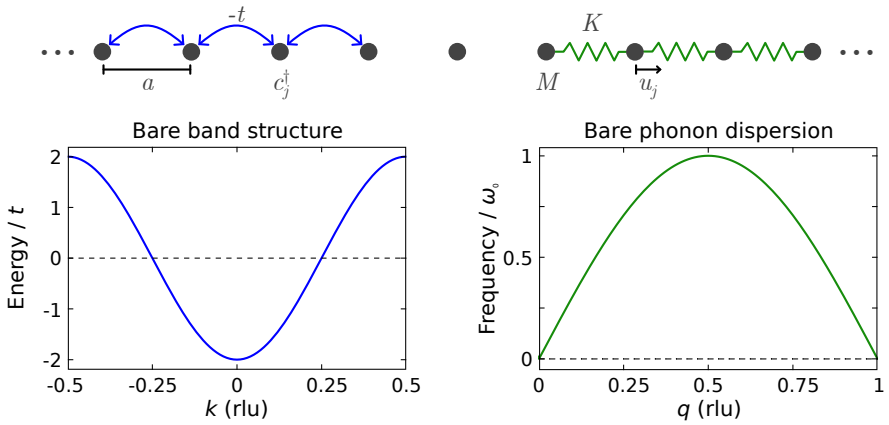

Figure 4.1: The 1D atomic chain considered in the Peierls model. This system hosts both electrons and phonons. If we first neglect the interaction between the two, we can derive a 'bare' electron dispersion from a tight-binding model (left) and a bare phonon dispersion from a classical ball-and-spring model (right). 1 rlu $= 2\pi/a$ is a reciprocal lattice unit.

We can solve this using the Ansatz $u_j = u\, e^{iqja - i\Omega_q t}$, by which we find the bare phonon dispersion[3]

$$\Omega_q = \omega_0 \left|\sin\left(\frac{qa}{2}\right)\right|, \tag{4.4}$$

where $\omega_0 = 2\sqrt{K/M}$. Throughout this thesis, we will use k to denote electron momenta, and q to denote phonon (or other bosonic) momenta.

Since atomic displacements will directly affect the likelihood of an electron to tunnel from one atom to another (described by t), we expect electrons and phonons to couple to one another. This coupling can be described by a Fröhlich Hamiltonian [128, 129]:

$$H = \sum_k \epsilon_k c_k^\dagger c_k + \sum_q \hbar\Omega_q b_q^\dagger b_q + \frac{1}{\sqrt{N}} \sum_k \sum_q g_{k,k+q} c_k^\dagger c_{k+q} (b_q^\dagger + b_{-q}). \tag{4.5}$$

The first term describes the bare electrons with creation operators $c_k^\dagger$, the second the bare phonons with creation operators $b_q^\dagger$, and the final term describes the interaction, assuming N lattice sites per unit length and electron-phonon coupling (EPC) matrix element $g_{k,k+q}$. The interaction can be understood as follows: upon annihilating a phonon with wavevector $-q$, or upon creating a phonon with wavevector q, an electron will scatter from wavevector $k+q$ to a state at wavevector k, with scattering amplitude $g_{k,k+q}$. Generically, the (largest) phonon energy will be two orders of magnitude smaller than the bandwidth of the electronic band ($4t$), such that phonons can only scatter electrons in states near E_F.

[3]The bare phonon dispersion can also be derived quantum-mechanically, giving the same result. See for instance ref [127], Chapter 1.

Now that we have a Hamiltonian, we can use mean-field (MF) theory to determine how electrons and phonons are affected by the coupling [128, 130, 131]. To do so, we treat the electrons as living in the MF background provided by the phonons, and vice versa. Note that this kind of treatment assumes $g_{k,k+q}$ to be small, *i.e.* we are in the weak-coupling regime. Because we know that only the electronic states near the Fermi level can be scattered by phonons, we consider the limit in which only the phonons with momentum $Q = 2k_{\mathrm{F}} = \pi/a$ play a role.[4] This corresponds to taking the zero-temperature limit. We then obtain two new MF Hamiltonians as follows:

$$\begin{aligned} H_{\mathrm{e}}^{\mathrm{MF}} &= \sum_k \epsilon_k c_k^\dagger c_k + \frac{1}{\sqrt{N}} \sum_k g_{k,k+Q} c_k^\dagger c_{k+Q} (\langle b_Q^\dagger \rangle + \langle b_{-Q} \rangle); \\ H_{\mathrm{ph}}^{\mathrm{MF}} &= \sum_q \hbar\Omega_q b_q^\dagger b_q + \frac{1}{\sqrt{N}} \sum_k g_{k,k+Q} \langle c_k^\dagger c_{k+Q} \rangle (b_Q^\dagger + b_{-Q}). \end{aligned} \tag{4.6}$$

Above, $\langle \dots \rangle$ indicates the expectation value.

$H_{\mathrm{e}}^{\mathrm{MF}}$ is straightforwardly diagonalised as follows:

$$E_\pm(k) = \frac{\epsilon_k + \epsilon_{k+Q}}{2} \pm \sqrt{\left(\frac{\epsilon_k - \epsilon_{k+Q}}{2}\right)^2 + |\Delta|^2}, \tag{4.7}$$

where we have identified the order parameter

$$\Delta = \frac{1}{\sqrt{N}} g_{k,k+Q} (\langle b_Q^\dagger \rangle + \langle b_{-Q} \rangle). \tag{4.8}$$

Conventionally, one actually neglects the k-dependence of $g_{k,k+Q}$, such that the order parameter is – as is expected – a simple scalar. We will return to this point later. When plotting $E_\pm(k)$, it is immediately clear that the two bands correspond to the upper and lower halves of ϵ_k and ϵ_{k+Q}, with an energy gap of size 2Δ at E_{F} (see Figure 4.2). Opening a gap here corresponds to an overall lowering of energy, as (at low temperatures) occupied electronic states are pushed down in energy while only unoccupied states are pushed up.

To diagonalise the MF phonon Hamiltonian, we consider $H_{\mathrm{ph}}^{\mathrm{MF}}(q{=}Q)$. (The remaining q-values of the phonon dispersion remain unchanged from the bare phonon Ω_q.) Using the transformation $b_Q = a_Q + \alpha$ with α some scalar, we can rewrite it as

$$H_{\mathrm{ph}}^{\mathrm{MF}}(q{=}Q) = \hbar\Omega_Q (a_Q^\dagger a_Q - \alpha^2), \tag{4.9}$$

where we have identified

$$\alpha = -\frac{\sum_k g_{k,k+Q} \langle c_k^\dagger c_{k+Q} \rangle}{\sqrt{N}\hbar\Omega_Q}. \tag{4.10}$$

[4] In this special case of the half-filled chain, $Q = -Q$.

Notice that by coupling to electrons, the ground state energy is reduced. Importantly, because we have identified a diagonal basis in terms of the number of phonons ($|n\rangle = (n!)^{-\frac{1}{2}}(a_Q^\dagger)^n\,|0\rangle$), we can now evaluate

$$\langle b_Q^\dagger\rangle = \langle a_Q^\dagger\rangle + \alpha = \frac{\sum_n \langle n|\, a_Q^\dagger\, |n\rangle\, e^{-\beta E_n}}{\sum_n e^{-\beta E_n}} + \alpha = 0 + \alpha, \tag{4.11}$$

and similarly $\langle b_{-Q}\rangle = \alpha$. Filling this result back into Equation 4.8, we find

$$\Delta = -\frac{2}{\sqrt{N}} g_{k,k+Q} \sum_{k'} g_{k',k'+Q} \langle c_{k'}^\dagger c_{k'+Q}\rangle, \tag{4.12}$$

or, if we neglect the k-dependence of g:

$$\Delta = -\frac{2}{\sqrt{N}} g_Q^2 \sum_{k'} \langle c_{k'}^\dagger c_{k'+Q}\rangle = -2g_Q^2 \langle \rho_Q\rangle. \tag{4.13}$$

Here, $\rho_Q \equiv \frac{1}{\sqrt{N}} \sum_k c_k^\dagger c_{k+Q}$ is the Fourier transform of the real-space (charge) density operator $\rho(x) = c_x^\dagger c_x$. The size of the gap in the electronic spectrum thus correlates with the expectation value of a periodic modulation of charge density with wavevector Q. This is also reflected in that our derivation demonstrates that $\langle b_Q^\dagger b_Q\rangle = \alpha^2 \neq 0$ at zero absolute temperature.

Putting all we've seen together, we conclude that inducing a periodic modulation of charge density – a CDW – with the specific wavevector $Q = 2k_\mathrm{F}$ will result in the opening of a gap around E_F in the electronic spectrum, thereby lowering the total energy of the system. Importantly, the wavevector of the CDW is determined by the Fermi momenta; if we would change the chemical potential μ, the Fermi momenta would change, and the system would naturally prefer a CDW with a different wavevector.[5] The formation of the CDW is driven by EPC, and as such it is always accompanied by a periodic lattice distortion. While everything so far has been derived for $T = 0\,\mathrm{K}$, we note that at the CDW ordering temperature T_CDW, the energy of the phonons dressed by electron-phonon interactions will go to zero for wavevector Q. At this temperature, the energy gain of forming a CDW exactly counters the elastic energy cost of displacing atoms in the periodic lattice distortion. This lowering of the dressed phonon energy is called the *Kohn anomaly* [132], an effect we return to in Section 4.3.1. We summarise all of this in Figure 4.2.

This concludes the MF treatment of the Peierls model. It is widely assumed that the general mechanism behind the CDW formation in the Peierls model is the same as what drives CDW formation in many real materials. To make such a generalisation, it is important to be aware of the specific assumptions made in the present model. For one, we implicitly assumed here that the EPC was

[5] In a MF treatment, going away from half-filling complicates the maths slightly, but the results are essentially the same. See for instance refs. [128, 130, 131].

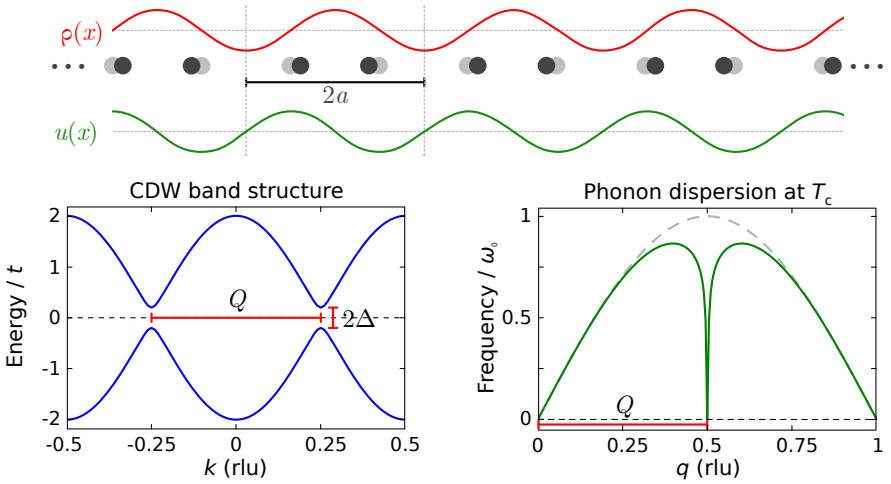

Figure 4.2: The formation of a charge density wave (CDW) and associated periodic lattice distortion (PLD) results in a doubling of the unit cell, and a gap opening in the electronic spectrum ($E_{\pm}(k)$). At the CDW ordering temperature, the dressed phonon energy at wavevector Q goes to zero. This is not captured by the zero-temperature MF treatment presented thus far; we will derive this phonon softening effect in Section 4.3. 1 rlu $= 2\pi/a$.

weak, such that despite the electron-phonon interactions, we have (relatively) long-lived and well-defined quasiparticles. Otherwise, our second-quantised operators would no longer be meaningful. Importantly, we also assumed here that the EPC matrix elements $g_{k,k+q}$ don't depend on momentum k. We will demonstrate in Section 4.3 and Chapter 5 that this is a crude approximation to make, and certainly doesn't hold generically – even for 'weak-coupling' materials!

Second, the Peierls model is purely one-dimensional. This means there are only two Fermi momenta, which can always be connected by a single wavevector Q. However, ungapped systems in two dimensions will have one or more lines of Fermi momenta, and three-dimensional metals have a Fermi surface (FS, which may consist of multiple parts). From here on, we will call the set of Fermi momenta a FS, regardless of its dimensionality. For phonons of a single wavevector $\mathbf{Q}$[6] to be able to scatter electrons from a significant number of states at the Fermi level to another state at the Fermi level requires the FS to have large parallel sections. If this is so, then the FS is *nested*, with $\mathbf{Q}$ the *nesting vector*. While (partial) nesting occurs in a small subset of materials, it is never perfect. This means that in real materials there is a more delicate energy balance at play – the total energy gained by opening a (localised) gap should be compared to the elastic energy cost of displacing atoms.

Another feature that makes the Peierls model so simple is that it assumes that the only interaction is EPC. However, electron-electron interactions may also play a role. That Coulomb interactions might be relevant for charge or-

[6]Now an actual wave*vector*.

der is clear from the idealised example of a half-filled 1D chain with nearest-neighbour Coulomb interactions (without EPC). In this system – the Coulomb-interaction analogy to the Peierls model – electrons will localise on every second atom, forming a so-called *Mott insulator*. (Notice that in this case, as there is no coupling to phonons, the charge order has no associated periodic lattice distortion.) In Chapter 6, we will see that electron-electron interactions are also important to consider in real, low-dimensional materials. The low dimensionality is relevant, because when there is less material to screen the electric field, the Coulomb interaction will be stronger. One can imagine that the field travels through the vacuum or air outside the material, bypassing the screening effect of all the electrons bound to the material.

Lastly, the Peierls model only has a single site per unit cell. Most materials are composed of more than one type of element, and even those made of a single type of atom may have more than one type of valence orbital. Orbital order, in which a CDW is accompanied by a modulation of orbital occupation throughout the crystal, has been shown in various materials, including elemental chalcogens [7]. In this specific example, the combined charge and orbital order can be understood as arising from interactions between three concomitant CDWs, each involving charge transfers between specific orbital species in neighbouring unit cells. More generally, systems with multiple atomic sites per unit cell may host charge (and orbital) order that involves specific charge transfers within a unit cell, rather than between unit cells. Furthermore, the anisotropic nature of atomic orbitals means that such orbital-specific charge transfers may naturally lead to atomic displacements that do not align with the CDW propagation direction; this is evidenced by *e.g.* $TiSe_2$ [133]. The Peierls model does not provide a clear roadmap for treating charge order in multi-band systems; we will explore this in the following section.

4.2. Multi-band charge order

Having discussed charge order in the simplest possible 1D crystal, let us consider what can change upon going to more complex lattices. We're not interested in performing extensive calculations, but we aim to obtain a qualitative picture by systematically building up from the Peierls model. Here, we will not discuss the role of the momentum- and orbital structure of the EPC, as this will be discussed at length in Section 4.3 and Chapter 5. We will also not delve into the role of dimensionality, nor interactions beyond EPC. Instead, we will demonstrate that even in simple 1D lattices, a single CDW may arise which involves charge transfers unlike the plane-wave form seen in the Peierls model.

To begin with, we can consider coupling several vertically aligned Peierls chains together, as shown in Figure 4.3. Assuming all atoms to be identical, and to host a single type of (isotropic) orbital, the non-interacting tight-binding

Hamiltonian for such a system with n coupled chains is given by:

$$\begin{aligned} H_{\mathrm{e}} = &\sum_{j}\sum_{\nu=1}^{n}\left[\mu\, c^{\dagger}_{j,\nu}c_{j,\nu} - t_1\left(c^{\dagger}_{j,\nu}c_{j+1,\nu} + c^{\dagger}_{j+1,\nu}c_{j,\nu}\right)\right] \\ &+ \sum_{j}\sum_{\nu=1}^{n-1}\left[-t_2\left(c^{\dagger}_{j,\nu}c_{j,\nu+1} + c^{\dagger}_{j,\nu+1}c_{j,\nu}\right)\right], \end{aligned} \tag{4.14}$$

where we assumed that electrons can only hop to their nearest neighbours. j labels the site index along the chains (*i.e.* the unit cell), ν labels the different chains (*i.e.* the site within the unit cell), μ indicates the on-site potential, t_1 describes hopping along the chains and t_2 describes interchain hopping. Notice that for $n = 1$, the above reduces to Equation 4.1. Taking the Fourier transform of this Hamiltonian, one obtains a tridiagonal $n \times n$ Bloch Hamiltonian with $\epsilon_k = \mu - 2t_1\cos(ka)$ on the diagonal, sandwiched between elements of $-t_2$:

$$H_{\mathrm{e}} = \begin{pmatrix} c^{\dagger}_{k,1} & c^{\dagger}_{k,2} & c^{\dagger}_{k,3} & \cdots \end{pmatrix} \begin{pmatrix} \epsilon_k & -t_2 & 0 & \cdots \\ -t_2 & \epsilon_k & -t_2 & \ddots \\ 0 & -t_2 & \epsilon_k & \ddots \\ \vdots & \ddots & \ddots & \ddots \end{pmatrix} \begin{pmatrix} c_{k,1} \\ c_{k,2} \\ c_{k,3} \\ \vdots \end{pmatrix} \tag{4.15}$$

Diagonalising these matrices, the bare electronic spectrum of n coupled Peierls chains has n bands identical to that of the original Peierls chain, offset from one another in energy by some factor proportional to t_2. To simplify a direct comparison to the previous section, we'll only consider the half-filled case by setting $\mu = 0$ from here on. As can be seen in Figure 4.3, we find that no matter how many Peierls chains we couple,[7] states at the Fermi level always come in pairs, lying exactly $Q = \pi/a$ apart. In direct analogy to the original Peierls model, this suggests that these systems are susceptible to the formation of a CDW with wavevector Q.

While we won't perform a full MF calculation as in the previous section, we will use intuition from what we've seen so far to predict a lattice distortion corresponding to the type of CDW we expect. For any such distorted lattice, we can again use a tight-binding model to find the electronic spectrum.[8] Any valid CDW Ansatz must open a gap around the Fermi level. In the present case, we know to expect a CDW with period 2, such that the unit cell must double. If we simply assume a Peierls-like CDW will form in every chain, we can obtain the CDW band structures shown in the bottom two panels of Figure 4.3. The tight-binding Hamiltonians for the distorted lattices are derived in Appendix A.1. Indeed, we find that the entire FS is gapped out!

[7] We assume here that n is small enough for the system to still be effectively one-dimensional; otherwise we'd have to consider the shape of the two-dimensional FS.

[8] Notice that this approach only works for commensurate CDWs.

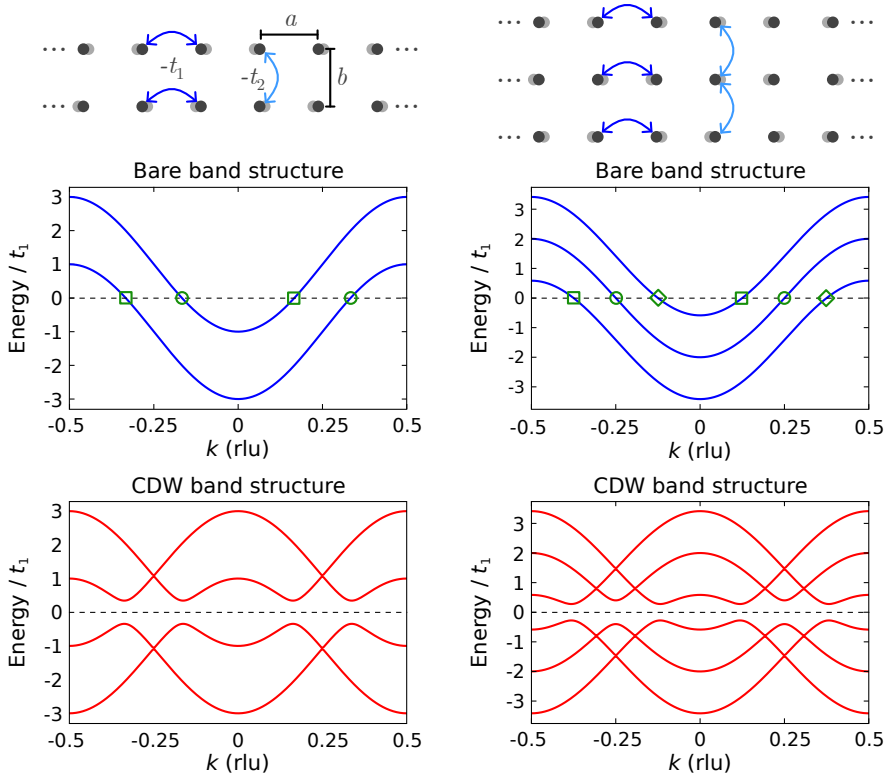

Figure 4.3: Two (left) and three (right) vertically aligned, coupled Peierls chains. At half-filling, Fermi momenta of the bare electronic spectra (highlighlighted by green shapes in the middle plots) always come in pairs, lying exactly $Q = \pi/a$ apart. This means a single period-2 CDW can gap out the entire Fermi surface, in direct analogy with the Peierls model. The grey circles indicate the CDW-induced periodic lattice distortion that was used to calculate the band structure in the CDW phase (bottom plots). The plot parameters are $t_1 = t_2 = 1$; $\mu = 0$; 1 rlu $= 2\pi/a$.

One thing to notice is that neighbouring chains necessarily host period-2 CDWs that are π out of phase. The alternative Ansatz where all chains host in-phase distortions does not open a gap at E_F.[9] This means that as soon as there is more than one site per unit cell, the charge-density modulations in these Peierls-like models are no longer described by an overall, single scalar plane-wave modulation as depicted in Figure 4.2. Instead, each chain has its own distinct CDW modulation. That the neighbouring chains prefer to have CDWs that are out of phase with one another shouldn't come as a big surprise, considering that a phonon of wavevector Q will scatter electrons from one band into another (note the pairwise matching shapes in Figure 4.3). The bands consist of (orthogonal) linear combinations of the original atomic orbitals. In

[9]This alternative Ansatz does open gaps, but above and below E_F in the middle of each individual band; these are precisely the regions within each band that are connected by Q.

the case of $n = 2$, the original two bands correspond to the dispersions of the bonding and antibonding states within each unit cell; the eigenvectors of the two bands are $(1/\sqrt{2}, \pm 1/\sqrt{2})$, independent of momentum k. A Q-phonon will thus always scatter an electron from a bonding to an anti-bonding state, or *vice versa*. This naturally results in a CDW displacement in opposite directions for the two types of atom in the unit cell. For $n = 3$, it's slightly more convoluted – the middle band has eigenvector $(1/\sqrt{2}, 0, -1/\sqrt{2})$, while the outer bands have eigenvectors $(1/2, \pm 1/\sqrt{2}, 1/2)$ – but the principle remains the same.

One pertinent question is to what extent this type of order deviates from the standard Peierls description. In Section 4.1, we started with the Fröhlich Hamiltonian describing EPC, and found that the MF CDW order parameter Δ is proportional to $\sum_k \langle c_k^\dagger c_{k+Q} \rangle$. In multiband systems, the Fröhlich Hamiltonian generalises to

$$H = H_{\mathrm{e}} + H_{\mathrm{ph}} + \frac{1}{\sqrt{N}} \sum_{k,q,\nu,\lambda,\eta} g_{k,k+q}^{\nu,\lambda,\eta} c_{k,\nu}^\dagger c_{k+q,\lambda} (b_{q,\eta}^\dagger + b_{-q,\eta}), \tag{4.16}$$

where we have introduced the electron band labels ν, λ and the phonon mode label η. Note that here, the c and b operators indicate the relevant electron and phonon *normal modes*. That is, they represent operators for those orthogonal linear combinations of orbitals and atomic displacements that one obtains after diagonalising the Bloch Hamiltonian and dynamical matrix, respectively.

Importantly, the relevant electron-phonon interaction may now consist of pairings of different species of electrons and phonons, each with their relevant scattering amplitude $g_{k,k+q}^{\nu,\lambda,\eta}$. This is something not described by the overly simplified Peierls model, and not easy to systematically describe within the current framework. For the specific models considered above, however, we can easily determine the relevant electronic modes. For the Peierls-like models described by the Hamiltonian in Equation 4.14, we can relate each band with a specific combination of site-specific orbitals using the eigenvectors. For $n = 2$, the interband scattering generated by a wavevector Q is described by

$$\begin{aligned} &\left(\frac{1}{\sqrt{2}} c_{k,1}^\dagger + \frac{1}{\sqrt{2}} c_{k,2}^\dagger\right)\left(\frac{1}{\sqrt{2}} c_{k+Q,1} - \frac{1}{\sqrt{2}} c_{k+Q,2}\right) \\ &+ \left(\frac{1}{\sqrt{2}} c_{k,1}^\dagger - \frac{1}{\sqrt{2}} c_{k,2}^\dagger\right)\left(\frac{1}{\sqrt{2}} c_{k+Q,1} + \frac{1}{\sqrt{2}} c_{k+Q,2}\right) \\ &= c_{k,1}^\dagger c_{k+Q,1} - c_{k,2}^\dagger c_{k+Q,2}. \end{aligned} \tag{4.17}$$

For $n=3$ we obtain

$$\begin{aligned}
&\left(\frac{1}{\sqrt{2}}c^\dagger_{k,1}-\frac{1}{\sqrt{2}}c^\dagger_{k,3}\right)\left(\frac{1}{\sqrt{2}}c_{k+Q,1}-\frac{1}{\sqrt{2}}c_{k+Q,3}\right)\\
&+\left(\frac{1}{2}c^\dagger_{k,1}+\frac{1}{\sqrt{2}}c^\dagger_{k,2}+\frac{1}{2}c^\dagger_{k,3}\right)\left(\frac{1}{2}c_{k,1}-\frac{1}{\sqrt{2}}c_{k,2}+\frac{1}{2}c_{k,3}\right)\\
&+\left(\frac{1}{2}c^\dagger_{k,1}-\frac{1}{\sqrt{2}}c^\dagger_{k,2}+\frac{1}{2}c^\dagger_{k,3}\right)\left(\frac{1}{2}c_{k,1}+\frac{1}{\sqrt{2}}c_{k,2}+\frac{1}{2}c_{k,3}\right)\\
=\,&c^\dagger_{k,1}c_{k+Q,1}-c^\dagger_{k,2}c_{k+Q,2}+c^\dagger_{k,3}c_{k+Q,3}.
\end{aligned} \tag{4.18}$$

On the electronic side of things, it is thus immediately clear that for such a system of n coupled Peierls chains, the order parameter will be proportional to

$$\sum_n(-1)^{n+1}\sum_k\langle c^\dagger_{k,n}c_{k+Q,n}\rangle. \tag{4.19}$$

Although the bands are of mixed orbital composition, phonons effectively only couple electronic states within the same chain. As such, all atomic displacements in the periodic lattice distortion will lie along the chain direction.

What we've demonstrated so far is that adding more atoms to a unit cell naturally generates multiple concomitant CDWs, but it does not automatically lead to any physics that goes 'beyond Peierls'. That is, the charge transfers within each chain are each exactly the same as those in the original model. It is no surprise that we have not found anything interesting, because in the multiband models considered above all sites within a unit cell were essentially equal to one another. We will now consider a different minimal model, in which we impose an explicit difference between different types of sites.

Our new minimal model consists of three coupled Peierls chains, but with several key adjustments compared to $n=3$ model discussed above. First, the middle chain is laterally shifted with respect to the outer chains, such that the three chains form (the beginnings of) a triangular lattice. Second, all sites on the outer chains host a single p_x orbital, while the sites on the middle chain host d_{xy} orbitals. This results in a sign difference between horizontal hopping t_1 and interchain hopping t_2. Lastly, we impose that the d-orbital sites have a positive on-site energy $\mu_d=2$, and p-orbital sites have negative on-site energy $\mu_p=-2$. This enforces that charge transfer between the outer and middle chains becomes favourable. The bare tight-binding Bloch Hamiltonian of this new 'diamond-chain' model is given by

$$h_{\mathrm{e}}(k)=\begin{pmatrix}\epsilon_{k,p} & -t_2(1+e^{ika}) & 0\\ -t_2(1+e^{-ika}) & \epsilon_{k,d} & -t_2(1+e^{ika})\\ 0 & -t_2(1+e^{-ika}) & \epsilon_{k,p}\end{pmatrix}, \tag{4.20}$$

where $\epsilon_{k,p}=\mu_p-2t_1\cos(ka)$ and similarly for $\epsilon_{k,d}$, and we used the same basis as before. This gives us a strongly orbitally anisotropic, semimetallic bare band

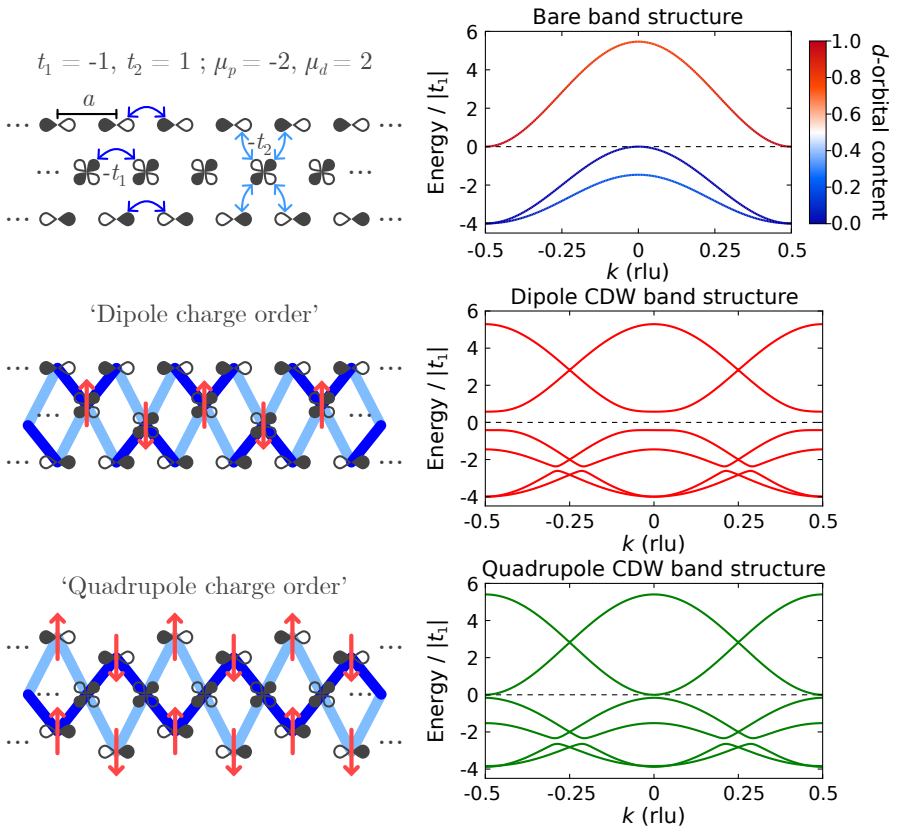

Figure 4.4: A minimal model for beyond-Peierls charge order. The triple-chain has p_x orbitals on the outer chains, and d_{xy} orbitals on the middle chain. We impose an on-site potential of $\mu_p = -2$ on the p-orbital sites, and $\mu_d = 2$ on the d-orbital sites. The hopping parameters are $t_1 = -1$, $t_2 = 1$. As can be seen on the top right, the bare band structure has a state of 100% d-orbital character at $k = \pi/a$, and a p-orbital state at $k = 0$. We can impose different period-2 CDW distortions. Two interesting ones which both open a gap at E_F are shown in the bottom two rows of the figure. On the left, we highlight the primary atomic displacement directions by red arrows, as well as short (bonding, dark blue) and long (anti-bonding, light blue) d-p bonds. As before, 1 rlu = $2\pi/a$.

structure, as shown in the top right panel of Figure 4.4. A single (antibonding) band of p-orbital character touches E_F from below at $k = 0$, while a single band of d-orbital character touches E_F at $k = \pi/a$. Notably, the two k_F lie exactly Q apart, as in all models considered above, and a single period-2 CDW should be able to gap out the entire FS. Considering the nature of the interband scattering, we expect that the main charge displacements in this CDW will relate to the interchain p-d bonds, rather than the intrachain bonds that were relevant in the Peierls-like models. Additionally, due to the antibonding nature of the relevant p-orbital band, we expect the atoms in the upper and lower chains to respond to the CDW by displacing in opposite directions.

Within these expectations, we consider two CDW Ansatzes, that are both found to open a gap at E_{F}. In the first of of these, the primary structural change is that the atoms in the middle chain wiggle up and down, displacing perpendicular to the chain direction (red arrows in Figure 4.4).[10] Interestingly, this implies that there is no net charge displacement between unit cells. Considering the direction of charge transfer between atoms (from light blue to dark blue bonds), we label this first Ansatz as a (transverse) 'dipole CDW'. The second CDW Ansatz we consider is one in which the d-orbital sites remain stationary, while the p-orbital sites wiggle up and down in a π-out-of-phase fashion. Interestingly, the resulting pattern of charge transfers resembles a quadrupole around the d-orbital sites. And as in the dipole CDW case, there is no net displacement of charge between unit cells. The Hamiltonians for the distorted lattices are derived in Appendix A.1.

In these models, we are not making any claims as to what the preferred charge order will be. Of the two Ansatzes considered, the dipole CDW would be more energetically favourable, as it opens a larger gap in the electronic spectrum. Intuitively, these atomic displacements also make more sense, seeing as the d-ortibal states lie at $k = \pi/a$ in the bare band structure, which is suggestive of finding a 'breathing mode' in these atoms rather than in the p-orbital sites. However, it is interesting to note that, in principle, quadrupolar charge displacements are possible, and do open up a gap.

To make the difference with the earlier models more concrete, let us once again consider what states are being scattered between. The orbital composition of the bands is k-dependent, but the relevant states at E_{F} are thankfully very simple. The interband scattering at E_{F} is described by

$$\begin{aligned}&\left(c^{\dagger}_{Q,2}\right)\left(\frac{1}{\sqrt{2}}c_{0,1}-\frac{1}{\sqrt{2}}c_{0,3}\right)\\&=\frac{1}{\sqrt{2}}c^{\dagger}_{Q,2}c_{0,1}-\frac{1}{\sqrt{2}}c^{\dagger}_{Q,2}c_{0,3}.\end{aligned}\tag{4.21}$$

Importantly, this demonstrates that the order parameter for this system is *purely* proportional to charge transfers from the p-orbitals to the d-orbitals. Such inter-chain transfers lie beyond the scope of the Peierls model.

We've now seen examples of two extremes: model systems hosting CDWs that are entirely Peierls-like, and systems that fall entirely outside the scope of the Peierls model. Real materials will generically lie somewhere in between these two extremes. Going from the present minimal models to treating a real material is non-trivial, but this serves as a reminder to be cautious of assuming we fully understand a phenomenon purely based on a single toy model.

As an example of non-trivial charge order in a real system, there is evidence that both dipolar and quadrupolar charge order are realised in the material 1T-

[10] In response to this, the p-orbital sites will also displace along the chain direction. However, this is a secondary effect that we do not directly consider.

$TiSe_2$. Its near-E_F band structure closely resembles that of our diamond-chain model: it has Se p-orbital states at $\mathbf{k} = 0$, and Ti d-orbital states at the edge of the Brillouin zone. Our model thus serves as a 1D approximation of the 3D lattice of $TiSe_2$. Excitingly, a Ginzburg-Landau theory for this material dating from 2011 predicts that in going from high to low temperature, the material first transitions to a transverse dipolar CDW state – in analogy to the one in our minimal model but with three symmetry-related CDW vectors – followed by a second transition to a state with quadrupolar charge displacements on top of the dipolar ones [133]. The quadrupolar phase breaks inversion symmetry, because of which it has commonly been dubbed 'chiral'.[11] The transition to this phase can be understood to arise due to interactions between the three concomitant (dipolar) CDWs [133], an effect that is clearly not captured by our 1D minimal model. While the $T_{CDW} \approx 200\,K$ transition to $(2\times2\times2)$ dipolar charge order has been detected experimentally with many different probes going back to the 1970s (see *e.g.* [136–139]), the existence and chiral nature of the second transition has been a matter of debate in the last decade [135, 140–143]. However, recent experimental results based on the photogalvanic effect [144] and resonant X-ray scattering [145] confirm the existence of this second transition to a state with chiral orbital order in $TiSe_2$.

Of course, one could argue that $TiSe_2$ is something of an outlier. Its semimetallic band structure is qualitatively very different from that of most CDW materials, which are generically metallic at high temperatures with many states crossing the Fermi level. On top of this, the CDW transition in $TiSe_2$ has been shown to be partially driven by the formation and condensation of excitons (bound electron-hole pairs) which are made possible by this same unusual band structure [146, 147]. However, there are plenty of examples of more 'Peierls-like' CDW materials that do not neatly follow what one might naively expect using intuition gained from the Peierls model, as already alluded to at the end of Section 4.1.

Something that appears to have both helped and hindered our collective understanding of charge order is the numerous ways in which discrepances between conventional wisdom and observations in real materials have been explained in the literature. Many attempts have been made to distinguish between distinct mechanisms driving charge order, with often the implicit assumption being made that one or the other mechanism is dominant. A distinction has historically been made between Peierls-inspired 'nesting-driven' CDWs, and those where the charge order arises due to the momentum-structure of the EPC (see *e.g.* [148]). Additionally, there have been proposals that because the conventional FS nesting picture in reciprocal space is demonstrably incomplete, one should consider the real-space shape and overlaps of atomic orbitals, leading

[11] In fact, the Ginzburg-Landau theory in ref. [133] was inspired by the claim of scanning tunnelling microscope (STM) measurements of 'chiral' CDWs in $TiSe_2$ [134]. However, such measurements only probe the surface, and were later dismissed as being inconclusive with regards to the inversion symmetry breaking between subsequent Se-Ti-Se layers within the material; see *e.g.* [135].

to concepts such as 'hidden nesting' [149–152]. This effectively corresponds to including an orbital-dependent EPC. Other mechanisms that have been proposed to drive CDW order include a Jahn-Teller effect, which encourages lattice distortions in certain (usually octahedral) lattice structures [153, 154], the aforementioned exciton condensation [146, 155], and an instability of saddle points in the band structure [156, 157].[12]

In reality, while some of these mechanisms only apply to materials with certain specific features in their (band) structures, it is misleading to distinguish between any of them in an either-or fashion. While other factors may contribute, it is safe to assume that all CDWs are at least partially driven by electron-phonon coupling, as evidenced by the periodic lattice distortions that universally accompany (long-range) charge order. As we are gaining ever more computational power, and our experiments are becoming ever more precise, the time has come to start making more realistic models by improving upon existing frameworks. This is what we'll demonstrate in the following section.

4.3. Quantum field theory

Having gained some intuition from analysing toy models, let us move on to more generally applicable field-theoretical methods with which we can deal with charge order in real materials. We will refer back to the half-filled Peierls model as an example, but the present description in terms of quantum fields will hold for multi-band as well as higher-dimensional systems. This has been demonstrated explicitly for $2H$-$NbSe_2$ [158, 159], $1H$-TaS_2 [160] and $1T$-VSe_2 (Chapters 5 and 6 [2, 3]). This section is based on the more extensive discussions in refs. [127, 161, 162].

In the following introduction, we will consider a system of electrons and phonons which couple to one another.[13] This means we can define a partition function

$$\mathcal{Z} = \int \mathcal{D}[\bar{\psi}, \psi]\mathcal{D}[\bar{\phi}, \phi]e^{-S[\bar{\psi},\psi,\phi]}, \tag{4.22}$$

where the action S is a functional of the electron field ψ_k and phonon displacement field ϕ_q.[14] I will use the general notation that $\mathbf{k}$ is the electron momentum wavevector of the relevant number of space dimensions, while $k = (i\omega_n, \mathbf{k})$. Similarly, for phonons I define the four-momentum $q = (i\Omega_n, \mathbf{q})$. ω_n and Ω_n are Matsubara frequencies, which arise from Wick rotating from real to imaginary time [161]. In the absence of interactions, and assuming normal-ordering of the fields, we can identify the electron creation operator $c^\dagger_{\mathbf{k}}$ with $\bar{\psi}_k$ and the electron annihilation operator $c_{\mathbf{k}}$ with ψ_k. Similarly, we can identify the phonon field $\bar{\phi}_q$ with $(b^\dagger_{\mathbf{q}} + b_{-\mathbf{q}})$, where we note that $\bar{\phi}_q = \phi_{-q}$. In the presence of

[12] References here are the original proposal and an example of a more recent article discussing this mechanism. They are not comprehensive lists of relevant publications.

[13] We neglect Coulomb (electron-photon) interactions here.

[14] We use units in which $\hbar = 1$. The bar in $\bar{\psi}$ indicates complex conjugation.

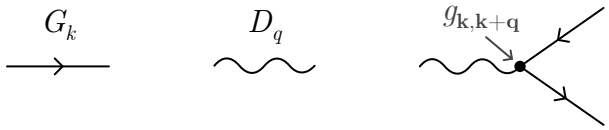

Figure 4.5: The diagrammatic representation of the bare electron propagator G_k and the bare phonon propagator D_q, and how these couple to one another as captured by S_{int}. At the interaction vertex lies the electron-phonon coupling matrix element $g_{\mathbf{k},\mathbf{k+q}}$. Here, we have ommitted the electron band and phonon mode labels.

interactions, the original quasiparticles are no longer well-defined, but their respective fields are. In this notation, the precise form of the action is

$$S = \sum_{k,\nu} \bar{\psi}_{k,\nu} (G_{k,\nu})^{-1} \psi_{k,\nu} + \sum_{q,\eta} \bar{\phi}_{q,\eta} (D_{q,\eta})^{-1} \phi_{q,\eta} + \sum_{k,q,\lambda,\nu,\eta} g^{\lambda,\nu,\eta}_{\mathbf{k},\mathbf{k+q}} \bar{\psi}_{k+q,\nu} \psi_{k,\lambda} \phi_{q,\eta}. \tag{4.23}$$

The above is written in full generality, applying to a system of any dimension and with any number of sites/orbitals per unit cell. ν and λ indicate (bare) electron band indices, and η indicates a bare phonon mode. The bare electron propagator $G_{k,\nu}$ has the standard Schrödinger form [161]:

$$G_{k,\nu} = (i\omega_n - \epsilon^{\nu}_{\mathbf{k}})^{-1}, \tag{4.24}$$

with fermionic Matsubara frequencies $\omega_n = (2n+1)\pi/\beta$ and electron dispersion $\epsilon^{\nu}_{\mathbf{k}}$ in band ν. We have absorbed the chemical potential μ into $\epsilon^{\nu}_{\mathbf{k}}$. The bare phonon propagator is defined as

$$D_{q,\eta} = \frac{-2\Omega^{\eta}_{\mathbf{q}}}{(i\Omega_n)^2 - (\Omega^{\eta}_{\mathbf{q}})^2} \tag{4.25}$$

with bosonic Matsubara frequencies $\Omega_n = 2n\pi/\beta$ and bare phonon frequencies $\Omega^{\eta}_{\mathbf{q}}$ of bare phonon mode η. We represent these propagators diagrammatically as shown in Figure 4.5. The bare electron and phonon fields are coupled to one another in the final term in the action, which allows for an electron to be scattered from state k in band λ to state $k+q$ in band ν by a phonon of type η and momentum q. As introduced at the end of the previous section, $g^{\lambda,\nu,\eta}_{\mathbf{k},\mathbf{k+q}}$ is the generalised form of the EPC matrix element seen in Section 4.1. The attentive reader might have already noted that the action above describes the same physics as the Fröhlich Hamiltonian discussed earlier (Equations 4.5 and 4.16). In the following, we will drop the band and phonon mode indices, under the assumption that all the relevant (combinations of) modes are summed over.

To proceed, we must 'integrate out' one of the two fields. That is, we perform the functional integral over either ψ or ϕ to obtain an effective action in terms of the remaining degrees of freedom. Using perturbation theory, we can derive from this how bare electron or phonon fields become 'renormalised'

due to EPC. This is the quantum field theory-equivalent of the MF treatment applied earlier to obtain Equations 4.6. In the language of quasiparticles, this corresponds to deriving how the free particles become 'dressed' by interactions. We will perform this procedure for phonons in Section 4.3.1. Importantly, this perturbative approach starting from the uncoupled fields only works for describing the renormalisation of fields in the high-temperature normal state. Within the CDW phase, the bare electrons and phonons are no longer a valid starting point to perturb from. In Section 4.3.2 we will discuss the renormalisation of electrons. Here, we include a different method, borrowed from the context of superconductivity, for describing the renormalisation of electrons within the CDW phase, while still using the high-temperature bare electrons as a starting point. We end with some general conclusions regarding the field-theoretical methods introduced, in Section 4.3.3.

4.3.1. Phonon renormalisation

Let us first derive how phonons renormalise, by integrating out the electron fields. To do so, we begin by Taylor expanding the interacting part of the action:

$$\mathcal{Z} = \int \mathcal{D}[\overline{\psi}, \psi]\mathcal{D}[\overline{\phi}, \phi] s^{-S_\psi} e^{-S_\phi} \left(1 - S_{\text{int}} + \frac{1}{2}S_{\text{int}}^2 - \dots\right), \tag{4.26}$$

where S_ψ and S_ϕ are the bare electron and phonon actions, respectively. The first-order contribution of the interaction vanishes, leaving us with the quadratic term:

$$S_{\text{int}}^2 = \sum_{k,k',q,q'} g_{\mathbf{k},\mathbf{k}+\mathbf{q}} g_{\mathbf{k}',\mathbf{k}'+\mathbf{q}'} \overline{\psi}_{k+q} \overline{\psi}_{k'+q'} \psi_{k'} \psi_k \phi_q \phi_{q'}. \tag{4.27}$$

To evaluate what remains of Equation 4.26, we recognise several things. First, the electrons are fermions, which means that their field operators are Grassmann variables, defined by the anticommutation relations

$$\left\{\psi_k, \overline{\psi}_{k'}\right\} = 0 \qquad \text{and} \qquad \left\{\psi_k, \psi_{k'}\right\} = \left\{\overline{\psi}_k, \overline{\psi}_{k'}\right\} = 0. \tag{4.28}$$

Second, we note that the functional (free) average over the electron field of some functional $O[\psi]$ is defined as

$$\langle O[\psi] \rangle = \mathcal{Z}_0^{-1} \int \mathcal{D}[\overline{\psi}, \psi] e^{-S_\psi} O[\psi], \tag{4.29}$$

with the free partition function $\mathcal{Z}_0 = \int \mathcal{D}[\overline{\psi}, \psi] e^{-S_\psi}$. This allows us to perform the functional integral over ψ and rewrite Equation 4.26 as

$$\mathcal{Z} \approx \int \mathcal{D}[\overline{\phi}, \phi] e^{-S_\phi} \left(1 + \frac{1}{2} \sum_{k,k',q,q'} g_{\mathbf{k},\mathbf{k}+\mathbf{q}} g_{\mathbf{k}',\mathbf{k}'+\mathbf{q}'} \langle \overline{\psi}_{k+q} \overline{\psi}_{k'+q'} \psi_{k'} \psi_k \rangle \phi_q \phi_{q'}\right). \tag{4.30}$$

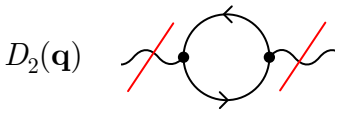

Figure 4.6: The diagrammatic representation of the structured electronic susceptibility $D_2(\mathbf{q})$. We indicate the EPC matrix elements $g_{\mathbf{k},\mathbf{k+q}}$ by dots at the vertices, and the red lines indicate that the phonon legs are amputated. The diagram for the Lindhard function $\chi(\mathbf{q})$ looks the same, but assumes that $g_{\mathbf{k},\mathbf{k+q}} = 1$.

We have redefined the measure of the integral to include a factor $\mathcal{Z}_0$. Next, we apply Wick's theorem, which states that (time-ordered) averages of products of fields can be replaced by the sum of all possible pairwise contractions of those fields [161]. That is, we can rewrite

$$\langle \bar{\psi}_{k+q} \bar{\psi}_{k'+q'} \psi_{k'} \psi_k \rangle = -\langle \bar{\psi}_{k+q} \psi_{k'} \rangle \langle \bar{\psi}_{k'+q'} \psi_k \rangle + \langle \bar{\psi}_{k+q} \psi_k \rangle \langle \bar{\psi}_{k'+q'} \psi_{k'} \rangle. \quad (4.31)$$

We assume that there is no superconducting order, such that there are no Cooper pairs, and $\langle \bar{\psi}_k \bar{\psi}_{k'} \rangle = \langle \psi_k \psi_{k'} \rangle = 0$. The two-point correlator can be derived from the action [161, 162], from which we obtain

$$\langle \psi_k \bar{\psi}_{k'} \rangle = G_k \delta_{k,k'}. \quad (4.32)$$

That is, all pairwise contractions of two (conjugate) field operators with matching indices are equal to the bare electron propagator G_k. If the indices don't match, the contractions are exactly zero. In the first term of Equation 4.31, this enforces that $k' = k + q$ and $q' = -q$, while in the second term it requires that $q = q' = 0$. Noting that $\mathbf{q} = 0$ phonons would correspond to displacements of the entire crystal – something which cannot be included in our theory – the second term in our Wick expansion disappears and we are left with

$$\mathcal{Z} \approx \int \mathcal{D}[\bar{\phi}, \phi] e^{-S_\phi} \left(1 - \frac{1}{2} \sum_{k,q} g_{\mathbf{k},\mathbf{k+q}} g_{\mathbf{k+q},\mathbf{k}} G_{k+q} G_k \phi_q \phi_{-q} \right). \quad (4.33)$$

By Hermiticity of the interaction Hamiltonian, we require that $g_{\mathbf{k+q},\mathbf{k}} = g^*_{\mathbf{k},\mathbf{k+q}}$. In the above, we can identify what we will call the 'structured electronic susceptibility':

$$D_2(\mathbf{q}) = \sum_k |g_{\mathbf{k},\mathbf{k+q}}|^2 G_k G_{k+q}. \quad (4.34)$$

Diagrammatically, this corresponds to a single electron-hole bubble – including the EPC matrix element $g_{\mathbf{k},\mathbf{k+q}}$ at the vertices – with two amputated phonon legs, the latter being what the subscript refers to (see Figure 4.6). This notation is adopted from refs. [158, 163, 164]. The inclusion of the factors $g_{\mathbf{k},\mathbf{k+q}}$ means that the structure of the EPC is included, unlike in the more traditionally defined '(bare) electronic susceptibility' or 'Lindhard function' in which it is assumed that $g = 1$ [161]:

$$\chi(\mathbf{q}) = \sum_k G_k G_{k+q}. \quad (4.35)$$

In the definitions above, the Green's functions may each carry their own band label.

We note that $g^{\lambda,\nu,\eta}_{\mathbf{k},\mathbf{k}+\mathbf{q}}$ may vary upon changing (electron or phonon) momentum, electronic band (relating also to orbital character and electron spin), and the phonon mode under consideration. Forgetting this dependence is convenient because it is hard to compute g directly. As was shown previously in the case of $NbSe_2$ [158, 159] and will be demonstrated in Chapter 5 for VSe_2, neglecting the structure of g is, however, not generically a valid assumption to make. One can approximate (the structure of) g either using *ab initio* methods, as reviewed at length in ref. [165], or using various approximations whose applicability depends on the system being studied. For systems with d-orbital character at the Fermi level, such as the CDW-hosting transition metal dichalcogenides (TMDCs), a known and well-tested approximation is that of Varma *et al.* [159, 166]. Starting with a chosen set of atomic orbitals φ_λ on a lattice, one can construct a tight-binding Hamiltonian H with elements $\langle\varphi_\nu|\, H\, |\varphi_\lambda\rangle$ describing the hopping amplitudes between orbitals, and an orbital overlap matrix S with elements $\langle\varphi_\nu|\varphi_\lambda\rangle$. The latter is included because the chosen set of atomic orbitals need not all be orthogonal. Then, we can solve the Schrödinger equation $H\,|\lambda\rangle = E_\lambda S\,|\lambda\rangle$, where λ labels the band index, for the eigenenergies E_λ and a matrix of eigenvectors which we'll denote by A. Then, the approximation states that the EPC matrix elements can be found using the relation

$$\mathbf{g}^{\lambda,\nu}_{\mathbf{k},\mathbf{k}'} \propto \frac{\partial\epsilon^\lambda_{\mathbf{k}}}{\partial\mathbf{k}}\left[A^\dagger_{\mathbf{k}} S_{\mathbf{k}} A_{\mathbf{k}'}\right]^{\lambda\nu} - \left[A^\dagger_{\mathbf{k}} S_{\mathbf{k}'} A_{\mathbf{k}'}\right]^{\lambda\nu}\frac{\partial\epsilon^\nu_{\mathbf{k}}}{\partial\mathbf{k}'}. \tag{4.36}$$

Importantly, this tight-binding-based approximation removes all phonon mode-dependence (η) from the coupling, making it conveniently easy to solve. In systems where a single band of (roughly) single orbital character makes up the FS, we can also neglect the A and S matrices, and the approximated g reduces to the difference in slope of the band at $\mathbf{k}$ and $\mathbf{k}+\mathbf{q}$. Finally, the expression above is vector-valued. To obtain a scalar, one should project this onto the relevant axis. If the CDW formation involves longitudinal phonons (as is usually the case), one can simply project onto the direction of the phonon wavevector: $g^{\lambda,\nu}_{\mathbf{k},\mathbf{k}+\mathbf{q}} = \mathbf{g}^{\lambda,\nu}_{\mathbf{k},\mathbf{k}+\mathbf{q}}\cdot\mathbf{q}/|\mathbf{q}|$.

In Appendix A.2, we perform the sum over Matsubara frequencies ω_n in the susceptibility expressions to obtain

$$D_2^{\lambda,\nu,\eta}(\mathbf{q}) = \lim_{\Omega\to 0}\left(-\sum_{\mathbf{k}}|g^{\lambda,\nu,\eta}_{\mathbf{k},\mathbf{k}+\mathbf{q}}|^2\frac{f(\epsilon^\lambda_{\mathbf{k}}) - f(\epsilon^\nu_{\mathbf{k}+\mathbf{q}})}{\epsilon^\lambda_{\mathbf{k}} - \epsilon^\nu_{\mathbf{k}+\mathbf{q}} + i\Omega}\right); \tag{4.37}$$

$$\chi^{\lambda,\nu}(\mathbf{q}) = \lim_{\Omega\to 0}\left(-\sum_{\mathbf{k}}\frac{f(\epsilon^\lambda_{\mathbf{k}}) - f(\epsilon^\nu_{\mathbf{k}+\mathbf{q}})}{\epsilon^\lambda_{\mathbf{k}} - \epsilon^\nu_{\mathbf{k}+\mathbf{q}} + i\Omega}\right), \tag{4.38}$$

where we have reintroduced the band and phonon mode labels and $f(\epsilon)$ is the Fermi-Dirac distribution function. Ω, which arises in the derivation from

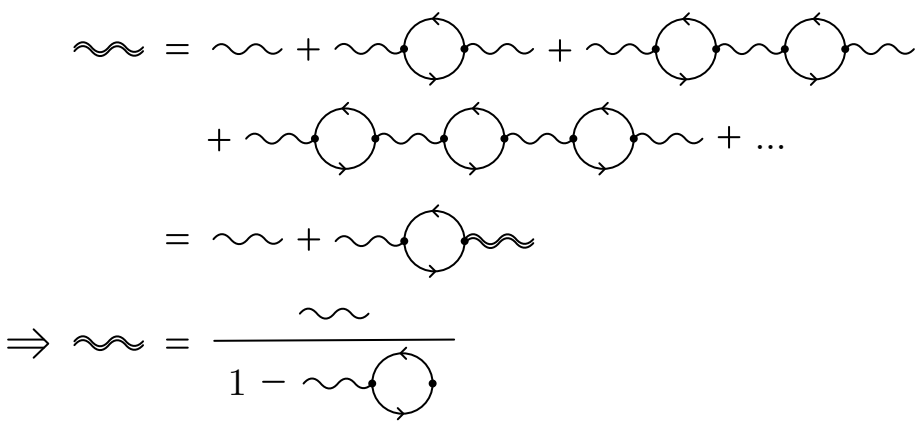

Figure 4.7: In the Random Phase Approximation, we compute the renormalised phonon propagator (indicated by double lines) perturbatively, as an infinite series with an increasing number of uncorrelated electron-hole loops. We can rewrite this series in the form of a self-consistent relation, and then into a form we can solve directly.

the phononic Matsubara frequency, can be understood as the frequency of an externally applied strain used to probe the linear response of the system. While in the present context we are interested in the intrinsic susceptibility of a system towards charge-ordering – without any external fields applied – introducing an infinitesimal factor $i\Omega$ serves to regularise the sum over $\mathbf{k}$. In this case, one should consider only the real part of $D_2(\mathbf{q}, \Omega)$.

Thus far, we have considered the lowest-order-in-g effect of EPC on the bare phonon fields, and found that this is described by the structured electronic susceptibility $D_2(\mathbf{q})$. To extend this to infinite order in g, we can use the 'Random Phase Approximation' (RPA). In this approximation, one considers the renormalisation of the bare phonon propagator by perturbatively expanding it with an infinite series of electron-hole loops. We assume these loops – each equivalent precisely to $D_2(\mathbf{q})$ – to be uncorrelated with one another, hence the name 'random phase'. The renormalised propagator is then given by

$$D_{\mathrm{RPA}} = D + DD_2D + DD_2DD_2D + \dots \tag{4.39}$$

Figure 4.7 shows this expansion diagrammatically. Because the series goes on *ad infinitum*, one can rewrite it in the following way:

$$\begin{aligned} D_{\mathrm{RPA}} &= D + DD_2\left(D + DD_2D + DD_2DD_2D + \dots\right) \\ &= D + DD_2D_{\mathrm{RPA}}. \end{aligned} \tag{4.40}$$

This type of recursion relation is commonly called a *Dyson equation* [161]. We can solve it by subtracting DD_2D_{RPA} from both sides:

$$\begin{aligned} (1 - DD_2)D_{\mathrm{RPA}} &= D \\ D_{\mathrm{RPA}} &= D/(1 - DD_2) = (D^{-1} - D_2)^{-1}. \end{aligned} \tag{4.41}$$

Within the approximations made so far, coupling to electrons has changed the phonon spectrum from the bare one ($\Omega_{\mathbf{q}}$) to a new, renormalised one [159]:

$$\Omega^2_{\mathrm{RPA}} = \Omega^2_{\mathbf{q}} - \Omega_{\mathbf{q}} D_2. \tag{4.42}$$

Notably, because $\Omega_{\mathbf{q}}$ and D_2 are both necessarily positive, $\Omega_{\mathrm{RPA}} \leq \Omega_{\mathbf{q}}$. For every $\mathbf{q}$ where there is a peak in the structured electronic susceptibility, there will be an associated dip in the renormalised phonon spectrum. We thus once again encounter the *Kohn anomaly* [129, 132], mentioned before in Section 4.1. This time, however, we have derived a general expression that is valid for all wavevectors $\mathbf{q}$, and for $T > T_{\mathrm{CDW}}$. The renormalised phonon dispersion in Figure 4.2 was computed using this expression.

At this point, it is useful to consider what could generate a peak in $D_2(\mathbf{q})$. On the one hand, one expects a peak whenever the denominator $\epsilon^{\lambda}_{\mathbf{k}} - \epsilon^{\nu}_{\mathbf{k}+\mathbf{q}} \to 0$. This effect is balanced by the numerator of the expression, $f(\epsilon^{\lambda}_{\mathbf{k}}) - f(\epsilon^{\nu}_{\mathbf{k}+\mathbf{q}})$. A peak in the susceptibility thus requires that the two states connected by $\mathbf{q}$ have a different (statistical) occupation. Considering also the sum over $\mathbf{k}$, we expect maxima in the Lindhard function χ (and therefore also in D_2) at wavevectors $\mathbf{Q}$ which connect a significant portion of states near the Fermi level to other states near E_{F}; this occurs for Fermi surfaces that are nested. Lastly, let us not forget the structured EPC ($g^{\lambda,\nu,\eta}_{\mathbf{k},\mathbf{k}+\mathbf{q}}$); its structure can selectively enhance or diminish peaks in $\chi(\mathbf{q})$. From Equation 4.36 we know that for systems with d-orbital character at E_{F}, coupled states with a large and opposite slope are generically more important than others. This effect has been demonstrated explicitly for *e.g.* $NbSe_2$ [158], TaS_2 [160] and VSe_2 [2] (Chapter 5).

The temperature dependence of $f(\epsilon)$ also gives D_2 a temperature dependence. As a general rule, at higher temperatures any peaks in D_2 are lowered and broadened. This agrees with our intuition that the effect of interactions is diminished at high temperatures. Conversely, any phonon softening in Ω_{RPA} will be enhanced as the temperature is lowered. As already mentioned, one expects a CDW with wavevector $\mathbf{Q}$ to form at the ordering temperature T_{CDW} for which $\Omega_{\mathrm{RPA}}(\mathbf{Q}) \to 0$. When this occurs, it effectively costs zero energy to generate phonons with wavevector $\mathbf{Q}$: what used to be excitations of the lattice become 'frozen' distortions at T_c, resulting in a periodic lattice distortion. For temperatures below T_{CDW}, $\Omega_{\mathrm{RPA}}(\mathbf{Q})$ becomes imaginary (its square being negative), indicating that a new field theory should be used. In other words, the bare electron and phonon propagators used in the original perturbative expansion are no longer a valid starting point inside the CDW phase.

As a demonstration, in Figure 4.8 we compare χ and D_2 of the half-filled Peierls chain for various temperatures, as well as the resulting renormalised phonon spectra Ω_{RPA}. The latter are found using Equation 4.42, with either $g^2_{\mathrm{eff}}\chi$ or D_2 with the structured coupling given by Equation 4.36. The thermal broadening effect is clear, which is in turn reflected in the degree of phonon softening seen in the phonon dispersion. Importantly, however, this figure

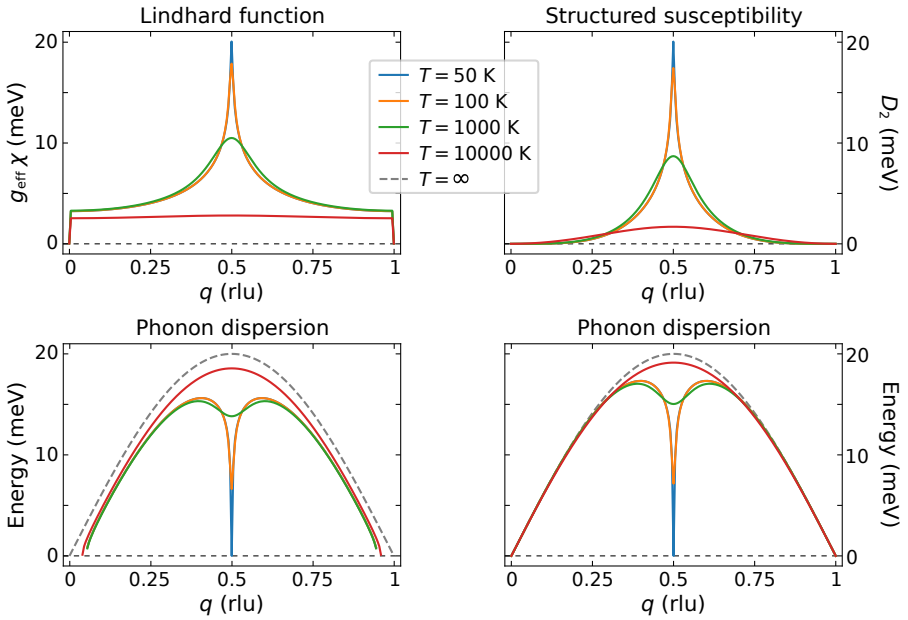

Figure 4.8: The electronic susceptibility, computed as the Lindhard function times an effective EPC squared ($g_{\text{eff}}^2\chi$, left) and the structured electronic susceptibility (D_2, right), and resulting renormalised phonon spectra of a half-filled Peierls chain (lower two plots), for various temperatures. The phonon energy goes to zero at $T_{\text{CDW}} = 50\,\text{K}$, at which point we expect charge order to set in with a CDW wavevector of $Q = \pi/a$. Parameters used: $g_{\text{eff}} \approx 100.3\text{meV}$; structured coupling $g_{k,k+q} = 8.72(v_k - v_{k+q})\,\text{meV}$ with $v_k = d\epsilon_k/dk$; hopping amplitude $t = 0.5\,\text{eV}$; maximum phonon energy $\omega_0 = 20\,\text{meV}$; regulator $\Omega = 10^{-4}\,\text{meV}$. $1\,\text{rlu} = 2\pi/a$.

highlights the weakness of the Lindhard function χ: while both χ and D_2 host a prominent peak at $Q = \pi/a$, χ does not go to zero away from $q = Q$, even at high temperatures. This is problematic, because it means that there is always a range of momenta (around $q = 0$ and $q = 2\pi/a$) where Ω_{RPA} becomes *imaginary*. Imaginary phonon energies imply an instability in the lattice; assuming a constant electron-phonon scattering amplitude g_{eff} thus leads to the prediction that the Peierls chain will always melt! A structured EPC is therefore a necessary ingredient even for this simple toy model.

Before moving on to the treatment of the electrons, let us briefly reflect on what we've done. Integrating out the electrons from the partition function describing coupled electron and phonon fields, we found that effective, lowest-order-in-g effect of the interaction on the phonon fields was renormalisation via the formation of a electron-hole bubbles (D_2). If we consider this the only type of renormalisation allowed, as done in RPA, then we find that D_2 is indeed the relevant quantity needed to describe phonon renormalisation (and CDW formation), all the way up to infinite order in g. Notably, D_2 allows us to (1) predict the wavevector of the CDWs that a system is susceptible to, based on

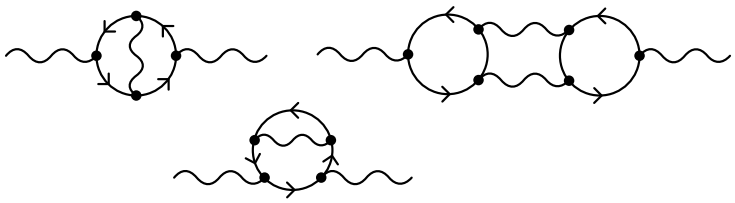

Figure 4.9: The Feynman diagrams constituting the Mode-Mode coupling Approximation (MMA). These are the simplest diagrams accounting for renormalization contributions from the phonon field, which may be considered on top of RPA. From left to right: a vertex correction, a bubble with electron self-energy, and a sixth-order diagram.

its non-interacting electronic spectrum; and (2) predict how phonons soften as a function of temperature. Luckily, both of these predictions can be directly compared to experimental data.

Of course, a full expansion of S_{int} would contain various other types of diagrams at higher order, such as vertex corrections and those with electronic self-energies. These other diagrams may certainly play a role, notably in systems where g is larger or strongly structured. By 'structured', we mean strongly dependent on $\mathbf{k}$, $\mathbf{q}$ or orbital character. In that case, we must move beyond the weak-coupling limit we've considered so far (*i.e.* RPA), and include other types of diagrams in our expansion. This has been done for example for TaS_2 [167], $TiSe_2$ [168] and $NbSe_2$ [158, 159], where the so-called Mode-Mode coupling Approximation (MMA, see Figure 4.9) was employed to capture the effect of phonon fluctuations suppressing the temperature at which long-range CDW order sets in. In many materials, however, there are no (significant) fluctuations, and the weak-coupling RPA description suffices to capture the physics at play.

4.3.2. Electron renormalisation

Just like the phonons, electrons are also renormalised by the electron-phonon interaction. Above T_{CDW}, we can use the same approach as described for phonons in the previous section. Within the RPA, the electronic fields get renormalised as

$$\begin{aligned} G_{\text{RPA}} &= G + G\Sigma G + G\Sigma G\Sigma G + G\Sigma G\Sigma G\Sigma G + \dots \\ &= G + G\Sigma G_{\text{RPA}} \\ \rightarrow \qquad G_{\text{RPA}} &= (G^{-1} - \Sigma)^{-1}. \end{aligned} \tag{4.43}$$

This is yet another Dyson equation. Σ indicates the electronic self-energy. While the self-energy may be composed of a sum over various (higher-order) diagrams [127, 161], we will consider the case with a single phonon line, as depicted in Figure 4.10 or written out in full as:

$$\Sigma_k^{\lambda,\nu,\eta} = \sum_q |g_{\mathbf{k},\mathbf{k}-\mathbf{q}}^{\lambda,\nu,\eta}|^2 G_{k-q}^{\lambda} D_q^{\eta}, \tag{4.44}$$

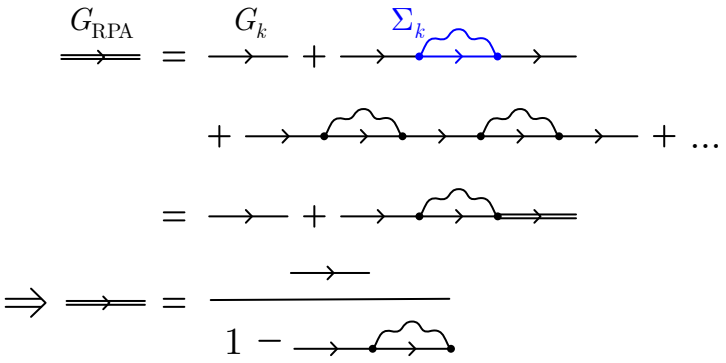

Figure 4.10: In the Random Phase Approximation, we compute the renormalised electron propagator (G_{RPA}, indicated by double lines) perturbatively, as an infinite series with an increasing number of uncorrelated electronic self-energy interactions (Σ_k, highlighted in blue). As done earlier for phonons, we can rewrite this series in the form of a self-consistent relation, and then into a form we can solve directly.

where ν indicates the electron mode of the two external (amputated) electron legs, λ the electron mode of the scattered electron, and η the phonon mode coupled to. This can be understood as renormalisation by generating and reabsorbing a (virtual) phonon. We perform the Matsubara summation in Equation 4.44 in Appendix A.3.

Here we considered only a simple form of coupling between electrons and phonons. Incorporating higher-order diagrams, or instead considering also electron-photon (*i.e.* Coulomb) interactions would result in a different kind of electronic self-energy. This will complicate the mathematics, but won't change the qualitative outcome: including interactions, electron propagators are renormalised as

$$G_\Sigma(\mathbf{k}, i\omega_n) = (i\omega_n - \epsilon_{\mathbf{k}} - \Sigma_k)^{-1}, \tag{4.45}$$

where we've absorbed the chemical potential into $\epsilon_{\mathbf{k}}$, and the self-energy $\Sigma_k = \Sigma'_k + i\Sigma''_k$ is some complex-valued function of k.[15]

To see the effect that such a self-energy has on the electrons, let us first re-express the electron propagator in what's known as the *Lehmann representation*:

$$G_\Sigma(\mathbf{k}, i\omega_n) = -\frac{1}{\pi}\int_{-\infty}^{\infty} d\epsilon \, \frac{\mathrm{Im}\left[G_\Sigma(\mathbf{k}, \epsilon)\right]}{i\omega_n - \epsilon}. \tag{4.46}$$

[15] In Fermi liquid theory – which is a good approximate description for many weakly correlated electron systems – we note that the imaginary part of the self-energy must go to zero at the Fermi level, at zero temperature: $\Sigma''(\mathbf{k}, \epsilon) \to 0$ as $k \to k_{\mathrm{F}}$ and $\epsilon \to 0$ [127]. This means that quasi-electrons at the Fermi energy are infinitely long-lived, well-defined particles. From this it also follows that we can expand Σ'' as a power series in energy ($\sim \epsilon^2 + \dots$) and that the self-energy must be a smooth function for energies close to the Fermi level.

The above (general) identity follows from the Kramers Kronig relation. Within this representation, we identify what's known as the 'spectral function'

$$A(\mathbf{k}, \epsilon + i\delta) = -\frac{1}{\pi}\mathrm{Im}\left[G_\Sigma(\mathbf{k}, \epsilon + i\delta)\right], \tag{4.47}$$

where we've introduced an infinitessimal imaginary part $i\delta$.[16] The spectral function can be understood as a probability measure for finding a (quasi)electron with energy ϵ at momentum $\mathbf{k}$ [161]. If $\Sigma_k = 0$, the spectral function is given by

$$A(\mathbf{k}, \epsilon + i\delta) = -\frac{1}{\pi}\frac{\delta}{\left(\epsilon - \epsilon_{\mathbf{k}}\right)^2 + \delta^2}. \tag{4.48}$$

In the limit $\delta \to 0^+$, this reduces to the delta function $\delta(\epsilon - \epsilon_{\mathbf{k}})$ [162]. That is, in the absence of electron-electron interactions, the spectral function returns a series of delta functions at the positions of the bare, single-particle electron dispersion (including chemical potential) $\epsilon_{\mathbf{k}}$. If instead $\Sigma_k \neq 0$, we obtain the Lorentzian form

$$A(\mathbf{k}, \epsilon + i\delta) = -\frac{1}{\pi}\frac{\delta - \Sigma_k''}{\left(\epsilon - \epsilon_{\mathbf{k}} - \Sigma_k'\right)^2 + \left(\delta - \Sigma_k''\right)^2}. \tag{4.49}$$

From this expression it is immediately clear that the real part Σ_k' of the self-energy shifts the energies at which quasi-electrons are most likely to be found, while the imaginary part Σ_k'' broadens the spectral function from a delta function (in the limit $\delta \to 0$) to a Lorentzian of finite width. This is a general feature, independent of what interactions induce an electronic self-energy. Figure 4.11 demonstrates the broadening effect in the spectral function of the Peierls model, assuming a constant imaginary self-energy.

The spectral function is interesting from an experimental standpoint, because it can be (more or less) directly probed using Angle-Resolved Photoemission Spectroscopy (ARPES).[17] Here, we will briefly recap the most relevant features of this experimental technique; for a more complete introduction, we refer the reader to refs. [169, 170], on which the present summary is based. In this technique, photoemitted electrons from a material are collected in an energy and angle-resolved manner. In this process, the conserved in-plane crystal momentum $\mathbf{k}_\parallel$ can be determined from the angle at which the electrons exit the material. The out-of-plane component of the crystal momentum may be probed by varying the photon energy ν. The photoelectron intensity one measures may be described by

$$I_{\mathrm{ARPES}}(\mathbf{k}, \epsilon) = I_0(\mathbf{k}, \nu, \mathbf{A}) f(\epsilon) A(\mathbf{k}, \epsilon), \tag{4.50}$$

[16] We have performed the Wick rotation $i\omega_n \to \epsilon + i\delta$.

[17] There are other techniques that probe the spectral function, but we focus on ARPES here because it is the most commonly used $\mathbf{k}$-resolved probe, and will feature in Chapters 5 and 6.

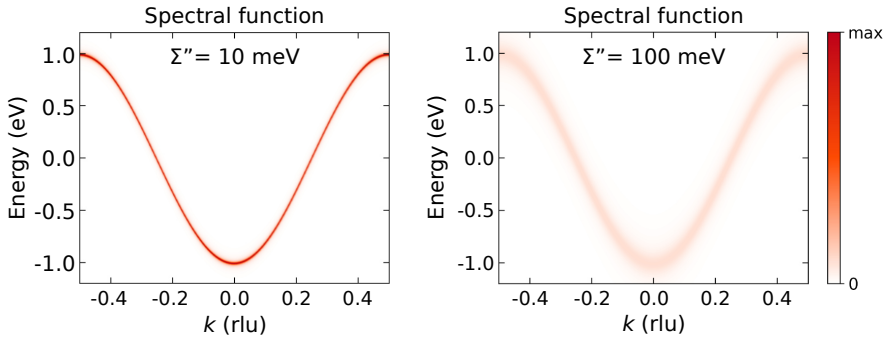

Figure 4.11: The spectral function $A(\mathbf{k}, \epsilon)$ of the half-filled Peierls chain, assuming that the electronic self-energy Σ_k is some imaginary constant $i\Sigma''$. The larger Σ'', the more peaks in the spectral function are broadened. Plot parameters: hopping amplitude $t = 0.5\,\mathrm{eV}$, chemical potential $\mu = 0$. $1\,\mathrm{rlu} = 2\pi/a$.

where $I_0(\mathbf{k}, \nu, \mathbf{A})$ is proportional to the squared one-electron dipole matrix element $|M_{f,i}^{\mathbf{k}}|^2$, which in turn depends on the electron momentum and on the energy and polarisation of the incoming photon; $\mathbf{A}$ is the electromagnetic vector potential. The Fermi-Dirac distribution function $f(\epsilon)$ enters because only occupied electronic states can be probed. In the relation above, we neglect the presence of any extrinsic background, which should be subtracted from the measured spectrum, as well as the effects of the energy and momentum resolution of the equipment used, which typically results in a Gaussian-like broadening effect.

Experimentally probing the spectral function is useful in two ways. On the one hand, in non- or weakly interacting systems, $A(\mathbf{k}, \epsilon)$ approximates the electronic band structure, such that ARPES spectra can be directly compared to tight-binding or *ab initio* calculations. Conversely, a significant discrepancy between band structure calculation predictions and an ARPES spectrum, or the measurement of a linewidth in an ARPES spectrum that is broader than the experimental resolution of the equipment used, are both direct indicators of interactions.

Importantly, the electron renormalisation described so far – via the electron self-energy – will *not* result in a gap opening in the spectrum as a result of charge order[18] as described earlier in this chapter. This means that the description thus far only holds for temperatures above T_{CDW}. Once a material has transitioned to a CDW state, the original, hypothetical bare electron and phonon propagators used as a starting point for our perturbative approach have different symmetries than the quasi-electrons and quasi-phonons you expect to find. Notably, translational symmetry has broken down in such a way that, in the normal state basis, states with momentum $\mathbf{k}$ are now equivalent to states

[18] Or any other symmetry-breaking order in the system.

at any momentum $\mathbf{k}+n\mathbf{Q}$, where $n \in \mathbb{Z}$ and $\mathbf{Q}$ the wavevector of the CDW.[19]

The resolution of this problem is to define a new set of bare electron and phonon propagators, with the symmetries present in the ordered state. A rather ingenious approach to doing this – at least for the electrons – is to use the same bare propagators as before, but to impart the breaking of translational symmetry by defining a matrix-valued bare electron propagator with copies of the original bare propagators, each lying at momenta shifted by all multiples of $\mathbf{Q}$ that still lie (at distinct positions) within the original Brillouin zone. We require that $\mathbf{Q}$ is commensurate with the lattice; *i.e.* we require that $N\mathbf{Q}$ equals a reciprocal lattice vector, with $N \in \mathbb{Z}$. If there are multiple concomitant CDW wavevectors $\mathbf{Q}_j$, we consider all linear combinations $\sum_j n_j \mathbf{Q}_j$ that shift $\mathbf{k}$ to a different position within the original Brillouin zone (with $n_j \in \mathbb{Z}$). For the period-2 CDW mode in the Peierls chain, $N = 2$ and we can define a new bare electron propagator as:

$$\hat{G}_k = \begin{pmatrix} G_k & 0 \\ 0 & G_{k+Q} \end{pmatrix}. \tag{4.51}$$

That this is an $N \times N$ matrix reflects the fact that there will be N renormalised electron 'bands' in the CDW state.[20] In the bare propagator defined above, these different bands do not interact with one another at all; this can be seen from the fact that the matrix is diagonal.

Now that we have a new bare propagator, we are ready to determine how EPC may allow these different bands to interact and open up a gap. To do this, we should note that inter-band interactions require that the renormalised electron propagator has off-diagonal elements. The question then is: what should we put there? It should be something *like* an electron propagator, but one for which the electron momentum is both k and $k + Q$ at the same time. Here, we can use a method developed in the context of superconductivity by Nambu [171] and Gor'kov [172].[21] The superconducting state is characterised by the formation of Cooper pairs, which breaks the conservation of particle number. That is, the expectation value of $F^\dagger = \langle \psi^\dagger_{k,\uparrow} \psi^\dagger_{-k,\downarrow} \rangle \neq 0$, and likewise for $F = \langle \psi_{-k,\downarrow} \psi_{k,\uparrow} \rangle$; these define new 'anomalous' propagators that create and annihilate one Cooper pair, respectively [162]. Similarly, the breaking of momentum conservation in the presence of charge order means that $\langle \psi_k \psi^\dagger_{k+Q} \rangle \neq 0$.

[19] In crystals of dimension higher than one, it is common that there is more than one plane-wave CDW mode, with the different modes related via a crystal symmetry (*e.g.* rotation). In this case, $\mathbf{Q}$ should be replaced with any linear combination (with integer prefactors) of the wavevectors of the CDWs that are present.

[20] Electron bands are really only defined for purely non-interacting electrons, where $A(\mathbf{k}, \epsilon)$ is composed of a set of delta functions lying along $\epsilon_{\mathbf{k}}$. The 'bands' that we mean here are the interaction-broadened peaks in $A(\mathbf{k}, \epsilon)$ that will lie at roughly the same positions as long as the interactions are not too strong.

[21] The work of Nambu and Gor'kov was built on foundations laid by Bogoliubov [173], and popularised in the West by de Gennes [174]. It is commonly called the 'Bogoliubov-de Gennes method' [175]. We adopt the notation used in ref. [162].

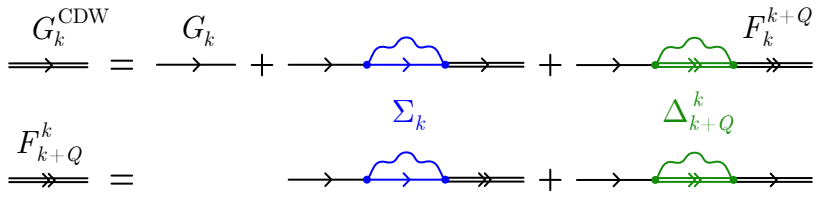

Figure 4.12: In the Random Phase Approximation, we compute the renormalised electron propagator (G_k^{CDW}, indicated by double lines) and the momentum-non-conserving anomalous propagator (F_{k+Q}^{k}, indicated by double lines and double arrows) perturbatively. There are two types of interactions included: electronic self-energy interactions (Σ_k, highlighted in blue); and new interactions that include a momentum shift of one CDW wavevector (Δ_{k+Q}^{k}, highlighted in green). We can rewrite these series as a set of self-consistent relations.

4

This allows us to define anomalous propagators that change momentum by one CDW wavevector Q:

$$F_{k+Q}^{k} = \langle \psi_k \psi_{k+Q}^{\dagger} \rangle. \tag{4.52}$$

This anomalous propagator starts with momentum k and ends with momentum $k+Q$. We note that $F_k^{k+Q} = (F_{k+Q}^{k})^*$. As before, in the presence of multiple CDW wavevectors, the upper and lower indices of F would correspond to any integer linear combination $k_1 = k + \sum_j n_j Q_j$ and $k_2 = k + \sum_j m_j Q_j$, where the sums include any combinations that still reside within the first Brillouin zone and $k_1 - k_2$ is one CDW wavevector. In the case of the half-filled Peierls chain the notation is conveniently simple, and we denote the renormalised electron propagator in matrix form as:

$$\hat{G}^{\mathrm{CDW}} = \begin{pmatrix} G_k^{\mathrm{CDW}} & F_{k+Q}^{k} \\ F_k^{k+Q} & G_{k+Q}^{\mathrm{CDW}} \end{pmatrix}, \tag{4.53}$$

with renormalised electron propagators G_k^{CDW}.

The last ingredient we need is an interaction matrix. We will assume for now that the electron fields only interact with bare phonon fields described by propagator D_q. Much like before, we can derive the form of the renormalised propagator perturbatively. Within RPA, we find a set of self-consistent relations for the propagators in $\hat{G}^{\mathrm{CDW}}$, shown diagrammatically in Figure 4.12. We can write this concisely in a matrix form of the Dyson equation:

$$\hat{G}^{\mathrm{CDW}} = \hat{G} + \hat{G}\hat{\Sigma}\hat{G}^{\mathrm{CDW}}. \tag{4.54}$$

The interaction matrix $\hat{\Sigma}$ consists of two types of interaction processes. On the diagonal, there are the self-energies as described by Equation 4.44, while away from the diagonal there are interaction terms of the form

$$\Delta_{k+Q}^{k} = \sum_q g_{\mathbf{k},\mathbf{k}-\mathbf{q}} g_{\mathbf{k}-\mathbf{q}+\mathbf{Q},\mathbf{k}+\mathbf{Q}} F_{k-q+Q}^{k-q} D_q. \tag{4.55}$$

These terms thus describe an electron-phonon interaction between two electron fields with momenta $\mathbf{k}$ and $\mathbf{k}+\mathbf{Q}$, lying exactly one CDW wavevector apart,

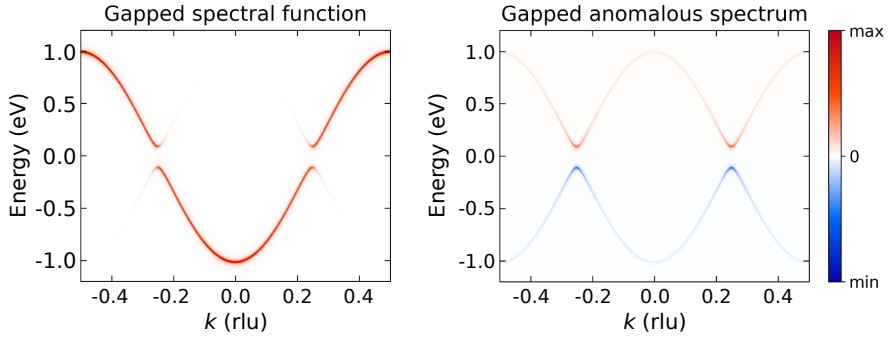

Figure 4.13: The spectral function $A(\mathbf{k}, \epsilon) \propto \mathrm{Im}[G_k^{\mathrm{CDW}}]$ (left) and anomalous spectrum $\mathrm{Im}[F_{k+q}^{q}]$ (right) of the half-filled Peierls chain in the CDW phase, assuming a electronic self-energy $\Sigma_k = 10i\,\mathrm{meV}$ and a constant gap $\Delta = 100\,\mathrm{meV}$, and using Equation 4.57. The two plots use the same (symmetric) colour scale. Plot parameters: $t = 0.5\,\mathrm{eV}$; $\mu = 0$. $1\,\mathrm{rlu} = 2\pi/a$.

via the generation and reabsorption of a (virtual) anomalous propagator and phonon. In the case of the Peierls model, the interaction matrix is given by

$$\hat{\Sigma} = \begin{pmatrix} \Sigma_k & \Delta_{k+Q}^{k} \\ \Delta_k^{k+Q} & \Sigma_{k+Q} \end{pmatrix}. \tag{4.56}$$

As was the case for the anomalous propagators, $\Delta_k^{k+Q} = (\Delta_{k+Q}^{k})^*$, such that $\hat{\Sigma}$ is Hermitian.

Now that we have a self-consistent matrix equation, let us address how to solve it. We can rearrange the matrix Dyson equation as follows:

$$\begin{aligned} \hat{G}^{\mathrm{CDW}} &= \hat{G} + \hat{G}\hat{\Sigma}\hat{G}^{\mathrm{CDW}} \\ (\hat{1} - \hat{G}\hat{\Sigma})\hat{G}^{\mathrm{CDW}} &= \hat{G} \\ \hat{G}^{\mathrm{CDW}} &= (\hat{1} - \hat{G}\hat{\Sigma})^{-1}\hat{G}. \end{aligned} \tag{4.57}$$

Depending on the dimensions of the matrices involved, performing the required matrix inversion may be computationally expensive. In the case of the half-filled Peierls chain, however, the last line of the above can easily be rewritten as

$$\hat{G}^{\mathrm{CDW}} = \frac{1}{\det(\hat{1} - \hat{G}\hat{\Sigma})} \begin{pmatrix} G_k - G_{k+Q}\Sigma_{k+Q}G_k & G_k\Delta_{k+Q}^{k}G_{k+Q} \\ G_{k+Q}\Delta_k^{k+Q}G_k & G_{k+Q} - G_k\Sigma_k G_{k+Q} \end{pmatrix}. \tag{4.58}$$

The above demonstrates the interaction between the bare electron propagators at k and $k{+}Q$, as expected in the CDW phase. It is also immediatedly clear that the anomalous spectral functions are directly proportional to the gap function: $F_{k+Q}^{k} \propto \Delta_{k+Q}^{k}$. The anomalous propagators are thus necessarily zero when the CDW gap disappears.

Now that we have an expression for $\hat{G}^{\mathrm{CDW}}$, how can we use it? The top left element of the matrix is the renormalised equivalent of the bare electron propagator G_k; this is the propagator that enters the spectral function, directly probed by ARPES. Figure 4.13 demonstrates what the spectral function $A(\mathbf{k},\epsilon) = (-1/\pi)\mathrm{Im}\left[G_k^{\mathrm{CDW}}\right]$ and the spectral function of the anomalous propagator F_{k+q}^{k} look like for the Peierls model, assuming a constant self-energy and gap function. Although these are not realistic parameters, they are instructive. First, the gapped spectral function primarily maintains intensity around the bare electron dispersion. This contrasts with the naïve tight-binding CDW band structures that we showed in Sections 4.1 and 4.2; while the bare dispersions get folded back into the smaller Brillouin zone, the back-folded bands generically get less intensity in the renormalised spectral function [129].

Second, we imposed a constant gap, and a gap naturally opened at positions in the spectrum lying exactly momentum $\mathbf{Q}$ apart. Of course, this is by construction, because our calculation imposes that momentum is only not conserved up to one CDW wavevector, so that interactions are only allowed between states that are separated by this wavevector. While it may seem simple, this makes such a calculation a powerful tool for predicting where (partial) gaps may open in the spectrum of real materials, given the wavevector(s) of the charge order that forms. We include the word 'may' here, because the structure of the EPC may partially suppress gaps in some regions and some bands. It cannot, however, open gaps at positions other than those predicted by the simple gap prediction described here. We use this technique in Chapter 5 for the material VSe_2, whose three-dimensional, poorly nested FS makes such a prediction useful.

Finally, any Dyson equation, including Equation 4.57, can in principle be solved self-consistently. That means that we can solve for all elements of Equation 4.56 to find the self-consistent values for Σ_k and the CDW gap Δ_{k+Q}^{k}. Let us demonstrate this procedure with the Peierls model. We start with a seed self-energy matrix with the elements a chosen set of (possibly complex-valued) functions:

$$\hat{\Sigma}^{(0)} = \begin{pmatrix} \Sigma_k^{(0)} & (\Delta_{k+Q}^{k})^{(0)} \\ (\Delta_k^{k+Q})^{(0)} & \Sigma_{k+Q}^{(0)} \end{pmatrix}. \tag{4.59}$$

Note that there are only two distinct input functions: $\Sigma_k^{(0)} = \Sigma^{(0)}(\mathbf{k}, \epsilon + i\delta)$, which prescribes $\Sigma_{k+Q}^{(0)}$; and $(\Delta_{k+Q}^{k})^{(0)} = \Delta^{(0)}(\mathbf{k}, \epsilon + i\delta)$, which is the complex conjugate of $(\Delta_k^{k+Q})^{(0)}$.[22] Using Equation 4.58 we then find the '0-loop' expression for $\hat{G}^{\mathrm{CDW}}$, given by

$$(\hat{G}^{\mathrm{CDW}})^{(0)} = \begin{pmatrix} G^{(0)}(\mathbf{k},\epsilon) & F^{(0)}(\mathbf{k},\epsilon) \\ (F^{(0)}(\mathbf{k},\epsilon))^{*} & G^{(0)}(\mathbf{k}+\mathbf{Q},\epsilon) \end{pmatrix}. \tag{4.60}$$

[22] We use bold font for the one-dimensional momentum $\mathbf{k}$ to distinguish it from the $(d+1)$-momentum $k = (i\omega_n, \mathbf{k})$.

This we can then plug into the '1-loop' expressions derived in Appendix A.3:

$$\Sigma^{(1)}(\mathbf{k},\epsilon+i\delta) = -\frac{1}{\pi}\sum_{\mathbf{q}}\Bigg(|g_{\mathbf{k},\mathbf{k}-\mathbf{q}}|^2\int d\epsilon'\,\mathrm{Im}\left[G^{(0)}(\mathbf{k}-\mathbf{q},\epsilon')\right] \times\left(\frac{n_{\mathrm{B}}(\Omega_{\mathbf{q}})-f(\epsilon')+1}{\epsilon-\epsilon'-\Omega_{\mathbf{q}}+i\delta}+\frac{n_{\mathrm{B}}(\Omega_{\mathbf{q}})+f(\epsilon')}{\epsilon-\epsilon'+\Omega_{\mathbf{q}}+i\delta}\right)\Bigg); \tag{4.61}$$

$$\Delta^{(1)}(\mathbf{k},\epsilon+i\delta) = -\frac{1}{\pi}\sum_{\mathbf{q}}\Bigg(g_{\mathbf{k},\mathbf{k}-\mathbf{q}}g_{\mathbf{k}-\mathbf{q}+\mathbf{Q},\mathbf{k}+\mathbf{Q}} \times\int d\epsilon'\,\mathrm{Im}\left[F^{(0)}(\mathbf{k}-\mathbf{q},\epsilon')\right] \times\left(\frac{n_{\mathrm{B}}(\Omega_{\mathbf{q}})-f(\epsilon')+1}{\epsilon-\epsilon'-\Omega_{\mathbf{q}}+i\delta}+\frac{n_{\mathrm{B}}(\Omega_{\mathbf{q}})+f(\epsilon')}{\epsilon-\epsilon'+\Omega_{\mathbf{q}}+i\delta}\right)\Bigg). \tag{4.62}$$

The outcomes of these relations can then be used as input for $\hat{\Sigma}^{(1)}$, to compute $(\hat{G}^{\mathrm{CDW}})^{(1)}$. Going on to find $\hat{\Sigma}^{(2)}$ and iterating further is very computationally expensive. A much faster way to find the self-consistent solution is to plot the outcomes $\Sigma^{(1)}$ and $\Delta^{(1)}$ against the seed input values; the intercepts $\Sigma^{(0)}=\Sigma^{(1)}$ and $\Delta^{(0)}=\Delta^{(1)}$ then constitute the self-consistent outcome. If Σ_k and Δ^k_{k+Q} are both non-zero, their self-consistent values should be found simultaneously.

Such a method can also be applied to real materials, as was done for finding the self-consistent, momentum-dependent gap function in $NbSe_2$ [159, 162]. In practice, some approximations must be made for such a calculation to be feasible. In the case of $NbSe_2$, the band structure was approximated to be two-dimensional, Σ_k was set to zero, the gap was assumed to be real and independent of energy (assuming the value at $\epsilon=0$), and the gap function was found self-consistently at several high-symmetry points in the Brillouin zone and then fit to a tight-binding expression with the symmetries of the (2D) lattice. Despite these approximations, the predicted self-consistent gap function opened partial gaps at the correct locations of the FS, reproducting what is measured by ARPES, and was able to reproduce the suppression of density of states around E_{F}, as measured by STM experiments [159, 162]. This definitively resolved the preceding confusion and discussion in the literature surrounding the partial CDW gap in $NbSe_2$ which only opens in one of the two bands making up the FS [157, 176–178]; something which can *only* be understood with the consideration of a structured EPC.

4.3.3. Conclusion

This concludes our introduction to field-theoretical methods for describing charge order. We have seen how to describe the renormalisation of electrons and phonons in the normal state ($T>T_{\mathrm{CDW}}$) of a CDW material using the

Random Phase Approximation. This gives us the structured electronic susceptibility $D_2(\mathbf{q})$, which we can use to predict at what wavevector phonons will soften, and thereby the wavevector(s) with which we expect CDWs to form. Additionally, we can make predictions regarding how the electronic spectrum is renormalised by interactions, and where gaps will open in the electronic spectrum inside the CDW phase ($T < T_{\mathrm{CDW}}$), and compare these predictions with the spectral function as experimentally probed by ARPES.

Aside from generating more complete predictions than the much-simplified Peierls MF theory (Section 4.1) and the toy models discussed in Section 4.2, the present framework highlights the importance of considering not only the shape of the Fermi surface but also a structured electron-phonon coupling. The latter, which may depend on the slope and orbital character of the bands, is needed for a complete understanding of charge order in real materials. The need for including it has in fact long been argued for in the literature [129, 158–160, 164, 179, 180]. Hopefully, modern computational power will allow for it to become the standard.

In the following chapters, we will apply the methods discussed here to the real material VSe_2. In Chapter 5, we show that the bulk material hosts three-dimensional CDWs whose properties can only be understood when the structured EPC is considered. In Chapter 6 we turn to monolayer VSe_2. In a combined experimental and theoretical study, we demonstrate that the two-dimensional material hosts two distinct CDWs. One of these is a modified version of the bulk charge order, while the other is cannot be described by EPC alone, being largely driven by Coulomb interactions. The latter constitutes, to the best of our knowledge, the first example of a Coulomb-driven CDW in a real material.[23] In both cases, the charge order goes decidedly beyond the simplified picture of the Peierls model.

[23] We don't consider Mott insulators as constituting a CDW phase, because they are usually associated with antiferromagnetic order and highly localised electrons.

5

Charge order from structured coupling in VSe_2

Charge order – ubiquitous among correlated materials – is customarily described purely as an instability of the electronic structure. However, the resulting theoretical predictions often do not match high-resolution experimental data. A pertinent case is $1T$-VSe_2, whose single-band Fermi surface and weak-coupling nature make it qualitatively similar to the Peierls model underlying the traditional approach. Despite this, its Fermi surface is poorly nested, the thermal evolution of its charge density wave (CDW) ordering vectors displays an unexpected jump, and the CDW gap itself evades detection in direct probes of the electronic structure. We demonstrate that the thermal variation of the CDW vectors is naturally reproduced by the electronic susceptibility when incorporating a structured, momentum-dependent electron-phonon coupling, while the evasive CDW gap presents itself as a localized suppression of spectral weight centered above the Fermi level. Our results showcase the general utility of incorporating a structured coupling in the description of charge ordered materials, including those that appear unconventional. This chapter is based on ref. [2].

In the previous chapter, we introduced a theoretical framework for describing charge order, based on quantum field theory. In line with what has long been argued for in the literature, this framework allows for taking into account the structured, momentum-dependent electron-phonon coupling (EPC) to supplement the traditional analysis based solely on nesting of the electronic structure and yields *quantitative* agreement with experimental observations [129, 158, 159, 164, 179, 180]. Going beyond the strongly-coupled settings considered before, we show here that including a structured EPC resolves several paradoxes surrounding the CDW phase in the weakly-coupled compound $1T$-VSe_2.

Let us begin by summarising what is known about the CDWs in this compound. The CDW gap in VSe_2 was found in recent scanning tunnelling spec-

troscopy (STS) measurements to be $2\Delta = 24 \pm 6\,\text{meV}$ at a temperature of 5 K [124], while the CDW ordering temperature is approximately $T_{\text{CDW}} \approx 110\,\text{K}$ [122, 181–183]. This is close to the BCS ratio of $2\Delta(T=0) = 3.52\,k_{\text{B}}T_{\text{CDW}}$ [129], which together with the lack of evidence for charge-order fluctuations above T_{CDW} places VSe_2 firmly within the weak-coupling regime [124]. Electronically, a single band of predominantly single-orbital character makes up the Fermi surface (FS), consistent with a model Peierls description. Despite this apparent best-case scenario for a weak-coupling CDW, several experimental observations appear to be paradoxical and inconsistent with the customary interpretation of 'nesting-driven' charge order.

Angle-resolved photoemission spectroscopy (ARPES) studies, for example, do not show clear gaps in the spectral function at low temperatures, such that the CDW gap structure remains unclear [184–188]. This is in stark contrast to other transition metal dichalcogenides (TMDCs) with CDW instabilities, such as $2H$-$NbSe_2$, $2H$-$TaSe_2$ and $1T$-TaS_2 [177, 189]. Furthermore, while the in-plane components of the three simultaneous CDW wavevectors $\mathbf{Q}_i$ $(i = 1, 2, 3)$ in VSe_2 are commensurate (periodicity $4a$ with lattice parameter a), it was determined via X-ray diffraction that their common out-of-plane component is incommensurate and varies from $q_z = 0.314\,c^*$ at 105 K to $q_z = 0.307\,c^*$ below 85 K with c^* the reciprocal lattice vector along k_z [181].

The thermal evolution of the ordering wavevector was deemed anomalous, and led to the suggestion that this material hosts two distinct CDW phases [181, 190]. This is unusual, since both phases remain incommensurate, and the transition between them is therefore not of the common lock-in type.[1] Phase contrast in satellite dark field images led to the suggestion that the transition may be between a high-T, three-component CDW and a low-T phase with only two of the three symmetry-related $\mathbf{Q}_i$, a so-called 2Q phase [190]. Although theoretically allowed, such a 2Q phase would be unusual, as it can only be stable in a small region of phase space and requires fine-tuned contributions from sixth order terms in a Landau expansion of the free energy [159, 190]. Various scanning tunnelling microscopy (STM) experiments (down to 4.2 K) report a 3Q CDW phase [122, 124, 191, 192], while others observe an enhanced intensity of one or two CDW wavevectors [193, 194]. The latter could be the effect of an anisotropic STM tip [124] and/or spatial variations in the relative phases of the three CDW components [192]. Concrete evidence for a phase transition around 85 K is also absent in thermodynamic probes [122, 182, 183].

[1] To 'lock in' means that an incommensurate CDW becomes commensurate with the lattice, thereby moving away from the preferred ordering wavevector as determined by the electronic susceptibility.

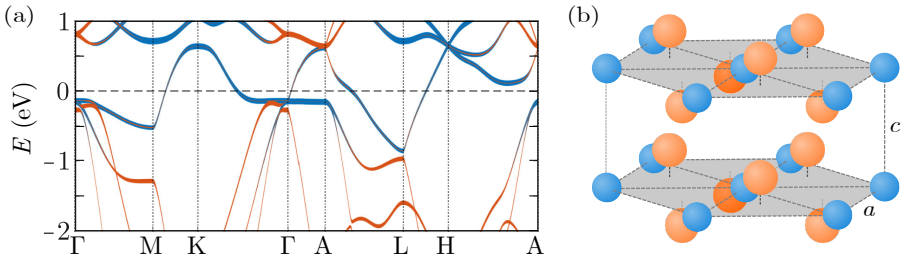

Figure 5.1: (a) The *ab initio* band structure of VSe_2 with the orbital character of the bands indicated. Orange corresponds to Se character, and blue indicates V character. The single band crossing the Fermi level was used to compute the electronic susceptibility. (b) Sketch of the layered atomic structure of 1*T*-VSe_2, in which layers of vanadium atoms (blue) are sandwiched between two layers of selenium (orange).

5.1. Structured electronic susceptibility

To determine the nature of the CDW instability in VSe_2, we first compute its electronic structure using an *ab initio* calculation within the local density approximation (LDA), based on the all-electron full-potential linear augmented plane wave Elk code [195].[2] We used the experimental lattice parameters of $a = 3.356\,\text{Å}$, $c = 6.104\,\text{Å}$, and the relative distance of the Se planes from the V planes $z_{\text{Se}} = 0.25$ [196]. Relaxation of the Se position did not significantly affect the band structure or the computed value of the Fermi energy ($E = 0$). We used a mesh of $32 \times 32 \times 24$ **k**-points in the full Brillouin zone (> 2000 in the irreducible wedge) to achieve convergence. In agreement with earlier computations, our *ab initio* calculations show only a single band crossing the Fermi level, of predominantly vanadium, 3*d*-orbital character, which significantly disperses along k_z (see Figure 5.1). We evaluated the energies for this band on a $100 \times 100 \times 400$ **k**-point mesh for subsequent calculations of the Lindhard response function, as well as the structured susceptibility, which includes a momentum-dependent EPC. Because *ab initio* predictions of the Fermi energy may vary slightly from experimentally observed levels, and because non-stoichiometry and self-intercalation in VSe_2 samples are known to affect the precise value of the Fermi energy [197], we shift all of our obtained eigenenergies up by 20 meV to obtain a best-fit value for E_{F} compared to the experimental Fermi level.

For the EPC matrix elements, we use the expression derived by Varma *et al.* [166], introduced in Section 4.3. In the case of a single band crossing E_{F}, the expression simplifies to:

$$\mathbf{g}_{\mathbf{k},\mathbf{k}+\mathbf{q}} \propto \frac{\partial \epsilon_{\mathbf{k}}}{\partial \mathbf{k}} - \frac{\partial \epsilon_{\mathbf{k}+\mathbf{q}}}{\partial \mathbf{k}}. \tag{5.1}$$

Here, $\epsilon_{\mathbf{k}}$ is the electronic dispersion taken from the density-functional theory

[2] The density functional theory calculations were performed by Jude Laverock (University of Bristol).

calculation. The direction of the vector $\mathbf{g}_{\mathbf{k},\mathbf{k+q}}$ indicates the polarisation of the phonons coupled to. The displacements of vanadium atoms associated with the CDW transition are known to be purely in-plane and longitudinal [198]. From here on, we therefore consider only the component of the EPC vector parallel to the in-plane phonon momentum: $g_{\mathbf{k},\mathbf{k+q}} = \mathbf{g}_{\mathbf{k},\mathbf{k+q}} \cdot \mathbf{q}_\parallel / |\mathbf{q}_\parallel|$.

Using this form of $g_{\mathbf{k},\mathbf{k+q}}$, we can compute the structured electronic susceptibility introduced in Section 4.3.1. Since VSe_2 falls in the weak-coupling regime, it is sufficient to use the random phase approximation (RPA), and neglect vertex corrections, which should be small [199]. The renormalised phonon propagator is then described by $D_{\mathrm{RPA}} = (D_0^{-1} - D_2)^{-1}$, with bare phonon propagator D_0 and structured electronic susceptibility D_2, given by [158, 164]:

$$D_2(\mathbf{q}) = -\sum_{\mathbf{k}\in\mathrm{BZ}} |g_{\mathbf{k},\mathbf{k+q}}|^2 \frac{f(\epsilon_\mathbf{k}) - f(\epsilon_{\mathbf{k+q}})}{\epsilon_\mathbf{k} - \epsilon_{\mathbf{k+q}} + i\delta}. \tag{5.2}$$

Here, $f(\epsilon)$ is the Fermi-Dirac distribution function and we use a small regulator $\delta = 0.1\,\mathrm{meV}$. The Lindhard function $\chi(\mathbf{q})$ is defined as the above, but taking $g_{\mathbf{k},\mathbf{k+q}} = 1$:

$$\chi(\mathbf{q}) = -\sum_{\mathbf{k}\in\mathrm{BZ}} \frac{f(\epsilon_\mathbf{k}) - f(\epsilon_{\mathbf{k+q}})}{\epsilon_\mathbf{k} - \epsilon_{\mathbf{k+q}} + i\delta}. \tag{5.3}$$

The full $g_{\mathbf{k},\mathbf{k+q}}$ enters the renormalised phonon dispersion via D_2 in the RPA calculation: $\Omega^2_{\mathrm{RPA}}(\mathbf{q}) = \Omega^2_0(\mathbf{q}) - \Omega_0(\mathbf{q}) D_2(\mathbf{q})$. Here, $\Omega_0(\mathbf{q})$ is the bare (high-temperature) phonon dispersion [159]. At T_{CDW}, phonons will exhibit a Kohn anomaly such that $\Omega_{\mathrm{RPA}}(\mathbf{Q}_i) = 0$. As long as $\Omega_0(\mathbf{q} \approx \mathbf{Q}_i)$ has no sharp features, the maximum of $D_2(\mathbf{q})$ close to T_{CDW} will lie at $\mathbf{q} = \mathbf{Q}_i$.

In Figure 5.2 we show $\chi(\mathbf{q})$ and $D_2(\mathbf{q})$ for three values of q_z, while q_x and q_y span one reciprocal lattice vector each. We set the temperature to 100 K, close to T_{CDW}. $D_2(\mathbf{q})$ is not periodic across Brillouin zones, because of the projection of $\mathbf{g}_{\mathbf{k},\mathbf{k+q}}$ onto the in-plane radial direction of $\mathbf{q}$. It is clear from Figure 5.2 that χ disperses significantly less than D_2, and is far-removed from a divergence. This is indicative of the small degree of nesting in VSe_2. We find that the maxima of both χ and D_2 at $q_z = 0.31$ lie close to $(q_x, q_y) = (0, 0.25)$ (in reciprocal lattice units, rlu), in agreement with the experimentally observed in-plane value [181].

In Figure 5.3, we take a closer look at the out-of-plane variation of $\chi(\mathbf{q})$ and $D_2(\mathbf{q})$ at $q_x = 0$, for five different values of q_y. To get a more complete picture, we also see what happens when we artificially shift the Fermi level by 10 or 20 meV. We note that at E_{F}, the highest peak in the susceptibility actually lies at $q_y = 0.26\,\mathrm{rlu}$.[3] Deviations of the peak position of the order

[3]Notice that we are limited by the resolution of the band structure calculation, $\delta q_x = \delta q_y =$

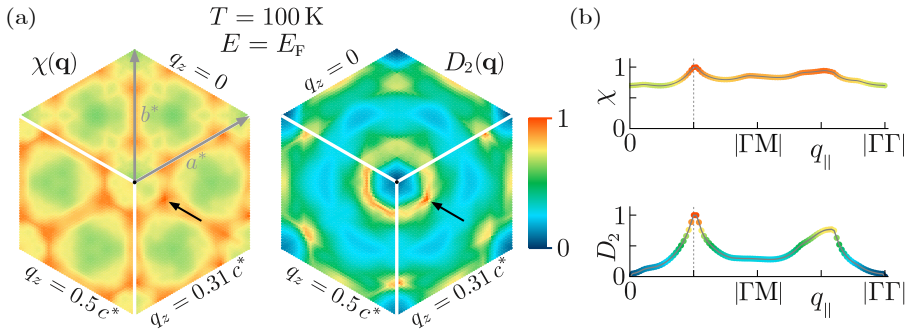

Figure 5.2: (a) The Lindhard function $\chi(\mathbf{q})$ (left) and the structured susceptibility $D_2(\mathbf{q})$ (right) at $T = 100\,\mathrm{K}$ as a function of in-plane $q_\parallel$ (with $q_\parallel = 0$ indicated by the black dot), at various values of q_z. Both graphs are normalised to their respective maxima, which lie around $\mathbf{q} = (0, 0.25, 0.31)\,\mathrm{rlu}$ and symmetry-related positions (black arrows). (b) Line cuts of the Lindhard function and structured susceptibility at $q_z = 0.31c^*$, varying $q_\parallel$ along a line through the black arrows in (a).

of the in-plane $\mathbf{k}$-mesh resolution of 0.01 rlu are not expected to have observable consequences, because as long as the peak is close to commensurate, the coupling between the CDW order parameter and the lattice (neglected here) is prone to locking the in-plane component of the CDW wavevector into the lattice-preferred commensurate value [200, 201]. We expect no lock-in effect in the out-of-plane direction, because the peak in susceptibility is further from low-period commensurate values, inter-layer coupling is weak [124], and the atomic displacements are purely in-plane [198]. This agrees with the observed values of Q_z remaining incommensurate at all temperatures [181].

Aside from this, Figure 5.3 demonstrates several things. First, the peaks lie close to the experimentally determined wavevectors in all cases, even allowing for small shifts of the Fermi energy. This is a good sign, because it indicates that our theory is capturing the correct physics. The fact that the peaks remain relatively broad is not unexpected, because the band structure of VSe_2 is highly 3D and poorly nested, and we are considering $T = 100\,\mathrm{K}$. Often in the literature, the electronic susceptibility is only computed at low temperatures, which naturally makes any peaks in the susceptibility sharper. However, χ and D_2 are strictly only valid above T_CDW, and the effect of the thermal occupation of states may be non-trivial. Finally, by comparing D_2 and χ we can see that the structure of the electron-phonon coupling selectively amplifies and suppresses the various sub-peaks that make up the Lindhard function. These sub-peaks arise from similar wavevectors connecting pairs of states in different regions of the Fermi surface, so that they generically have different associated electron-phonon coupling strengths. The inclusion of a structured EPC is therefore able to shift the peak positions in the susceptibility.

Finally, we have repeatedly stated that the FS is poorly nested, based on

0.01 rlu, and $\delta q_z = 0.0025\,\mathrm{rlu}$.

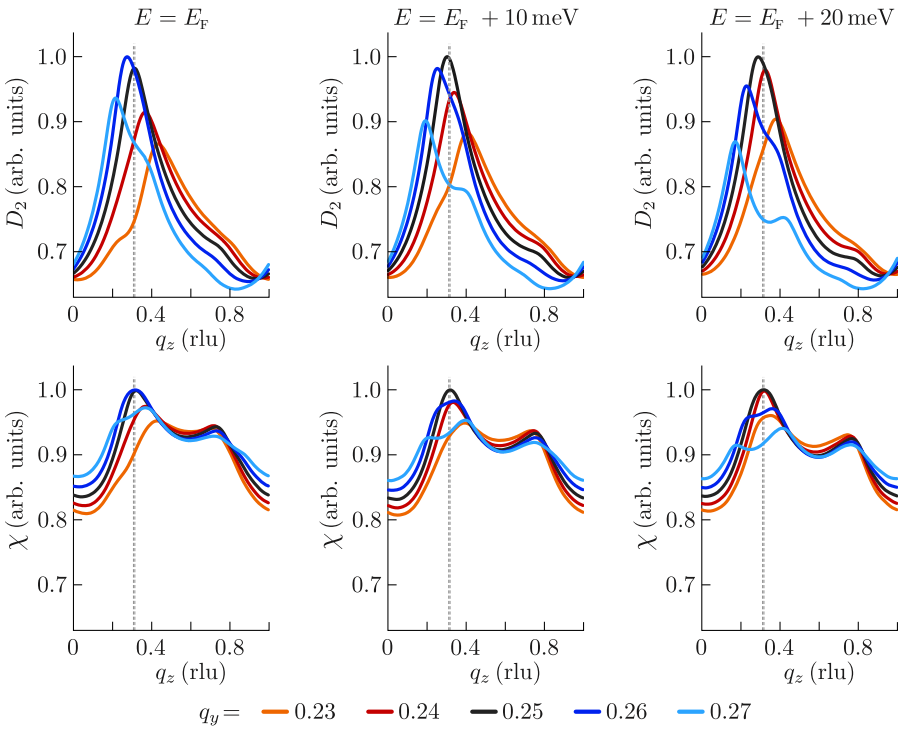

Figure 5.3: The structured susceptibility (top row) and Lindhard function (bottom row) along q_z, at $q_x = 0$ and for various values of q_y, and varying the chemical potential. The two closely-spaced vertical dashed lines correspond to the two experimentally observed values of the out-of-plane component of the CDW wave vector [181]. As before, we have set $T = 100\,\text{K}$. Curves are normalised per panel.

the lack of pronounced, sharp peaks in (the real part of) the Lindhard function. To quantify the degree of nesting, one can also consider the so-called *nesting function* [179]

$$\lim_{\omega \to 0} \text{Im}[\chi(\mathbf{q}, \omega)]/\omega. \tag{5.4}$$

This function is expected to diverge at vectors $\mathbf{q}$ that nest the FS. In the limit of $T = 0\,\text{K}$, the nesting function reduces to $\sum_{\mathbf{k}} \delta(\epsilon_{\mathbf{k}} - E_F)\delta(\epsilon_{\mathbf{k}+\mathbf{q}} - E_F)$ [179]. We are interested in the arguably more physically relevant degree of nesting at $T = 100\,\text{K}$, so we will instead use the form given above, the results of which are plotted in Figure 5.4. Numerically, a finite value for ω is required; considering $\omega = 1\,\text{meV}$ corresponds to computing the degree of nesting between states around the Fermi level separated in energy by 1 meV. The absence of pronounced peaks in these plots, and the fact that the maximum in Figure 5.4 does not coincide with the experimentally observed CDW propagation vector, show once again that VSe_2 is not a well-nested material.

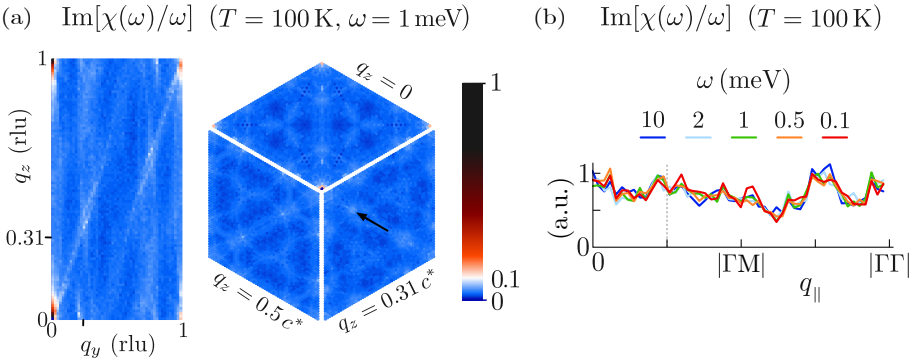

Figure 5.4: (a) The magnitude of the nesting function $\mathrm{Im}[\chi]/\omega$, with $\chi(\mathbf{q},\omega)$ the Lindhard function and $\omega = 1\,\mathrm{meV}$. The rectangular figure is in the $q_y q_z$-plane, with $q_x = 0$, while the hexagonal figure shows the function in the $q_x q_y$-plane for three different values of q_z. The ticks on the axes of the rectangular figure indicate the location of the observed CDW ordering wavevector, also indicated by black arrow in the hexagonal figure. Note the lack of a significant peak at this position. (b) The nesting function for $\mathbf{q}$ along the black arrow shown in (a), at $q_z = 0.31$, for different values of ω. There is no clear nesting peak.

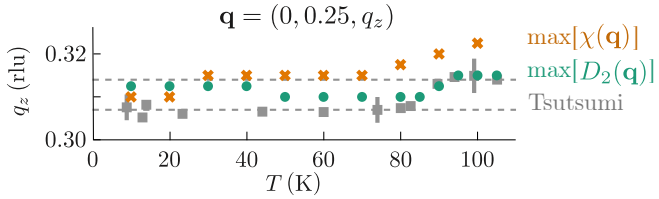

Figure 5.5: The temperature dependence of the position of the maximum of χ (crosses) and D_2 (circles) along the line $\mathbf{q} = (0, 0.25, q_z)$, plotted alongside experimental data reproduced from ref. [181] (squares and dashed line fits).

5.2. Thermally dependent CDW wavevector

Tsutsumi's key experimental observation, which has lead to much speculation regarding the existence of a second, CDW-to-CDW transition in VSe_2, is that the out-of-plane component of the CDW wavevector determined by X-ray diffraction changes from $q_z = 0.314\,c^*$ at 105 K to $q_z = 0.307\,c^*$ below 85 K [181]. In this experiment, X-rays are diffracted by a single crystal of VSe_2, and the positions of the diffraction peaks indicate the periodicities present in the crystal lattice. Because the formation of a CDW changes the crystal symmetries, new peaks arise once the charge order sets in; whose positions correspond to the CDW wavevectors.

We can compare these experimental results to the positions of the peaks in our computed electronic susceptibility at different temperatures. This is equivalent to predicting the CDW ordering wavevector of VSe_2 if we were to quench the system from its high-temperature state directly to the chosen temperature. In Figure 5.5, we plot the maximum of D_2 and χ along the line

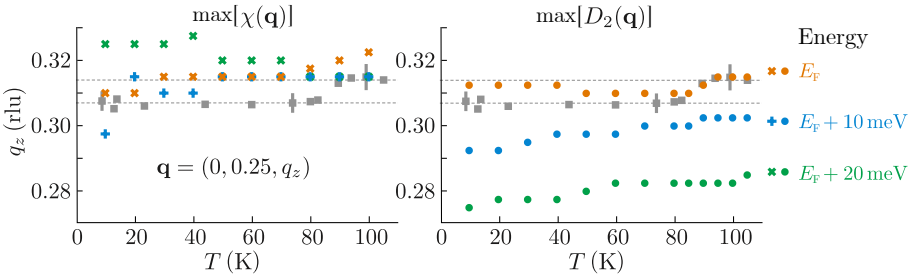

Figure 5.6: The temperature dependence of the maxima of the Lindhard function χ and structured susceptibility D_2 along the line $\mathbf{q} = (0, 0.25, q_z)$, varying the chemical potential. E_F is the experimentally determined Fermi level, which lies 20 meV below the zero energy level of the computed *ab initio* band structure shown in Figure 5.1. The grey data points indicate the experimentally determined charge ordering wavevectors from [181], and the grey dashed lines indicate $q_z = 0.307c^*$ and $q_z = 0.314c^*$. While D_2 shows a clear trend in its temperature dependence, χ does not.

5

$\mathbf{q} = (0, 0.25, q_z)$ as a function of temperature. We find remarkable agreement between the thermal evolution of the peak position of D_2 from 50-105 K and the q_z values observed by Tsutsumi [181]. Importantly, it shows a smooth variation with temperature that quantitatively fits the experimental data points without requiring any discontinuous phase transition.

As mentioned before, variations in the chemical potential may arise from the non-stoichiometry of crystal samples, and might lead to small variations in the experimentally determined CDW wavevectors. Nonetheless, the smooth downward trend in the peak position of D_2 as the temperature is lowered is stable under variation of the chemical potential, as shown in Figure 5.6. In contrast, although the Lindhard function χ in Figure 5.5 shows a temperature variation similar to D_2 for this specific value of E_F, even minute changes in the chemical potential yield a qualitatively different thermal evolution. Figure 5.6 demonstrates that the structure of the electron-phonon coupling can significantly affect not only the position of the maximum of the susceptibility, but also its temperature-dependence.

5.3. The CDW gap

Having established the smooth thermal evolution of the CDW propagation vector in VSe_2, we next turn to its CDW gap structure. Two practical issues contributing to its elusiveness are the small gap size ($2\Delta \approx 24$ meV [124]) and the three-dimensional nature of the electron dispersion, which necessitate experiments with high energy- and k_z-resolution. Several low-temperature ARPES measurements are suggestive of a gap around $k_z \approx 0.5c^*$ [184, 186–188]. The reported gap size of 80-100 meV in ref. [184], however, refers to a shift in peak positions of energy dispersion curves, while the CDW gap is more closely related to the leading edge shift [202]. Refs. [186–188], on the other hand, show spectral weight suppression in Fermi pockets around the L-point even above

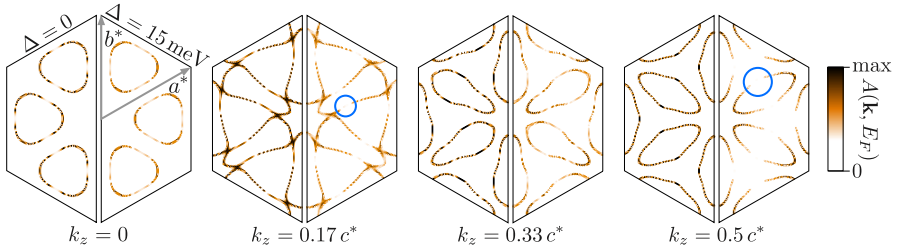

Figure 5.7: The spectral function of VSe_2 at 20 meV above E_F, where the effect of the CDW gap is most pronounced. The four plots correspond to different values of k_z. In each, the left(right) side shows the ungapped(gapped) phase above(below) T_{CDW}. All plots employ the same colour scale. We employed a spectral broadening of $\Sigma = 15i$ meV, and a constant gap $\Delta = 15$ meV. The blue circles highlight two gapped regions separated by $\mathbf{Q} = (0, 0.25, 0.33)$.

T_{CDW}, while ref. [185] has a lower resolution and reports no gaps. The location and shape of the partial CDW gaps in VSe_2 thus remain to be determined conclusively.

Based on the energy dispersion of the band that makes up the FS, we can compute the spectral function $A(\mathbf{k}, \epsilon)$ probed by photoemission experiments in a numerically inexpensive way [159]. This method was introduced in Section 4.3.2, but we will summarise it again here. The electron propagator in the normal state is $G\ (\mathbf{k}, i\omega_n) = \left(i\omega_n - \epsilon_{\mathbf{k}} - \Sigma_{\mathbf{k}} - \mu\right)^{-1}$, where $i\omega_n$ are Matsubara frequencies and μ is the chemical potential. The complex-valued electron self-energy is given by $\Sigma_{\mathbf{k}} = \Sigma'_{\mathbf{k}} + i\Sigma''_{\mathbf{k}}$, and has a real part that shifts the energy of the state at $\mathbf{k}$, while the imaginary part broadens its linewidth. Wick rotating $i\omega_n$ to an energy ϵ and an infinitesimal imaginary part $i\delta$, we obtain the spectral function,

$$A\ (\mathbf{k}, \epsilon) = -\frac{1}{\pi}\mathrm{Im}\left[G\ (\mathbf{k}, \epsilon + i\delta)\right]. \tag{5.5}$$

We assume $\Sigma'_{\mathbf{k}} = 0$ and for $\Sigma''_{\mathbf{k}}$, which describes the experimental resolution, we use a constant value of 15 meV. We obtain the normal-state spectral function at E_F ($\epsilon = 0$) shown in the left halves of the hexagonal plots in Figure 5.7.

To predict where gaps will open up in the spectral function as the CDW order sets in, we use a similar method to that developed in the context of superconductivity by Nambu [171] and Gor'kov [172]. Rather than constructing a new field theory starting from propagators with the symmetries of the ordered state, we complement the disordered propagators with additional, anomalous electron propagators

$$F^{\mathbf{k}_1}_{\mathbf{k}_2} = \langle \psi_{\mathbf{k}_1}\, \bar{\psi}_{\mathbf{k}_2} \rangle \tag{5.6}$$

that do not conserve momentum up to one CDW wavevector. $\bar{\psi}_{\mathbf{k}}$ creates an electron with momentum $\mathbf{k}$, and $\mathbf{k}_1 - \mathbf{k}_2 = \pm\mathbf{Q}_i$, with $\mathbf{Q}_{1,2,3}$ the three CDW wavevectors. Since the CDWs in VSe_2 are incommensurate, an infinite

number of different $F^{\mathbf{k}_1}_{\mathbf{k}_2}$ could be constructed. For the sake of computation, we approximate $Q_i^z = \frac{1}{3}\mathbf{c}^*$ for all propagation vectors. Further noting that $12\mathbf{Q}_i = \mathbf{0}$ and $\sum_i \mathbf{Q}_i = \mathbf{c}^*$, we can represent all possible $\mathbf{k}_1$ and $\mathbf{k}_2$ by $\mathbf{k} + m\mathbf{Q}_1 + n\mathbf{Q}_2$ (with $m, n \in [0, 11]$). Doing so, we generate a matrix $\hat{G}^{\mathrm{CDW}}$ whose elements are the renormalised electron propagators $G^{\mathrm{CDW}}(\mathbf{k}+m\mathbf{Q}_1+n\mathbf{Q}_2)$ on the diagonal, and anomalous propagators $F^{\mathbf{k}_1}_{\mathbf{k}_2}$ and $(F^{\mathbf{k}_1}_{\mathbf{k}_2})^\dagger$ for any off-diagonal element with $\mathbf{k}_1$ and $\mathbf{k}_2$ differing by exactly one $\mathbf{Q}_i$. We then construct a matrix Dyson equation:

$$\hat{G}^{\mathrm{CDW}} = \hat{G} + \hat{G}\hat{\Sigma}\hat{G}^{\mathrm{CDW}} \quad \Rightarrow \quad \hat{G}^{\mathrm{CDW}} = \left(\hat{I} - \hat{G}\hat{\Sigma}\right)^{-1}\hat{G}. \tag{5.7}$$

$\hat{G}$ is a diagonal matrix of bare propagators evaluated at momenta $\mathbf{k} + m\mathbf{Q}_1 + n\mathbf{Q}_2$; $\hat{\Sigma}$ is a matrix with self-energies on the diagonal and gaps Δ in off-diagonal elements connected by one $\mathbf{Q}_i$; and $\hat{I}$ is the identity matrix. Solving this equation for the top left element of $\hat{G}^{\mathrm{CDW}}$, we find $G^{\mathrm{CDW}}(\mathbf{k})$, and hence the spectral function in the presence of a CDW gap (using Equation 5.5). This method provides an inexpensive way to predict the gap structure of any CDW system, given only the band structure and the ordering wavevectors.

We find that some portions of the spectral function are suppressed from around approximately 20 meV above E_{F}, as shown in Figure 5.7. For completeness, in Figure 5.8 we contrast the gap structure at $E_{\mathrm{F}} + 20\,\mathrm{meV}$ to what we find at E_{F}. The offset of this CDW gap from E_{F} is not surprising, since the structuring of the EPC will generically stabilise a CDW with wave vectors that do not nest the Fermi surface, and therefore do not necessitate any particle-hole symmetry (in contrast, for example, to a superconducting gap). Indeed, asymmetric CDW gaps have been observed in various TMDCs before [203]. The positive offset found here is consistent with STS results, which show a suppression of the density of states with width $2\Delta = (24 \pm 6)\,\mathrm{meV}$ centered at 10 meV above E_{F} [124].

The clearest gaps in the computed spectral function appear on the long sides of the oval-shaped lobes around the L point ($k_z = 0.5c^*$). These gaps are connected to others at $k_z = 0.17c^*$ by a CDW wavevector, as indicated by blue circles in Figure 5.7. Planes at other k_z values are either unaffected by the CDW or experience a moderate loss of spectral weight. It is probable that the true gap function $\Delta(\mathbf{k})$ in VSe_2 depends on $\mathbf{k}$. Obtaining a self-consistent solution for the gap function, which explicitly incorporates the EPC structure, is possible in principle [159], but the three-dimensional nature of the electron dispersion implies a significant computational cost. Moreover, including momentum dependence in $\Delta(\mathbf{k})$ can only change the relative sizes of gaps and will not allow additional gaps to open on top of those already observed in Figure 5.7. The locations highlighted by blue circles in Figure 5.7 are thus the primary candidates for observing the elusive CDW gap in VSe_2.

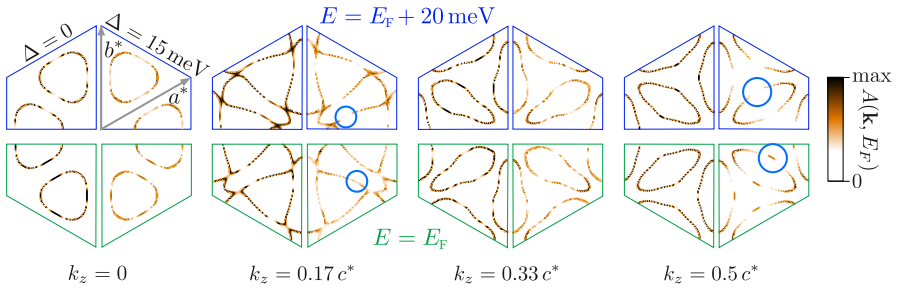

Figure 5.8: The spectral function of VSe_2, for various values of k_z. The left(right) side of each plot shows the ungapped(gapped) phase above(below) T_{CDW}. The top(bottom) half of each plot shows the spectral function 20 meV above E_F (at E_F). All plots employ the same colour scale. We employed a spectral broadening of $\Sigma = 15i$ meV, and a constant gap $\Delta = 15$ meV. The blue circles highlight regions regions separated by one CDW wavevector.

5.4. Discussion and conclusion

We have shown that the structured susceptibility in 1T-VSe_2, which includes the momentum-dependence of the electron-phonon coupling, shows a sharp peak at the experimentally observed CDW ordering vector. Moreover, its temperature dependence reproduces the thermal evolution of the CDW wavevectors observed by X-ray diffraction experiments. Our results demonstrate that this thermal variation is an intrinsic effect, whose observation does not necessitate a description in terms of multiple consecutive CDW phases. Additionally considering the error margins of the reported X-ray diffraction data (see Figure 5.5), the lack of indicators for a second transition in thermodynamic probes [122, 182, 183], and the fact that satellite dark-field phase contrast may be due to a natural phase variation of the CDWs [192], we suggest that VSe_2 hosts a single CDW phase. The resolution of this discussion by the effect of a structured electron-phonon coupling brings VSe_2 in line with more strongly coupled CDW materials in which temperature-dependent incommensurate CDW ordering wavevectors are commonly observed [200].

Based on a computation of the spectral function, we predict the elusive CDW gap in VSe_2 to appear as localized suppressions of spectral weight centered above E_F, most pronounced on the sides of the Fermi surface lobes around $k_z = 0.17c^*$ and $k_z = 0.5c^*$. The degree of localization and offset from the Fermi energy reflect the weakness of the nesting in this system. High-resolution, k_z-resolved ARPES at varying temperature should be able to resolve the opening of the predicted CDW gaps.

The results reported here for the specific CDW material VSe_2 fit into a larger picture of structured electron-phonon coupling being essential to the quantitative understanding of any charge ordered material. That is, in an ideal single-band, one-dimensional (1D) model for a metal, a Peierls transition may be signalled in the Lindhard function, which describes the (bare) electronic susceptibility and which diverges in 1D metals at the wavevector $Q = 2k_F$ connecting the two Fermi surface points [126, 129]. In real materi-

als, however, perfect FS nesting never occurs, and inspection of the Lindhard function commonly indicates either no clear peak, or a dominant peak at a wavevector inconsistent with the observed CDW [179]. Examples of supposedly nesting-driven density wave materials for which this was demonstrated explicitly include $2H$-$NbSe_2$ and $2H$-$TaSe_2$ [158, 159, 179, 204], $TbTe_3$ and other rare-earth tellurides [152, 179, 205, 206], blue bronze ($K_{0.3}MoO_3$) [180], and chromium [207]. Even for materials with electronic band structures that are considered well-nested, the assumption that density waves arise purely from FS nesting is thus demonstrably incomplete.

In contrast, the structured susceptibility, which includes the momentum and orbital dependent electron-phonon coupling, has been shown to agree with experimental observations in a range of real CDW materials. We have already mentioned the example of the prototypical strong-coupling, quasi-two-dimensional CDW compound $2H$-$NbSe_2$, for which incorporating the momentum and orbital-dependence of the EPC was shown to correctly predict the wavevector of its electronic instability [158, 159, 164, 208]. Similarly, the concept of 'hidden nesting', taking into account the real-space shape and orientation of valence orbitals in CDW formation, effectively corresponds to including an orbital-dependent EPC [149–152]. The need for including a coupling structure more generally, however, is typically associated with the strong-coupling nature of specific materials, and is far from standard practice [129, 179, 180, 205, 206, 209].

The results presented here for the weakly coupled, single-band material VSe_2 highlight the need for considering the structure of the electron-phonon coupling in quantitative models for any density wave material, regardless of its dimensionality, coupling strength or degree of nesting. Besides the momentum-dependence considered here, the coupling may in general also depend on orbital character and even spin.[4] All of these contribute to the physical properties of density wave materials, and understanding their quantitative impact is indispensable in understanding the emergence of and interaction between charge, orbital, and magnetic order throughout (unconventional) superconductors, magnets, and (multi)ferroics.

[4] A spin-dependent EPC could arise in magnetic systems with spin-polarised electron bands.

6

Coexisting charge-ordered states in ML-VSe_2

Bulk materials hosting charge density waves (CDWs), when reduced to ultrathin films, have shown CDW enhancement and tunability. Systematic scanning tunnelling microscopy experiments reveal that bilayer VSe_2 largely retains the bulk electronic structure, hosting a tri-directional CDW. However, monolayer (ML-)VSe_2 – consistently across distinct substrates – exhibits a dimensional crossover, hosting two CDWs with distinct wavelengths and transition temperatures. Electronic structure calculations reveal that while one CDW is bulk-like and arises from the well-known Peierls mechanism, the other is decidedly unconventional. The observed CDW-lattice decoupling and the emergence of a flat band suggest that the second CDW could arise from enhanced electron-electron interactions in the 2D limit. These findings establish ML-VSe_2 as a host of coexisting charge orders with distinct origins, and demonstrate emergent interactions in a 2D material. This chapter is adapted from ref. [3].

In layered materials, CDWs often exist in proximity to other ordered phases, *e.g.* superconductivity and magnetism [210], due to a precarious balance between competing interactions. Approaching the two-dimensional (2D) limit enhances the potential for such interplay [211], while providing new knobs to tune electronic phases, such as electric fields and strain [212–215]. Notably, electron-electron interactions in the 2D limit are expected to induce competition among different CDW driving mechanisms as well as other ordered states [216–218]. In practice, however, a crossover towards electronic charge order driven by dimensional reduction remains to be discovered.

Transition metal dichalcogenides (TMDCs) are well-studied hosts of conventional and unconventional CDWs [129, 146, 158, 200, 210]. The tunability of CDWs in the ultrathin limit of several TMDCs is particularly relevant to practical electronic applications [213–215, 219, 220]. In Chapter 5 we discussed the TMDC 1T-VSe2. Bulk VSe_2 is paramagnetic, with a three-

dimensional (3D) Fermi surface (FS). Below temperature $T_{\mathrm{CDW}}^{\mathrm{bulk}} \sim 110\,\mathrm{K}$, it hosts a triple-$Q$ (triangular) CDW with 3D character. The CDW periodicity $\lambda_{\mathrm{CDW}} \simeq 4a \times 4a \times 3c + \delta$ is commensurate with the in-plane lattice constant a, but incommensurate with the inter-layer distance c. The 3D nature of the FS makes nesting in this material extremely weak, and we demonstrated in the previous chapter that understanding the CDW phase in this system requires consideration of a structured electron-phonon coupling (EPC) [2, 185].

In this chapter, we consider what happens to this system when we reduce its dimensionality. It has been demonstrated that for thicknesses below 20 nm, the FS of 1T-VSe_2 transitions to 2D character, while maintaining triple-Q, $4a$ CDW order [122]. However, monolayer (ML)-VSe_2, grown epitaxially in several recent works, purportedly hosts a ground state with concomitant charge and spin orders, the nature of which is controversial [188, 221, 222]. First, while some claim the $4a$ CDW to be absent even at low temperatures [188, 221], others indicate its persistence to well above room temperature [222]. Second, several works report incommensurate superstructures with varying periodicities, *viz.* $\sqrt{3}a \times 2a$, $\sqrt{3}a \times \sqrt{7}a$, and $\sim 2a \times 3a$ [188, 221–223], whose purported origins vary from structural distortions to nested CDWs. The relation of all these superstructures – identified via electronic density distributions over small real-space regions – to any long-ranged charge order remains unclear. Finally, magnetism is suggested to emerge in ML-VSe_2 despite its absence in the bulk [221, 224], but both its existence and interplay with charge order are actively debated [225, 226]. Disentangling these apparently conflicting observations is paramount to revealing the true nature of charge order in ML-VSe_2, its driving mechanism, and its ramifications on other phases. This requires a controlled and systematic study of the CDW under varying thermodynamic conditions.

To remedy this, we performed a comprehensive experimental and theoretical investigation of charge order in ultrathin epitaxial 1T-VSe_2.[1] Scanning Tunnelling Microscopy (STM) and non-contact Atomic Force Microscopy (nc-AFM) experiments show that while the CDW in bilayer (BL)-VSe_2 is closely related to that in bulk, charge order in ML-VSe_2 is qualitatively different. By systematically varying substrates, film thickness, and temperature, we find that ML-VSe_2 consistently hosts two unidirectional (single-Q) CDWs with periods $4a$ and $2.8a$, with strikingly distinct phenomenologies. Band structure calculations elucidate that while the $4a$ CDW is stabilized by conventional FS nesting and EPC, the $2.8a$ CDW cannot be explained by such mechanisms. Instead, we find the $2.8a$ instability to originate from a flat band region, wherein electron-electron interactions are expected to be strongly enhanced. Our results establish ML-VSe_2 as a host of coexisting CDWs with distinct driving mechanisms, demonstrating the potential of correlations for tuning electronic

[1] My part in this collaborative project included constructing a tight-binding model, computing and analysing the electronic susceptibility based on this model, and aiding in the overall interpretation of the combined experimental and theoretical results.

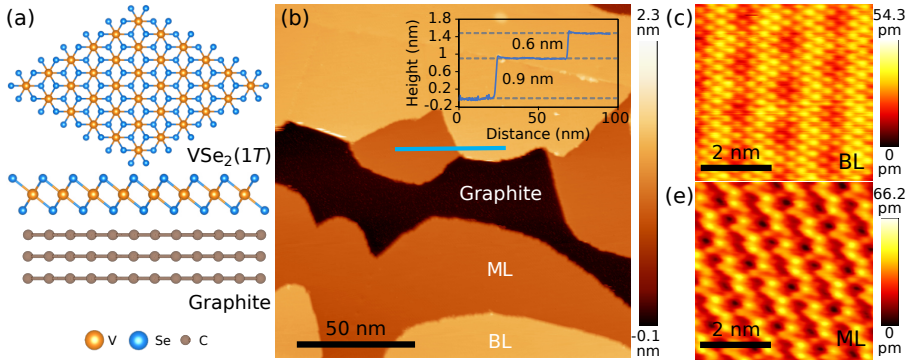

Figure 6.1: (a) Top view (top) and side view (bottom) of the atomic structure of 1T-VSe_2 on graphite substrate. (b) Large field-of-view STM topograph ($150\times150\,nm^2$, bias voltage $V_{tip} = 0.7\,V$, current setpoint $I_{set} = 100\,pA$) of MBE-grown epitaxial VSe_2 on a HOPG substrate. The average thickness of 1.5 VSe_2 layers resulted in monolayer (ML) and bilayer (BL) VSe_2 regions identified within the image. Inset shows the height profile across layers, with the respective step heights indicated. (c-d) Atomically resolved STM topographs ($5 \times 5\,nm^2$, $V_{tip} = -0.2\,V$, $I_{set} = 200\,pA$) of BL (c) and ML (d) VSe_2 at 78 K. Both topographs show a hexagonal lattice with visibly distinct superstructures.

phases in the 2D limit.

6.1. Experimental Results

The scanning probe microscopy experiments for this project were performed by Rebekah Chua, Yuli Huang, Jian Gou, and Xiaoyue He at the National University of Singapore. In STM, a sharp metallic tip is brought close to the surface of a material, and the tunnelling current between the tip and the sample is measured. With this method, we probe the local density of states, and are able to 'see' individual atoms as well as charge density modulations on the surface of the material probed. In nc-AFM, an oscillating cantilever with a sharp tip at the end is brought close to the surface of a material, such that local force interactions allow one to determine the surface structure. Importantly, AFM is predominantly sensitive to the atomic positions, rather than CDWs. For a more extensive introduction to these methods, we refer the reader to refs. [227, 228].

6.1.1. STM and nc-AFM Imaging Experiments

Thin 1T-VSe_2 films were grown on highly oriented pyrolytic graphite (HOPG) and MoS_2 substrates in a home-made, ultrahigh-vacuum molecular beam epitaxy (MBE) system, the growth chamber of which has a base pressure of 2×10^{-9} mbar. Both substrates are known to stabilize the 1T polymorph of VSe_2 [221] whose crystal structure is shown in Figure 6.1a. The substrates were exfoliated *ex-situ*, immediately transferred into the MBE chamber, and then outgassed at 420°C for 3 hours before MBE growth. The VSe_2 samples

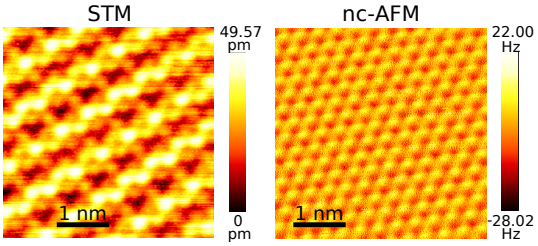

Figure 6.2: Comparison of atomic resolution topographs ($4 \times 4\,\mathrm{nm}^2$) of ML-$VSe_2$ on HOPG at $T = 78\,\mathrm{K}$ acquired by (a) STM ($V_{\mathrm{tip}} = -0.7\,\mathrm{V}$, $I_{\mathrm{tip}} = 220\,\mathrm{pA}$), and (b) non-contact AFM techniques. Superstructures are visible in (a), but not in (b).

were grown by simultaneously evaporating V and Se using an electron-beam evaporator and a Knudsen cell, respectively, onto the substrates maintained at 360°C. The Se/V ratio was high, and Se was controlled to be in excess. A selenium capping layer was deposited onto the VSe_2 surface to prevent direct ambient contamination during *ex-situ* transport to the varying temperature STM/nc-AFM system for subsequent measurements. The capping layer was removed by annealing at 240°C for 30 minutes in the microscope chamber.

STM and nc-AFM measurements were performed over 78-204 K in an Omicron UHV system interfaced to a Nanonis controller equipped with STM/qPlus sensor and an electrical local heater. To reduce thermal drift during data acquisition, the STM was first allowed to stabilise at each temperature. Electrochemically etched tungsten tips were used with bias voltage applied to the tip, while the sample holder was grounded. STM images were acquired using constant current mode. For nc-AFM imaging, the constant-height mode with an oscillation amplitude of 10 nm was used to record the frequency shift of the qPlus resonator (sensor frequency $f_0 \approx 24\,\mathrm{kHz}$, $Q \approx 8000$). A lock-in technique was used to measure dI/dV spectra, with a modulation of 625 Hz and 30 mV.

The films were characterized *in-situ* using STM over temperatures of 77-200 K. As shown in Figure 6.1b, controlled growth of an average thickness of 1.5 layers resulted in the formation of both ML- and BL-VSe_2 regions (on HOPG) within fields-of-view accessible to STM imaging. Topographic characterization of a terraced region at 78 K (Figure 6.1b: inset) reveals step heights of 0.9 nm and 0.6 nm for the first and second VSe_2 layers respectively, in line with values reported previously [222].

Figure 6.1c-d display atomic resolution topographs obtained in the BL and ML regions, respectively. As expected, both cases show a hexagonal arrangement of atoms, with lattice constant $a \simeq 0.34\,\mathrm{nm}$ [221, 222]. Meanwhile, the atomic-scale superstructures seen on ML- and BL-VSe_2 appear starkly different. For BL-VSe_2 (Figure 6.1c), the superstructure is tri-directional, *i.e.* it manifests along all three lattice directions with a single lengthscale. This is very similar to that of the triple-Q CDW reported in bulk and thinned 1T-VSe_2 crystals [122]. In contrast, for ML-VSe_2 (Figure 6.1d), the superstructure appears unidirectional, and has multiple lengthscales, consistent with recent re-

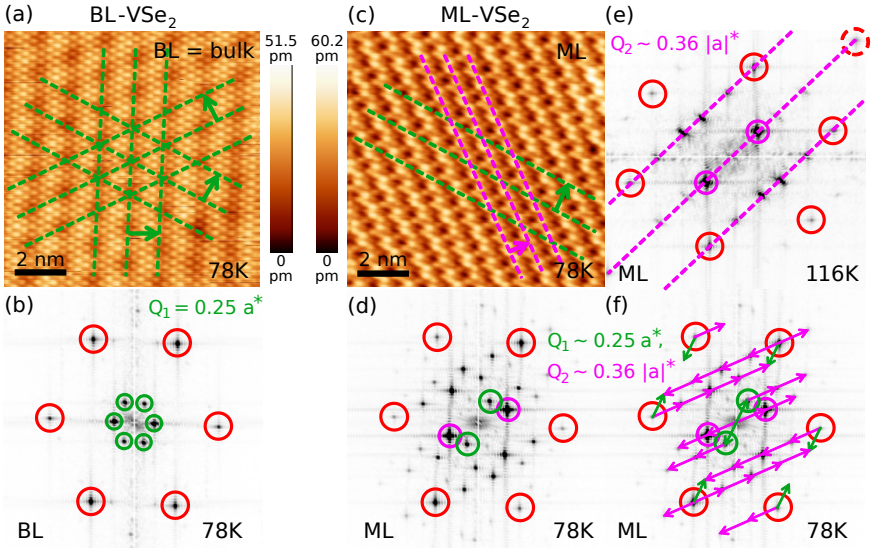

Figure 6.3: Comparison of CDWs in BL and ML-VSe_2. (a-d) STM topographs (a, c: $10 \times 10\,\mathrm{nm}^2$, $V_{\mathrm{tip}} = -0.2\,\mathrm{V}$, $I_{\mathrm{tip}} = 200\,\mathrm{pA}$) and their respective Fourier Transforms (FTs: b, d) acquired at 78 K on BL- (a-b) and ML- (c-d) VSe_2 from adjacent terraces with no observable grain boundary. Dashed colour-coded lines in (a, c) represent the real space CDW wavefronts, and corresponding circles in (b, d) denote the respective CDW wavevectors $\mathbf{Q}_1$ (b, d: green) and $\mathbf{Q}_2$ (d: magenta), whose magnitudes are indicated in reciprocal lattice units (rlu). Red circles denote atomic Bragg peaks in all FT images. (e) FT of STM topograph acquired on ML-VSe_2 at 116 K. Magenta circle denotes the $\mathbf{Q}_2$ peak, while the $\mathbf{Q}_1$ peak is absent. Dashed lines indicate the orientation of $\mathbf{Q}_2$ and its harmonics with respect to the Bragg peak (red circle). (f) Annotated FT of ML-VSe_2 at 78 K (*cf.* data in d). Green ($\mathbf{Q}_1$) and magenta ($\mathbf{Q}_2$) circles identify the primary CDW peaks. Color-coded arrows indicate the positions of harmonics with respect to primary and Bragg peaks. All peaks can be accounted for this way.

sults reported by other groups [221, 222].

Crucially, complementary imaging of the ML using non-contact atomic force microscopy under similar conditions, shown in Figure 6.2, shows no corrugations beyond those of the atomic lattice. This contradicts a statement in ref. [222], where it was claimed that the superstructures that could be seen on top of the expected modulation with period $4a$ were purely structural distortions. Meanwhile, the expected magnitude of a periodic lattice distortion associated with CDWs is $\sim 10^{-2}\,a$, *i.e.* well below the resolution of available microscopy techniques. Based on our data, we conclude that the superstructures observed in STM imaging of ML-VSe_2 are more likely of electronic origin, and putatively regard them as CDWs.

In light of conflicting reports on the CDW phenomenology in ultrathin VSe_2, we systematically examine the CDW modulations from larger STM topographs obtained for both BL and ML cases, in Figure 6.3. For BL-VSe_2, Figure 6.3b shows the Fourier transform (FT) of a typical STM topograph.

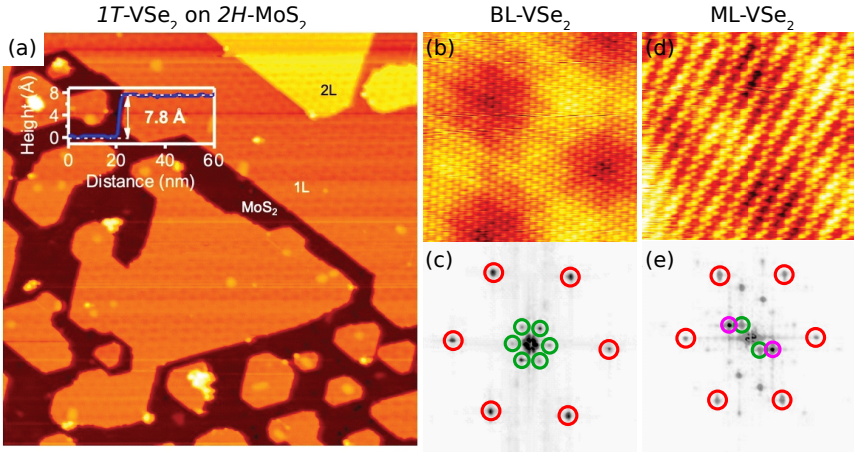

Figure 6.4: (a) Large-scale STM topograph ($200 \times 200\,\mathrm{nm}^2$; $V_{\mathrm{tip}} = 2.4\,\mathrm{V}$, $I_{\mathrm{tip}} = 100\,\mathrm{pA}$) of ultrathin 1$T$-$VSe_2$ grown on 2H-MoS_2. Inset: line profile showing that the first VSe_2 layer is $\sim 7.8\,\text{Å}$ above the substrate. (b-e) Atomic resolution low-temperature) STM topographs ($10 \times 10\,\mathrm{nm}^2$) of BL- (b) and ML-$VSe_2$ (c) at 78 K, and their respective Fourier transforms (FTs). $I_{\mathrm{tip}} = 180\,\mathrm{pA}$ in (b, d), $V_{\mathrm{tip}} = 10\,\mathrm{mV}$ in (b) and $-10\,\mathrm{mV}$ (d). Figure adapted from [226].

6

Here we find prominent peaks at $\mathbf{Q}_1 \simeq 0.25\mathbf{a}^*$ (green circles), where $\mathbf{a}^*$ is the reciprocal lattice vector, with C_6 symmetry, *i.e.* along all three Bragg directions. Meanwhile, the anisotropy of Bragg peak intensities may indicate either local uniaxial strain within the sample, or asymmetry in the tip shape. Regardless, these observations are consistent with the triple-Q, $4a$ CDW reported in bulk and thinned $1T-VSe_2$ crystals [122].

In contrast, the FT for ML-VSe_2 shown in Figure 6.3d appears more complex, with only C_2 symmetry present. The ML shows the persistence of the $\mathbf{Q}_1 \simeq 0.25\mathbf{a}^*$ peak (green circle) along a single Bragg direction, corresponding to a single-Q, $4a$ CDW. However, the most prominent Fourier peak for the ML is seen at $|\mathbf{Q}_2|$, of length $\simeq 0.36\,\mathrm{rlu}$[2] at an angle $\theta_{12} \sim 30°$ relative to the Bragg direction (magenta circle). As shown in Figure 6.3f, a careful inspection of the FT for the ML suggests that all remaining Fourier peaks can be assigned to higher harmonics or Bragg reflections of $\mathbf{Q}_1$ and $\mathbf{Q}_2$, including previously reported multiplet superstructures [188, 222, 223]. While such superstructures may, in principle, be identified with several distinct wavelengths over small topographic regions, such identifications are not consistent over length scales above 5 nm in any of the reported data [188, 222, 223]. Instead, we propose that these apparent supercells are merely the result of superposing two single-Q CDWs, one of which is aligned away from a high-symmetry direction and also incommensurate with the atomic lattice.

Finally, the STM data shown so far corresponds to VSe_2 grown on a HOPG

[2] $1\,\mathrm{rlu} = |\mathbf{a}^*|$; this is one reciprocal lattice unit.

substrate. To ensure that our findings are substrate-independent, we compare these results to samples grown in similar conditions on $2H$-MoS_2, previously reported in ref. [226]. A large-scale STM topograph, shown in Figure 6.4a, indicates that the first VSe_2 layer lies 7.8 Å above the substrate. The remaining panels in Figure 6.4 show atomic resolution zoom-ins of defect-free regions corresponding to BL- and ML-VSe_2. The slight lattice mismatch between VSe_2 and the substrate generates a hexagonal moiré superstructure, which is clearly visible in the topographs (Figure 6.4b,d). The new supercell consists of 17×17 VSe_2 unit cells atop 18×18 MoS_2 unit cells [226]. In contrast, no moiré pattern was observed for ultrathin VSe_2 on HOPG for any setpoint. The FTs of the zoomed-in topographs demonstrate, however, that aside from the difference in moiré intensity, the same CDW peaks are present for VSe_2 grown on $2H$-MoS_2 as seen for VSe_2 grown on HOPG. This agreement limits the potential role of substrate-induced strain effects in driving CDW formation. We conclude that BL-VSe_2 hosts a triple-Q, $4a$ CDW phase just like the bulk (green circles in Figures 6.3b and 6.4c), while ML-VSe_2 hosts two unidirectional CDWs with $|\mathbf{Q}_1| = 0.25\,\text{rlu}$ and $|\mathbf{Q}_2| = 0.36\,\text{rlu}$ (green and magenta circles, respectively).

6.1.2. Temperature Dependence

To further establish the character of CDW(s), we study the evolution of CDW peaks in BL- and ML-VSe_2 with temperature. Notably, the FT of ML-VSe_2 recorded at higher temperatures (Figure 6.3e) reveal only a single modulation with magnitude $\mathbf{Q}_2$, as well as its harmonics and reflections. This further evidences the presence of only two principal CDWs – $\mathbf{Q}_1$ and $\mathbf{Q}_2$ – and suggests that they may have independent origins. At the same time, the slight thermal variation in the direction of $\mathbf{Q}_2$ with respect to the lattice shows that the $\mathbf{Q}_2$ CDW is not strongly coupled to the lattice. It also suggests a potential interplay between the two CDWs, which may lower the energetic cost of the charge ordered state when harmonics and reflections of $\mathbf{Q}_2$ are connected by $\mathbf{Q}_1$ (Figure 6.3f).

The thermal evolution of the CDW intensity in STM topographs is an established thermodynamic marker of the CDW transition [203, 229]. In Figure 6.5, we show representative STM topographs for ML-VSe2 on HOPG for different temperatures. While the data were recorded over varying fields-of-view, we emphasize that, within our experiments, none of the CDWs exhibit any macroscopic spatial variation across atomically smooth regions. For ease of comparison, the CDW peak intensities plotted in Figure 6.5 are normalised to the corresponding Bragg peak intensities for each STM topograph. Consistently across BL- and ML-VSe_2, we find that the intensity of $\mathbf{Q}_1$ ($4a$ CDW) drops sharply at $\sim 110\,\text{K}$ to a negligible magnitude, consistent with the thermal evolution of its bulk counterpart [122]. The small, finite magnitude of $\mathbf{Q}_1$ in BL-VSe_2 at higher temperatures likely arises from small CDW pockets near defects, similar to defect-pinned CDWs at $T \gg T_{\text{CDW}}$ reported in other

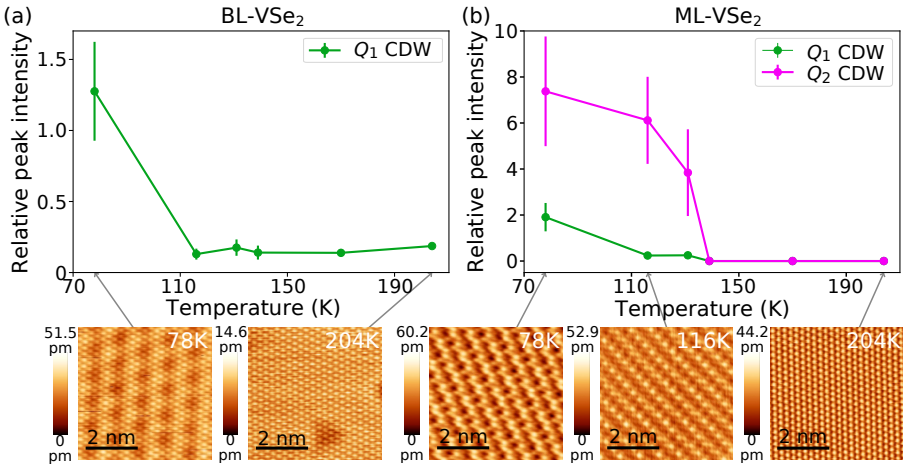

Figure 6.5: Thermal evolution of intensities of the CDW peaks, normalised to the averaged intensities of the six primary Bragg peaks at that temperature, as measured from FTs of $10 \times 10\,\mathrm{nm}^2$ STM topographs acquired on (a) BL- and (b) ML-VSe_2. Error bars show the standard deviation, incorporating the variance in Bragg and CDW peak intensities at each temperature. The bottom row shows STM topographs at selected temperatures for BL (left) and ML (right).

6

TMDCs [203, 229]. Meanwhile, for ML-VSe_2, the intensity of $\mathbf{Q}_2$ – in sharp contrast to $\mathbf{Q}_1$ – remains sizable well above $\sim 110\,\mathrm{K}$, and drops to nearly zero at $\sim 140\,\mathrm{K}$. Finally, no CDW signatures are observed in the 204 K topographs (Figure 6.5c,g), precluding the persistence of either CDW to room temperature [222].

Overall, our systematic analysis sheds much-needed light on the presence, character, and robustness of charge order in ML-VSe_2 in view of conflicting reports in literature [188, 198, 222, 230, 231]. First, our AFM-STM comparison confirms the purely electronic (CDW) origin of all observed superstructures on ML- and BL-VSe_2 (*cf.* ref. [222]). Second, T-dependent experiments conclusively establish the presence of two, and only two, independent single-Q CDWs in ML-VSe_2: $\mathbf{Q}_1 \simeq 0.25\mathbf{a}^*$ (*i.e.* $\lambda_1 \simeq 4a$) and $|\mathbf{Q}_2| \simeq 0.36\,\mathrm{rlu}$ (*i.e.* $\lambda_2 \simeq 2.8a$). The $\mathbf{Q}_1$ CDW is identical in magnitude, orientation, and transition temperature to the triple-Q CDW observed in BL-VSe_2, and to (the in-plane projection of) the CDW reported in bulk crystals. Meanwhile, the $\mathbf{Q}_2$ CDW persists at temperatures well beyond $\mathbf{Q}_1$ and exhibits thermal variations in its orientation with respect to the atomic lattice. Finally, the observed consistency of $\mathbf{Q}_1$ and $\mathbf{Q}_2$ across distinct substrates (*cf.* ref. [230, 231]), and of BL-VSe_2 with the bulk material (*cf.* ref. [198]), strongly constrains the potential influence of substrate-induced strain effects on the CDW characteristics reported here. To understand the origin of this observed dichotomy in CDW characteristics within the same material, we conduct a detailed examination of the electronic structure of ultrathin VSe_2.

6.2. Theoretical Results

6.2.1. Band Structure Calculations

To investigate the atomic and electronic structure of ultrathin 1T-VSe_2, density functional theory (DFT) calculations were performed by Surabhi Saha and Tanmoy Das (Indian Institute of Science, Bangalore, India) using the Vienna *Ab initio* Simulation Package (VASP) [232] with a plane-wave basis up to a cut-off of 500 eV. The Perdew-Burke-Ernzerhof (PBE) [233] form was used for the exchange-correlation functional. The Γ-centred **k**-mesh was set to $25 \times 25 \times 1$ points in the Brillouin zone for the self-consistent calculation. To simulate the monolayer, we artificially set the distance between two layers of VSe_2 to 25 Å. Then, the atomic positions in a 4×4 supercell structure were allowed to relax, both with and without the symmetry constraints of the underlying $P\bar{3}m1$ space group [234]. In both cases, the resulting lattice is purely hexagonal, and free of any structural distortions. This further points to the electronic origin of superstructures observed in ML-VSe_2, in line with our experimental findings. Subsequently, the electronic band structure was computed, both with and without including spin polarization. The resulting energies are nearly equal for both cases. This suggests, in conjunction with the absence of spin splitting in angle-resolved photoemission spectroscopy (ARPES) results [188, 222, 224, 225, 235–237], that magnetic order, even if present in ML-VSe_2, is unlikely to play a significant role in the energetics of charge ordered states.

The DFT band structure (Figure 6.6a) is broadly in agreement with the ARPES spectral function reported in ref. [235]. This data provides a valuable benchmark given its high quality, large momentum range, and qualitative agreement with other ARPES reports, including data acquired on our samples (reported in ref. [224]). Both techniques find a single band of predominantly d-orbital character crossing the Fermi energy E_F. Previous works have emphasised the importance of the nesting of the sides of the FS lobes at the BZ edge [188, 222, 238]. The DFT electronic structure, however, underestimates $\mathbf{k}_F$ along $\mathrm{M} - \mathrm{K}$ and suggests a 'nesting vector' along $\mathbf{a}^*$ of length 0.21 rlu. This falls short of the vector extracted from ARPES data ($0.54 \pm 0.04\,\text{Å}^{-1}$), which corresponds to 0.25 ± 0.02 rlu [225, 235]. The DFT band along $\Gamma - \mathrm{M}$ also appears more dispersive than that in ARPES, while along $\Gamma - \mathrm{K}$ the DFT band is higher (50-200 meV) than the magnitude expected from the high photoelectron count around Γ [188, 222, 224, 225, 235, 236]. These discrepancies are likely due to the inability to duly account for electronic correlations [237]. As a result, our *ab initio* calculations may not capture the electronic structure near E_F with sufficient quantitative accuracy to describe CDW energetics.

We therefore complement the DFT calculation with a tight-binding (TB) fit to the ARPES data in ref. [235]. To obtain this fit, we used an expansion of the dispersion $\epsilon_{\mathbf{k}}$ in functions respecting the lattice symmetries. Including

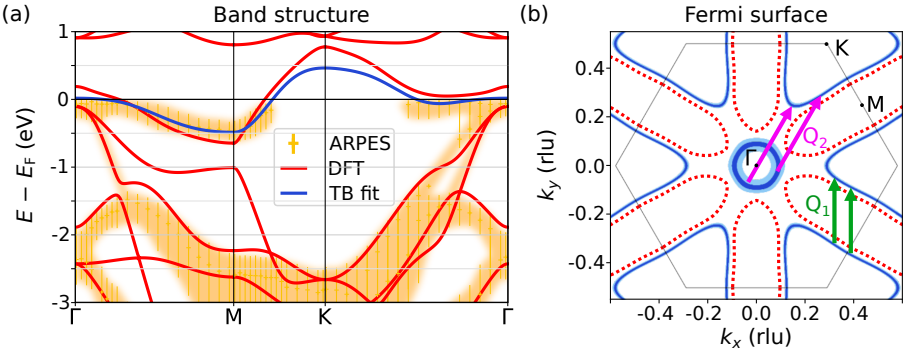

Figure 6.6: (a) Electronic band structure of ML-VSe_2 obtained from DFT calculations (red line), compared to published ARPES measurements of the spectral function for epitaxially grown ML-VSe_2 at $T = 170\,\mathrm{K}$ (shaded yellow, crosses: peak positions, lines: full width at half maximum). The linewidth of the experimental data greatly exceeds the experimental resolution [235]. Blue line is a tight-binding (TB) fit to the ARPES-measured, near-E_F band structure, where E_F is the Fermi energy. (b) Fermi surface (FS) of ML-VSe_2, obtained from the TB fit in (a) by plotting states within $\pm 1\,\mathrm{meV}$ (dark blue) and $\pm 10\,\mathrm{meV}$ ($\approx k_b T$ for $T = 100\,\mathrm{K}$, light blue) of E_F. Dotted red line shows the DFT FS, which qualitatively deviates from the TB fit. Hexagon shows the Brillouin zone, and the arrows indicate FS regions visually appearing to be nested by the experimentally determined CDW wavevectors.

terms to fifth order, the fit can be expressed as:

$$\begin{aligned}\epsilon_{\mathbf{k}} = t_0 &+ t_1\Big(2\cos(\xi)\cos(\eta) + \cos(2\xi)\Big)\\ &+ t_2\big(2\cos(3\xi)\cos(\eta) + \cos(2\eta)\big)\\ &+ t_3\big(2\cos(2\xi)\cos(2\eta) + \cos(4\xi)\big)\\ &+ t_4\big(\cos(\xi)\cos(3\eta) + \cos(5\xi)\cos(\eta) + \cos(4\xi)\cos(2\eta)\big)\\ &+ t_5\big(2\cos(3\xi)\cos(3\eta) + \cos(6\xi)\big),\end{aligned} \tag{6.1}$$

where $\xi = k_x/2$ and $\eta = \sqrt{3}k_y/2$, and k_x, k_y are given in units of $2\pi/a$, with a the lattice parameter. t_i are the (in-plane) hopping amplitudes. This expression was fitted using a least-squares fit procedure to the peak positions of the ARPES spectrum of ML-VSe_2 on bilayer graphene reported in ref. [235]. The resulting best fit is shown in 6.6. In agreement with reported ARPES spectra, the TB fit shows a flat band region around the Γ-point, an indicator of strong correlations.[3] The difference in topology between the DFT and TB FS (Figure 6.6b) is due to the proximity of a van Hove singularity to E_F [235]. Overlaying the CDW vectors extracted from our STM data onto the FS visually suggests that $\mathbf{Q}_1$ corresponds to nesting between the sides of neighbouring

[3] An intuitive argument for this is that a flat band describes electrons with a small group velocity (given by the slope of the band). When the kinetic energy of electrons is reduced, we can expect other interactions to become more dominant.

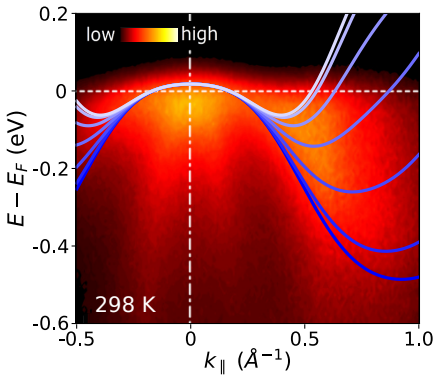

Figure 6.7: The TB fit overlaid on an azimuthally averaged ARPES spectrum acquired on an ultrathin VSe_2 sample grown on HOPG, reported previously [224]. The sample is from the same batch as that used for the STM measurements reported in the present chapter. Curves show TB fits for a sequence of **k**-directions in steps of 10°, from along $\Gamma - M$ (dark blue) to $\Gamma - K$ (white).

triangular FS pockets at the BZ edge, while $\mathbf{Q}_2$ connects the flat-band region around Γ to the pocket corners around K.

To ensure that the fitted spectrum is also consistent with the samples used in the present study, we compare our tight-binding fit to the ARPES spectrum of a sample from the same batch of ML-VSe_2 grown on HOPG, previously reported in ref. [224]. As the macroscopic photon beam used in these experiments averages over ML-VSe_2 grains of multiple orientations, the resulting spectrum corresponds to an azimuthal average over reciprocal space. While this limits a direct experimental determination of the **k**-resolved Fermi surface for the samples studied by STM, we can still compare the tight-binding fit band structure with the azimuthally averaged ARPES data. To account for the azimuthal averaging, we plot the tight-binding spectrum (Figure 6.7) for a sequence of different **k**-directions, rotated 10° from one another, lying along $\Gamma - M$ (dark blue) to $\Gamma - K$ (white). We find a good agreement between the two.

6.2.2. Nesting and Correlated Instabilities

As already discussed at length in the previous two chapters, a conventional CDW instability at wavevector $\mathbf{Q}_{\mathrm{CDW}}$ results from a maximum in its structured electronic susceptibility $D_2(\mathbf{q})$ for $\mathbf{q} = \mathbf{Q}_{\mathrm{CDW}}$ [164, 179]. In the weak electron-phonon coupling (EPC) limit, $D_2(\mathbf{q})$ is given by:

$$D_2(\mathbf{q}) = -\sum_{\mathbf{k}\in \mathrm{BZ}} |g_{\mathbf{k},\mathbf{k}+\mathbf{q}}|^2 \frac{f(\epsilon_{\mathbf{k}}) - f(\epsilon_{\mathbf{k}+\mathbf{q}})}{\epsilon_{\mathbf{k}} - \epsilon_{\mathbf{k}+\mathbf{q}} + i\delta}. \tag{6.2}$$

As before, $f(\epsilon)$ is the Fermi-Dirac function, $\epsilon_{\mathbf{k}}$ is the bare electronic dispersion (given by the TB model), and δ is a small regulator that we set to 0.1 meV in this work. For the EPC matrix elements, $g_{\mathbf{k},\mathbf{k}+\mathbf{q}}$, we again use the approximation

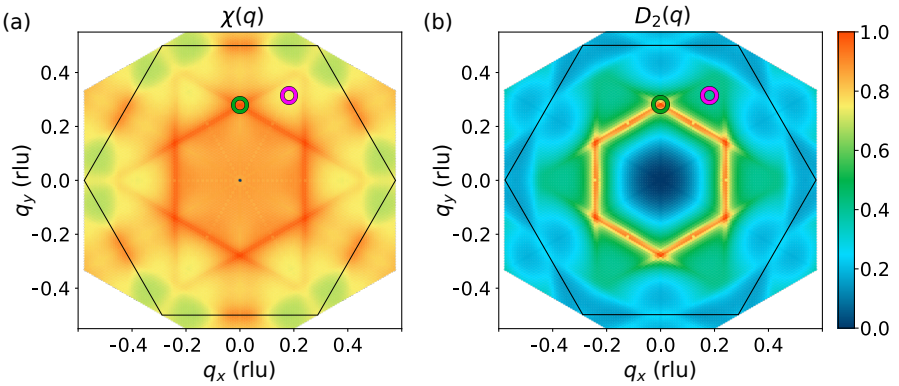

Figure 6.8: (a) The normalised Lindhard susceptibility χ and (b) structured electronic susceptibility D_2 of ML-VSe_2, derived from the TB band structure. Circles highlight the positions of the susceptibility maximum $(0, 0.28) \approx \mathbf{Q}_1$ (green) and experimentally determined $\mathbf{Q}_2 = (0.182, 0.315)$ (magenta), with the latter being located on an intensity plateau.

of Varma *et al.* [166], seen in earlier chapters. If we instead set $g_{\mathbf{k},\mathbf{k+q}} = 1$, we obtain the Lindhard function $\chi(\mathbf{q})$.

The green circle in Figure 6.8a(b) indicates the maximum of the bare (structured) susceptibility, which lies at $\mathbf{Q} = (0, 0.28) \approx \mathbf{Q}_1$. Its proximity to a commensurate value suggests that the corresponding CDW will lock to 0.25 rlu ($\lambda_1 = 4a$) due to CDW-lattice interactions [200]. Although its periodicity is the same as that of the CDW observed in bulk and BL-VSe_2, the FS for the ML is strictly 2D, and the parts of the FS involved in CDW formation may be different.

To elucidate the role of the FS in the observed CDWs, we plot in Figure 6.9 the $\mathbf{k}$-resolved contributions to $\chi(\mathbf{q})$ and $D_2(\mathbf{q})$ for $\mathbf{q} = \mathbf{Q}_1$ and $\mathbf{Q}_2$. To compute this, we define

$$D_2(\mathbf{k}, \mathbf{Q}) = -|g_{\mathbf{k},\mathbf{k+Q}}|^2 \frac{f(\epsilon_{\mathbf{k}}) - f(\epsilon_{\mathbf{k+Q}})}{\epsilon_{\mathbf{k}} - \epsilon_{\mathbf{k+Q}} + i\delta}, \tag{6.3}$$

and similarly for $\chi(\mathbf{k}, \mathbf{Q})$. Notice that we simply removed the sum over $\mathbf{k}$, and are computing what the contribution to the susceptibility is of a specific wavevector $\mathbf{Q}$. Regions of intensity in such a diagnostic indicate which regions of the BZ contribute to the susceptibility, *i.e.* which electronic states can be scattered by the chosen wavevector $\mathbf{Q}$. As anticipated in Figure 6.6b, the dominant contributions to $\chi(\mathbf{Q}_1)$ arise from the parallel edges of the K-centred pockets, while the Γ-centred FS region plays a negligible role. The well-nested K-pocket edges with opposite group velocities are therefore inherently unstable to a Peierls-like CDW. The EPC matrix elements further enhance the contribution of these $\mathbf{Q}_1$-connected regions to $D_2(\mathbf{Q}_1)$, thereby confirming the conventional origin of the $\mathbf{Q}_1$ CDW in ML-VSe_2.

In contrast, the phenomenology for $\mathbf{q} = \mathbf{Q}_2$ does not fit the conventional

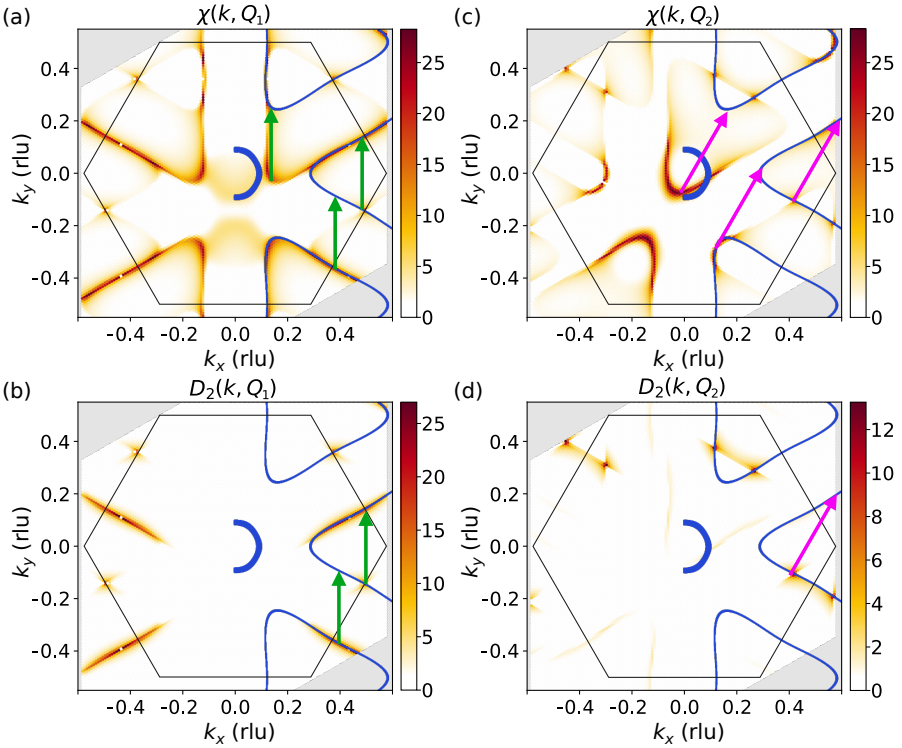

Figure 6.9: Momentum space diagnostics of ML-VSe_2 CDWs, indicating the BZ regions contributing to the two susceptibilities χ and D_2, given a chosen wavevector $\mathbf{Q}_1$ (a,b) or $\mathbf{Q}_2$ (c,d). Blue lines denote FS contours in the right half of the images, while black hexagons indicate the BZ. $\mathbf{Q}_1$ (green) and $\mathbf{Q}_2$ (magenta) arrows indicate the regions with prominent contributions to the susceptibilities as deduced from the diagnostics.

CDW framework. As highlighted by the magenta circles in Figure 6.8, this wavevector lies in the middle of a susceptibility plateau, and lacks a well-defined maximum. The dominant contribution to the bare susceptibility at $\mathbf{q} = \mathbf{Q}_2$ comes from the Γ-centered flat band region, with smaller contributions from the K-centred pockets (see Figure 6.9c). However, the corresponding $D_2(\mathbf{k}, \mathbf{Q}_2)$ in Figure 6.9d shows that the EPC matrix elements strongly suppress the intensity in these regions, and the remaining contributions are insufficient to drive the $\mathbf{Q}_2$ CDW according to an EPC-assisted Peierls scenario. While the perturbative expansion used for the structured susceptibility calculations [2, 159, 164, 166] may not fully capture EPC in flat bands, that the origin of the $\mathbf{Q}_2$ CDW lies beyond the Peierls description of CDWs is consistent with its empirical characteristics: its varying orientation with respect to the lattice, absence in BLs (and beyond), and the lack of a discernible peak in $\chi(\mathbf{q})$.

In the 2D limit of layered TMDCs like 1T-VSe_2, the screening of Coulomb interactions between electrons is much reduced [239]. The relative importance

of the unscreened interactions is further enhanced within flat bands associated with a van Hove singularity, such as at the near-Γ region in ML-VSe_2 (Figure 6.6) [222, 235–237]. Indeed, the measured linewidth, or self-energy, of the band near E_F is much larger than the experimental resolution [235], supporting the presence of strong electronic correlations [169]. Such interactions can considerably renormalise electron and phonon properties, and enable CDW order at momenta that do not correspond to peaks in the conventional susceptibility ($\chi(\mathbf{q})$ or $D_2(\mathbf{q})$). Indeed, such correlation-driven CDWs have been predicted to exist in TMDCs [210], including in ML-VSe_2 [238], and are consistent with the unusual characteristics of the $\mathbf{Q}_2$ CDW. Crucially, a correlation-driven mechanism for the $\mathbf{Q}_2$ CDW offers the only viable explanation of its prevalence over a well-nested counterpart ($\mathbf{Q}_1$), and the complete gapping of the FS [222, 235–237], despite the absence of any associated feature in susceptibility calculations based on models of non-interacting electrons. Further, we conjecture that the single-Q character of the $\mathbf{Q}_2$ CDW, which breaks the three-fold rotational symmetry of the lattice, makes it energetically favourable for the $\mathbf{Q}_1$ CDW (nominally triple-Q) to also order in a single-Q configuration. The interplay of these CDWs could be examined in future theoretical works by iteratively incorporating the resulting lattice distortions.

6.3. Discussion and conclusion

In summary, our systematic experimental and theoretical efforts elucidate that 1T-VSe_2 undergoes a dimensional crossover as its thickness is reduced to a single layer. While BL-VSe_2, akin to bulk, hosts a conventional triple-Q CDW, ML-VSe_2 hosts two distinct single-Q CDWs with contrasting characteristics. One, with $\lambda_1 \simeq 4a$, behaves similarly to its BL/bulk counterpart, and arises from a weak-coupling Peierls-like mechanism utilising nested FS regions. In contrast, the dominant CDW, with $\lambda_2 \simeq 2.8\,a$, cannot be explained within the conventional EPC-assisted Peierls framework. Instead, the observed thermal evolution and the calculated susceptibility suggest that this CDW – unique to the ML – arises from a flat region of the electronic band structure, where interactions and correlation effects are expected to dominate.

Monolayer VSe_2 stands apart in hosting two coexisting charge orders with distinct physical origins. Conventional electronic materials are typecast by the mechanisms and phenomena they host. Our work suggests that ML-VSe_2 transcends such labelling, and hosts coexisting ordered states originating from contrasting coupling mechanisms. The prospect of such emergent electron correlations and ensuing ordered states presenting themselves in 2D TMDCs more generally is particularly promising given their predominance in the plethora of proposed designs for heterogeneous layered materials [212, 240, 241]. Their potential for tunability and their interplay with conventional charge and spin orders in the ultrathin limit is promising for realising exotic ordered states on the one hand, and for applications in multifunctional electronics on the other.

With this, we also conclude Part II of this thesis. We have now seen how electrons, coupled to the lattice they live in, may form charge-ordered states that change the symmetry and other properties of their host material. The limitations of the conventional description of CDWs by analogy to the Peierls model has historically complicated the discussion in the literature, by encouraging the creation of distinct mechanisms and models to explain apparent 'unconventional' (by which we mean non-Peierls-like) features of CDWs in real materials. By describing the effects of electron-phonon coupling in a general framework that allows for the inclusion of a structured EPC (as well as strong-coupling extensions [159]), it becomes much easier to determine whether charge order in specific materials should be deemed unusual, or not. In the case of bulk VSe_2, we demonstrated that all the apparently unconventional features are well-described by a theory with weak, structured EPC. Conversely, in ML-VSe_2 this same framework was able to demonstrate that one of the two CDWs it hosts is decidedly unusual, and requires additional coupling mechanisms beyond EPC.

As demonstrated by Part II of this thesis, it has taken a concerted effort to understand the subtleties behind the formation of CDWs, even when restricting ourselves to only considering electron-phonon interactions. Now that we understand EPC-driven charge order, we should turn to the unknown. There are many systems which, like ML-VSe_2, host multiple types of interactions. Many also host multiple order parameters – be it electronic, magnetic, structural, superconducting, or otherwise – which may compete or complement each other. The need to take into account multiple types of interactions and phases is precisely what makes exotic beasts like cuprates, pnictides, complex oxides and (multi)ferroics so interesting.

In the grand scheme of things, it will always remain impossible to take into account, well, everything. In some cases, we might need to let go of the entire concept of quasiparticles and the starting point of hypothetical non-interacting quantum fields, and start using entirely new frameworks like holography [242]. In many other cases, however, we should be able to make significant progress by pushing the limits of (often already existing) methods. Note that Doran already demonstrated the need for considering a structured EPC to describe the charge order in $NbSe_2$ back in 1978 [164]. Now, 44 years later, having demonstrated that by including a structured EPC we can obtain quantitative agreement with experiments on real CDW materials, we appear to finally have reached the point that this might become more standard practice. With today's computational power, we should be able to reconsider many other standardised – but ultimately unphysical – approximations in the theories we use. With a bit of luck, this will further our understanding of exotic phases of matter; and where it fails, we might learn what we're missing.

A

Appendix

A.1. Multiband CDW Hamiltonians

In Section 4.2, we plot several electronic band structures within possible CDW phases of the models considered. These are derived by considering the lattice distortion generated by the CDW, and then defining a new tight-binding model with a larger unit cell and modified hopping parameters. Let us demonstrate how this works with the system of two coupled Peierls chains (see Figure 4.3). In the normal phase, this has Hamiltonian

$$\begin{aligned} H_{\mathrm{e}} =& \sum_j \Big[\mu_c c_j^\dagger c_j + \mu_d d_j^\dagger d_j - t_1 \left(c_j^\dagger c_{j+1} + c_{j+1}^\dagger c_j + d_j^\dagger d_{j+1} + d_{j+1}^\dagger d_j \right) \\ & - t_2 \left(c_j^\dagger d_j + d_j^\dagger c_j \right) \Big] \\ =& \sum_{\mathbf{k}} \begin{pmatrix} c_k^\dagger & d_k^\dagger \end{pmatrix} \begin{pmatrix} \mu_c - 2t_1 \cos(ka) & -t_2 \\ -t_2 & \mu_d - 2t_1 \cos(ka) \end{pmatrix} \begin{pmatrix} c_k \\ d_k \end{pmatrix}, \end{aligned} \tag{A.1}$$

where we have relabelled $c_{k,1} = c_k$ and $c_{k,2} = d_k$. We set $\mu_c = \mu_d = 0$ and $t_1 = t_2 = 1$. The periodic lattice distortion that we impose consists of an out-of-phase dimerisation in the two chains. This can be described in real space by defining $u_j = \alpha(-1)^j$ and $v_j = -\alpha(-1)^j$, which describe the lateral displacements of the c and d atoms from their original positions, respectively. We take α to be small compared to a; the plots in Figure 4.3 assume an exaggerated $\alpha = 0.1a$. To first order, the t_1-hopping is modified by these displacements because of this addition to the Hamiltonian:

$$-t_1 \sum_j \alpha \left[\Big(u_j - u_{j+1} \Big) \Big(c_j^\dagger c_{j+1} + c_{j+1}^\dagger c_j \Big) + \Big(v_j - v_{j+1} \Big) \Big(d_j^\dagger d_{j+1} + d_{j+1}^\dagger d_j \Big) \right]. \tag{A.2}$$

Overall, this means the t_1 hopping amplitude is modified by a factor $(1 \pm 2\alpha)$. For simplicity, we assume the atoms are allowed to relax their positions perpendicular to the chain direction, in such a way that t_2 remains unchanged.

At this point, we define a new Hamiltonian, which has a unit cell that is twice the size of the original. Let us define new electron operators for the n^{th} unit cell:

$$c_n = c_{2j}; \qquad \tilde{c}_n = c_{2j+1}; \qquad d_n = d_{2j}; \qquad \tilde{d}_n = d_{2j+1}. \tag{A.3}$$

In this basis, the Hamiltonian is given by (setting all on-site potentials μ_ν to zero)

$$\begin{aligned} H_{\text{e}} = \sum_n \Big[& - t_1(1+2\alpha)\left(c_n^\dagger \tilde{c}_n + \tilde{c}_n^\dagger c_n + \tilde{d}_{n+1}^\dagger d_n + d_n^\dagger \tilde{d}_{n+1}\right) \\ & - t_1(1-2\alpha)\left(c_{n+1}^\dagger \tilde{c}_n + \tilde{c}_n^\dagger c_{n+1} + \tilde{d}_n^\dagger d_n + d_n^\dagger \tilde{d}_n\right) \\ & - t_2\left(c_n^\dagger d_n + d_n^\dagger c_n + \tilde{c}_n^\dagger \tilde{d}_n + \tilde{d}_n^\dagger \tilde{c}_n\right)\Big]. \end{aligned} \tag{A.4}$$

Finally, using the Fourier transform $c_n = \sqrt{\frac{2}{N}} \sum_k e^{2ikna} c_k$ (and similarly for the other operators), where k takes $N/2$ values in the range $-\pi/2a$ to $+\pi/2a$, we obtain the Bloch Hamiltonian

$$h_{\text{e}}(k) = \begin{pmatrix} 0 & -\tilde{t} & -t_2 & 0 \\ -\tilde{t}^* & 0 & 0 & -t_2 \\ -t_2 & 0 & 0 & -\tilde{t}^* \\ 0 & -t_2 & -\tilde{t} & 0 \end{pmatrix}, \tag{A.5}$$

written in the basis $|\psi\rangle = (c_k^\dagger, \tilde{c}_k^\dagger, d_k^\dagger, \tilde{d}_k^\dagger)$. We defined $\tilde{t} = t_1(1+2\alpha) + t_1(1-2\alpha)e^{-2iak}$. Diagonalising this matrix gives the eigenvalues shown in the bottom left plot of Figure 4.3.

Adding a third (vertically aligned) Peierls chain has the following CDW Bloch Hamiltonian:

$$h_{\text{e}}(k) = \begin{pmatrix} 0 & -\tilde{t} & -t_2 & 0 & 0 & 0 \\ -\tilde{t}^* & 0 & 0 & -t_2 & 0 & 0 \\ -t_2 & 0 & 0 & -\tilde{t}^* & -t_2 & 0 \\ 0 & -t_2 & -\tilde{t} & 0 & 0 & -t_2 \\ 0 & 0 & -t_2 & 0 & 0 & -\tilde{t} \\ 0 & 0 & 0 & -t_2 & -\tilde{t}^* & 0 \end{pmatrix}, \tag{A.6}$$

which results in the CDW band structure in the bottom right of Figure 4.3.

In the case of the 'diamond-chain' model, we consider periodic lattice distortions in which the atoms move perpendicular to the chain directions. In

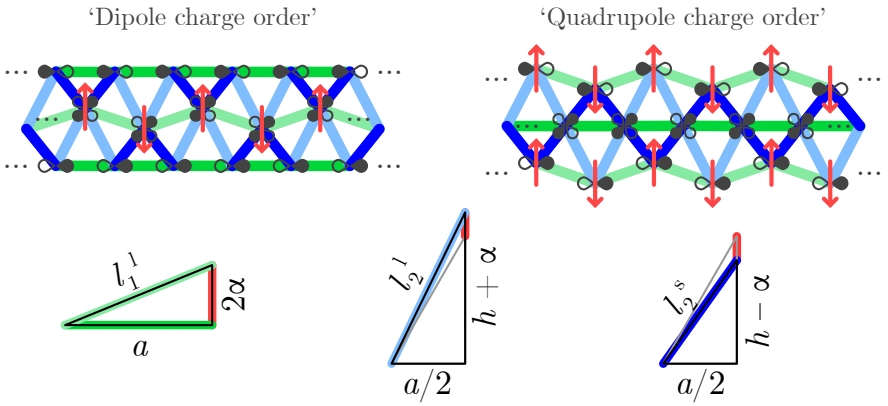

Figure A.1: The two sets of lattice distortions considered in the CDW Ansatzes for the 'diamond-chain' model. At the top, the distorted lattices are shown, with atomic displacements indicated as red arrows, and bonds colour-coded by their length. Dark green bonds have (unchanged) length a; light green bonds are slightly lengthened to l_1^{l}; light blue bonds are stretched to length l_2^{l}, and dark blue bonds are shortened to length l_2^{s}. The triangles in the bottom row indicate how we can determine the new bond lengths using Pythagoras' theorem. $h = \frac{\sqrt{3}}{2}a$.

this case, there are multiple changes to bond lengths which we must consider. As before, we can use the first-order approximation that a small displacement which changes a bond length will linearly affect the hopping parameter for this bond length. All initial bond lengths are set to a, such that the original lattice is made up of equilateral triangles. Vertical displacements thus change the bond lengths in a way that can be determined by trigonometry. Figure A.1 indicates all bond length changes considered in the two CDW Ansatzes demonstrated in Figure 4.4. We can calculate the length of the light green bonds as

$$l_1^{\mathrm{l}} = \sqrt{a^2 + 4\alpha^2} = a\sqrt{1 + \frac{4\alpha^2}{a^2}} \approx a\left(1 + \frac{2\alpha^2}{a^2}\right), \tag{A.7}$$

where in the last step we used $\sqrt{1+x} \approx 1 + x/2$. The length of the light and dark blue bonds is derived as

$$\begin{aligned} l_2^{\mathrm{l}} &= \sqrt{\frac{a^2}{4} + \left(\frac{\sqrt{3}}{2}a + \alpha\right)^2} = a\sqrt{1 + \frac{\sqrt{3}\alpha}{a} + \frac{\alpha^2}{a^2}} \approx a\left(1 + \frac{\sqrt{3}\alpha}{2a} + \frac{\alpha^2}{2a^2}\right); \\ l_2^{\mathrm{s}} &= \sqrt{\frac{a^2}{4} + \left(\frac{\sqrt{3}}{2}a - \alpha\right)^2} = a\sqrt{1 - \frac{\sqrt{3}\alpha}{a} + \frac{\alpha^2}{a^2}} \approx a\left(1 - \frac{\sqrt{3}\alpha}{2a} + \frac{\alpha^2}{2a^2}\right). \end{aligned} \tag{A.8}$$

A

This gives us the new hopping parameters

$$\begin{aligned} t_1^{\mathrm{l}} &= \left(1 - \frac{2\alpha^2}{a^2}\right); \\ t_2^{\mathrm{l}} &= \left(1 - \frac{\sqrt{3}\alpha}{2a} - \frac{\alpha^2}{2a^2}\right); \\ t_2^{\mathrm{s}} &= \left(1 + \frac{\sqrt{3}\alpha}{2a} - \frac{\alpha^2}{2a^2}\right). \end{aligned} \tag{A.9}$$

We then obtain the following Bloch Hamiltonian for the dipole CDW phase:

$$h_{\mathrm{e}}(k) = \begin{pmatrix} 0 & -t_1\gamma & -t_2^{\mathrm{s}} & -t_2^{\mathrm{l}} & 0 & 0 \\ -t_1\gamma^* & 0 & -t_2^{\mathrm{s}}\beta^* & -t_2^{\mathrm{l}} & 0 & 0 \\ -t_2^{\mathrm{s}} & -t_2^{\mathrm{s}}\beta & 0 & -t_1^{\mathrm{l}}\gamma & -t_2^{\mathrm{l}} & -t_2^{\mathrm{l}}\beta \\ -t_2^{\mathrm{l}} & -t_2^{\mathrm{l}} & -t_1^{\mathrm{l}}\gamma^* & 0 & -t_2^{\mathrm{s}} & -t_2^{\mathrm{s}} \\ 0 & 0 & -t_2^{\mathrm{l}} & -t_2^{\mathrm{s}} & 0 & -t_1\gamma \\ 0 & 0 & -t_2^{\mathrm{l}}\beta^* & -t_2^{\mathrm{s}} & -t_1\gamma^* & 0 \end{pmatrix}, \tag{A.10}$$

where we defined $\beta = e^{-2ika}$ and $\gamma = 1 + e^{-2ika}$. Finally, for the quadrupole CDW phase we obtain the Bloch Hamiltonian

$$h_{\mathrm{e}}(k) = \begin{pmatrix} 0 & -t_1^{\mathrm{l}}\gamma & -t_2^{\mathrm{s}} & -t_2^{\mathrm{s}} & 0 & 0 \\ -t_1^{\mathrm{l}}\gamma^* & 0 & -t_2^{\mathrm{l}}\beta^* & -t_2^{\mathrm{l}} & 0 & 0 \\ -t_2^{\mathrm{s}} & -t_2^{\mathrm{l}}\beta & 0 & -t_1\gamma & -t_2^{\mathrm{s}} & -t_2^{\mathrm{l}} \\ -t_2^{\mathrm{s}} & -t_2^{\mathrm{l}} & -t_1\gamma^* & 0 & -t_2^{\mathrm{s}}\beta^* & -t_2^{\mathrm{l}} \\ 0 & 0 & -t_2^{\mathrm{s}} & -t_2^{\mathrm{s}}\beta & 0 & -t_1^{\mathrm{l}}\gamma \\ 0 & 0 & -t_2^{\mathrm{l}} & -t_2^{\mathrm{l}} & -t_1^{\mathrm{l}}\gamma^* & 0 \end{pmatrix}. \tag{A.11}$$

A.2. Matsubara sum: electronic susceptibility

In this section, we perform the Matsubara summation in $D_2(\mathbf{q}, \Omega)$ and $\chi(\mathbf{q}, \Omega)$, to obtain Equations 4.37 and 4.38. The relevant summation in both cases is

$$\sum_{\omega_n} G_k G_{k+q} = \sum_{\omega_n} \frac{1}{i\omega_n - \epsilon_{\mathbf{k}}} \frac{1}{i\omega_n - \epsilon_{\mathbf{k}+\mathbf{q}} + i\Omega_n}, \tag{A.12}$$

where I omitted the band labels and absorbed the chemical potential μ into $\epsilon_{\mathbf{k}}$. The following describes the standard method for computing such summations; see for instance refs. [161, 162].

The fermionic Matsubara frequencies in Equation A.12 constitute an infinite set, defined by $\omega_n = (2n+1)\pi/\beta$ with $n \in \mathbb{Z}$. (The bosonic Matsubara frequencies are given by $\Omega_n = 2n\pi/\beta$.) To compute the sum over ω_n, we use Cauchy's theorem. This theorem equates the infinite sum over a function of

discrete frequencies to a contour integral in the complex plane over a weight function with poles at the same frequencies. For fermions, a convenient choice for this weight function is the Fermi-Dirac distribution function

$$f(z) = \frac{1}{e^{\beta z} + 1}. \tag{A.13}$$

Explicitly, a generic sum over fermionic Matsubara frequencies can be rewritten as

$$\sum_{\omega_n} h(i\omega_n) = \frac{1}{2\pi i} \oint_{\mathcal{C}} dz\, h(z) f(z). \tag{A.14}$$

In this expression, we can identify $h(i\omega_n) = G_k G_{k+q}$:

$$\sum_{\omega_n} G_k G_{k+q} = \frac{1}{2\pi i} \oint_{\mathcal{C}} dz\, \frac{1}{z - \epsilon_{\mathbf{k}}}\, \frac{f(z)}{z - \epsilon_{\mathbf{k+q}} + i\Omega_n}. \tag{A.15}$$

A convenient feature of contour integrals in the complex plane is that the outcome of the integral over a closed contour is equal to the sum of the residues of the poles enclosed by that contour. This is known as the residue theorem. The integrand in the above expression has the infinite set of poles in $f(z)$, which are enclosed by the contour $\mathcal{C}$, as well as two simple poles at $z_1 = \epsilon_{\mathbf{k+q}} - i\Omega_n$ and $z_2 = \epsilon_{\mathbf{k}}$, respectively. By the residue theorem, we know that we can deform the contour without changing the outcome of the contour integral, so long as the deformed contour does not enclose the two other poles at z_1 and z_2. Additionally, since $h(z)f(z) \to 0$ faster than $1/|z| \to 0$ as we take $|z| \to \infty$ in all directions in the complex plane, any line integral lying *at* infinity will give zero, regardless of how many poles it encloses. As is sketched in Figure A.2, we can equate the integral over the anti-clockwise[1] contour $\mathcal{C}$ enclosing all poles at Matsubara frequencies $z = i\omega_n$ with an integral over two clockwise contours $\gamma_{1,2}$ surrounding the poles at $z_{1,2}$, plus an anti-clockwise contour lying at infinity (which necessarily gives zero). And, by the residue theorem, this means that

$$\sum_{\omega_n} G_k G_{k+q} = -\sum_j \mathrm{Res}\left[\frac{f(z)}{z - \epsilon_{\mathbf{k}}}\, \frac{1}{z - \epsilon_{\mathbf{k+q}} + i\Omega_n}\right]_{z=z_j}. \tag{A.16}$$

Finally, the residues of the simple poles at z_j are given by $\left[(z - z_j)h(z)f(z)\right]_{z=z_j}$, such that we obtain

$$\begin{aligned} \sum_{\omega_n} G_k G_{k+q} &= -\frac{f(\epsilon_{\mathbf{k}})}{\epsilon_{\mathbf{k}} - \epsilon_{\mathbf{k+q}} + i\Omega_n} - \frac{f(\epsilon_{\mathbf{k+q}} - i\Omega_n)}{\epsilon_{\mathbf{k+q}} - i\Omega_n - \epsilon_{\mathbf{k}}} \\ &= -\frac{f(\epsilon_{\mathbf{k}}) - f(\epsilon_{\mathbf{k+q}})}{\epsilon_{\mathbf{k}} - \epsilon_{\mathbf{k+q}} + i\Omega_n}. \end{aligned} \tag{A.17}$$

[1] The direction in which the contour is integrated over is important, because changing from anti-clockwise to clockwise gives a minus sign.

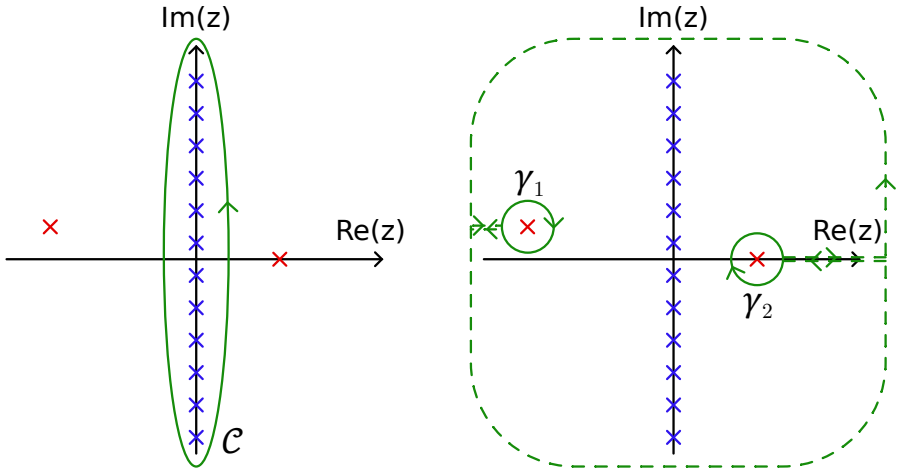

Figure A.2: The sum over electronic Matsubara frequencies ω_n can be calculated as a line integral in the complex plane of a function $(h(z)f(z))$ containing simple poles at $z = i\omega_n$ (blue crosses) over the anti-clockwise contour $\mathcal{C}$ (which stretches to $\mathrm{Im}(z) \to \pm\infty$), shown on the left. As shown on the right, we can deform this contour into two clockwise contours surrounding the poles of $h(z) = G_k G_{k+q}$: γ_1 surrounding $z_1 = \epsilon_{\mathbf{k+q}} - i\Omega_n$ and γ_2 surrounding $z_2 = \epsilon_{\mathbf{k}}$. The integrals along the dashed lines all give zero.

In the last line, we used that $f(\epsilon - i\Omega_n) = f(\epsilon - 2\pi i n/\beta) = f(\epsilon)$. Thus, we conclude that

$$D_2^{\lambda,\nu,\eta}(\mathbf{q},\Omega) = \sum_k |g^{\lambda,\nu,\eta}_{\mathbf{k},\mathbf{k+q}}|^2 G_k^\lambda G_{k+q}^\nu = -\sum_{\mathbf{k}} |g^{\lambda,\nu,\eta}_{\mathbf{k},\mathbf{k+q}}|^2 \frac{f(\epsilon^\lambda_{\mathbf{k}}) - f(\epsilon^\nu_{\mathbf{k+q}})}{\epsilon^\lambda_{\mathbf{k}} - \epsilon^\nu_{\mathbf{k+q}} + i\Omega}; \tag{A.18}$$

$$\chi^{\lambda,\nu}(\mathbf{q},\Omega) = \sum_k G_k^\lambda G_{k+q}^\nu = -\sum_{\mathbf{k}} \frac{f(\epsilon^\lambda_{\mathbf{k}}) - f(\epsilon^\nu_{\mathbf{k+q}})}{\epsilon^\lambda_{\mathbf{k}} - \epsilon^\nu_{\mathbf{k+q}} + i\Omega}. \tag{A.19}$$

A.3. Matsubara sum: electronic self-energy

In this section, we perform the Matsubara summation over bosonic frequencies $\Omega_n = 2n\pi/\beta$ to obtain an expression for the electronic self-energy. For simplicity, we consider only interactions via bare phonon fields here, although the same method can be applied using renormalised phonons, as demonstrated in *e.g.* ref. [162]. The electronic self-energy is given by

$$\Sigma_k = \Sigma(\mathbf{k}, i\omega_n) = \sum_{\mathbf{q}} \sum_{\Omega_n} \Big(|g_{\mathbf{k},\mathbf{k-q}}|^2 D(\mathbf{q}, i\Omega_n) G(\mathbf{k}-\mathbf{q}, i\omega_n - i\Omega_n \Big). \tag{A.20}$$

Writing out the bare phonon propagator D, and expressing the electron propagator in the Lehmann representation, we obtain

$$\Sigma(\mathbf{k}, i\omega_n) = -\frac{1}{\pi}\sum_{\mathbf{q}}\left(|g_{\mathbf{k},\mathbf{k}-\mathbf{q}}|^2\int d\epsilon' \,\mathrm{Im}\,[G(\mathbf{k}-\mathbf{q},\epsilon'] \times \sum_{\Omega_n}\left(\frac{-2\Omega_{\mathbf{q}}}{(i\Omega_n)^2-\Omega_{\mathbf{q}}^2}\frac{1}{i\omega_n - i\Omega_n - \epsilon'}\right)\right). \tag{A.21}$$

We can perform the Matsubara sum on the second line by rewriting it as a contour integral

$$\sum_{\Omega_n} h(i\Omega_n) = \frac{1}{2\pi i}\oint dz\, n_{\mathrm{B}}(z)h(z), \tag{A.22}$$

where $h(i\Omega_n)$ is the function in the parentheses on the second line of Equation A.21, and

$$n_{\mathrm{B}}(z) = \frac{1}{e^{\beta z}-1} \tag{A.23}$$

is the Bose-Einstein distribution function. We note that $n_{\mathrm{B}}(z)$ has simple poles at $i\Omega_n$, while $h(z)$ has three poles lying at $z_1 = \Omega_{\mathbf{q}}$, $z_2 = -\Omega_{\mathbf{q}}$ and $z_3 = i\omega_n - \epsilon'$. As such, we can replace the contour integral by the sum over residues of the poles enclosed:

$$\begin{aligned}\sum_{\Omega_n} h(i\Omega_n) &= -\sum_j \mathrm{Res}\left[n_{\mathrm{B}}(z)h(z)\right]_{z=z_j}\\ &= \frac{n_{\mathrm{B}}(\Omega_{\mathbf{q}})}{i\omega_n - \epsilon' - \Omega_{\mathbf{q}}} - \frac{n_{\mathrm{B}}(-\Omega_{\mathbf{q}})}{i\omega_n - \epsilon' + \Omega_{\mathbf{q}}}\\ &\quad - \frac{2\Omega_{\mathbf{q}} n_{\mathrm{B}}(i\omega_n - \epsilon')}{(i\omega_n - \epsilon' - \Omega_{\mathbf{q}})(i\omega_n - \epsilon' + \Omega_{\mathbf{q}})}.\end{aligned} \tag{A.24}$$

Using the properties $n_{\mathrm{B}}(-\Omega_{\mathbf{q}}) = -n_{\mathrm{B}}(\Omega_{\mathbf{q}}) - 1$ and $n_{\mathrm{B}}(i\omega_n - \epsilon') = -f(-\epsilon') = f(\epsilon') - 1$, we can rewrite this as

$$\sum_{\Omega_n} h(i\Omega_n) = \frac{n_{\mathrm{B}}(\Omega_{\mathbf{q}}) - f(\epsilon') + 1}{i\omega_n - \epsilon' - \Omega_{\mathbf{q}}} + \frac{n_{\mathrm{B}}(\Omega_{\mathbf{q}}) + f(\epsilon')}{i\omega_n - \epsilon' + \Omega_{\mathbf{q}}} \tag{A.25}$$

Finally, we Wick rotate $i\omega_n \to \epsilon + i\delta$, and fill it back into Equation A.21 to obtain

$$\Sigma(\mathbf{k}, \epsilon + i\delta) = -\frac{1}{\pi}\sum_{\mathbf{q}}\left(|g_{\mathbf{k},\mathbf{k}-\mathbf{q}}|^2\int d\epsilon' \,\mathrm{Im}\,[G(\mathbf{k}-\mathbf{q},\epsilon')] \times \left(\frac{n_{\mathrm{B}}(\Omega_{\mathbf{q}}) - f(\epsilon') + 1}{\epsilon - \epsilon' - \Omega_{\mathbf{q}} + i\delta} + \frac{n_{\mathrm{B}}(\Omega_{\mathbf{q}}) + f(\epsilon')}{\epsilon - \epsilon' + \Omega_{\mathbf{q}} + i\delta}\right)\right). \tag{A.26}$$

Because $\mathrm{Im}\,[G(\mathbf{k}-\mathbf{q},\epsilon')]$ depends on the electronic self-energy, this equation is self-consistent, and we can solve it recursively. Starting with a seed value of the self-energy (Σ^0), the first order expression is given by

$$\Sigma^1(\mathbf{k},\epsilon+i\delta) = -\frac{1}{\pi}\sum_{\mathbf{q}}\left(|g_{\mathbf{k},\mathbf{k}-\mathbf{q}}|^2\int d\epsilon'\,\mathrm{Im}\left[\frac{1}{\epsilon'-\epsilon_{\mathbf{k}-\mathbf{q}}-\Sigma^0+i\delta}\right]\right. \tag{A.27}$$
$$\left.\times\left(\frac{n_{\mathrm{B}}(\Omega_{\mathbf{q}})-f(\epsilon')+1}{\epsilon-\epsilon'-\Omega_{\mathbf{q}}+i\delta}+\frac{n_{\mathrm{B}}(\Omega_{\mathbf{q}})+f(\epsilon')}{\epsilon-\epsilon'+\Omega_{\mathbf{q}}+i\delta}\right)\right).$$

Continuing to higher order expressions is computationally expensive, since each order requires an integral over energies and a sum over momenta $\mathbf{q}$, and there is no telling how many iterations will be necessary. A more efficient way to find the self-consistent solution is to test a range of seed values Σ^0, and plot these against the "1-loop" result Σ^1. The resulting curve should be a continuous, smooth function, such that the intercept $\Sigma^1 = \Sigma^0$ is the self-consistent self-energy.

Within the charge-ordered phase, we have a self-energy *matrix* $\hat{\Sigma}$, rather than a function. The diagonal elements are the same self-energies as discussed above, while the off-diagonal elements of the matrix are the CDW gap functions $\Delta^{k_1}_{k_2}$. In this case, the elements m,n of $\hat{\Sigma}$ are described by

$$\Sigma^m_n(\mathbf{k},\epsilon+i\delta) = -\frac{1}{\pi}\sum_{\mathbf{q}}\left(g_{\mathbf{k}+m\mathbf{Q},\mathbf{k}-\mathbf{q}+m\mathbf{Q}}g_{\mathbf{k}-\mathbf{q}+n\mathbf{Q},\mathbf{k}+n\mathbf{Q}}\right.$$
$$\times\int d\epsilon'\,\mathrm{Im}\,[G^m_n(\mathbf{k}-\mathbf{q},\epsilon')] \tag{A.28}$$
$$\left.\times\left(\frac{n_{\mathrm{B}}(\Omega_{\mathbf{q}})-f(\epsilon')+1}{\epsilon-\epsilon'-\Omega_{\mathbf{q}}+i\delta}+\frac{n_{\mathrm{B}}(\Omega_{\mathbf{q}})+f(\epsilon')}{\epsilon-\epsilon'+\Omega_{\mathbf{q}}+i\delta}\right)\right),$$

where G^m_n denote the elements of the electron propagator matrix $\hat{G}$, comprised of G_{k+mQ} on the diagonal and anomalous propagators F^{k+mQ}_{k+nQ} away from the diagonal.

Summary

Electronic order:
Topology in crystals and symmetry-breaking from interactions

The electron was the first subatomic particle to be found experimentally, by J.J. Thomson in 1897 [243]. This carrier of negative charge has a mass of only 9.1×10^{-31} kg, but where would we be without it? Electrons form the basis of all electronics (the clue is in the name), so without it we would have no electric lighting, no computers, no internet, ... Most important of all,[1] without it this thesis would not have been possible. That's not just because much of the work presented in the present manuscript was dependent on the use of computers, but also because the (collective) behaviour of electrons makes for such an interesting topic of study. While we have measured the properties of the subatomic particle to extremely high precision, and we can easily predict what electrons in vacuum will do, electrons inside materials show beautiful and often tuneable emergent behaviour about which we still have much to learn. The focus of this thesis is precisely this collective behaviour.

The first thing one should note about electrons in matter, is that they're actually nothing like the subatomic particle. Interactions between an electron and the billions of particles that surround it in a material mean that it may for instance behave as if it has a completely different (effective) mass. We say the fundamental, 'bare' electrons are 'dressed' by interactions, becoming *quasiparticles*.[2] In fact, we can go a step further than this. In many materials, the atomic cores are arranged in a neat, orderly fashion, forming a periodic lattice; we call such materials *crystals*. The (quasi)electrons of the atoms in a crystal live in a periodic electric field generated by the positively charged atomic cores, and can move around by effectively hopping (or quantum-mechanically *tunnelling*) from one atom to the next. From this it follows that the atomic structure can have a huge influence on the behaviour of electrons in a material. In this thesis, we pose the question of what electronic phases of matter are made possible by the influence of the atomic lattice on the electrons that they host.

In Part I, we delve into the role of the symmetries of a crystal lattice. An example of this is the discrete translational symmetry generated by the periodicity of the lattice, which enforces that the quantum-mechanical wavefunctions

[1] ;)

[2] In some cases, even this quasiparticle picture breaks down.

describing electronic states[3] are also periodic. Importantly, it imposes that electronic wavefunctions may only be 'twisted' in certain ways, where twisting refers to how the phase of the wavefunction varies as you cycle through one period. A twisted wavefunction can only be untwisted by breaking a symmetry or changing the number of electrons in the system. These twisting conditions are a so-called *topological* feature, with the degree of twisting indicating the *topological phase* of the crystal. This leads to exotic phases such as topological insulators, which do not conduct electricity through the bulk, but host exotic electronic states on their surfaces that are protected by symmetry.

At present, the field of topology in condensed matter is edging towards completing the full topological classification of crystalline insulators, including the topological phases stabilised by all other possible lattice symmetries. This includes symmetries such as discrete rotations, reflections, and inversions, whose presence further constrains the electronic wavefunctions. While at this point it is known how many topological phases are possible, we still have not found a way to distinguish between all of them. In Chapter 3, we present a unifying framework with which we believe all crystalline topological invariants (which distinguish topological phases) may be identified. We demonstrate it for two-dimensional crystals with three-fold rotational symmetry, and discuss the generalisation of our method to other crystal symmetries.

In Part II of this thesis, we move away from topological insulators, and instead show how the interactions between electrons and the lattice they reside in can lead to ordered electronic phases that actually change the crystal symmetries. In these phases, electrons spontaneously form standing waves called *charge density waves* (CDWs), with wavelengths on the order of a few unit cells of the lattice. Electrons bunching up like this is something you'd never expect from bare electrons, because their negative charges mean they repel each other. The CDW is made possible by the fact that electrons also interact with vibrational modes of the crystal lattice, called *phonons*. By coupling together, the quasielectrons and dressed phonons find a new lowest-energy state, in which the CDW is accompanied by displacements of the positively charged atomic cores with the same periodicity as the CDW. Because materials change their atomic structure and their conductivity upon the transition to a CDW state, this type of charge order may be relevant for applications.

Most of the conventional wisdom regarding CDWs is derived from a simple, one-dimensional toy model. An important feature that this model neglects is that the strength of the coupling between electrons and phonons will depend on their momenta, as well as the orbital character and potentially even the spin of the electron. In this sense, we say that the electron-phonon coupling is *structured*. To incorporate such a structured coupling, we use a generally applicable method for describing charge order based on quantum field theory. We apply this method to analyse the CDWs in the real material VSe_2. This material is

[3] More formally, a wavefunction $\psi(\mathbf{r})$ describes the probability amplitude of finding an electron at position $\mathbf{r}$.

unusual, in that its three-dimensional electronic structure does not make it a likely candidate for hosting CDWs using the conventional wisdom. Additionally, the wavevectors of the CDWs it hosts were determined experimentally to vary with temperature, leading to the suggestion that the material might in fact host two distinct CDW phases. We show that both of these apparently anomalous features are easily explained by considering a structured coupling. Next, we consider what happens to this material when we thin it down to two dimensions. We demonstrate that when we go down to two layers of VSe_2, it still hosts CDWs with the same in-plane periodicity as the bulk material. However, in the monolayer limit, we encounter a dimensional crossover: the CDWs stop respecting the three-fold rotational symmetry of the lattice, and we can identify two distinct CDW types. One of these is still similar to the bulk CDW, while the other cannot be explained by electron-phonon coupling alone. The latter is most likely induced by Coulomb interactions, making monolayer VSe_2 the first material known to simultaneously host two types of CDWs with different driving mechanisms.

This thesis constitutes a step towards a complete understanding of the interplay between electrons and the lattice, and indicates a clear direction for future research. The unique environment provided to electrons by a crystal lattice lies at the heart of almost all exotic phases of matter, including those in which there are many different types of interactions that are difficult to disentangle. While we focussed on the two most fundamental types of electronic order, namely topology and charge order, our conclusions are general. We expect that the approaches demonstrated here, combined with modern computing power, will contribute to a more complete understanding of other, and perhaps even more exotic, phases of matter.

Samenvatting

Elektronische orde:
Topologie in kristallen en symmetriebreking door interacties

Het elektron is het eerste subatomaire deeltje dat experimenteel werd ontdekt, door J.J. Thomson in 1897 [243]. Deze drager van negatieve lading heeft een massa van slechts 9.1×10^{-31} kg, maar is van onmisbaar belang in ons dagelijks leven. Zonder elektronen zouden we geen elektrische verlichting hebben, geen computers, geen internet, ... En, als allerbelangrijkste,[1] zonder elektronen was dit proefschrift niet mogelijk geweest. Dat komt niet alleen omdat veel van het werk gepresenteerd in dit manuscript afhankelijk is van het gebruik van computers, maar ook omdat het (collectieve) gedrag van elektronen ons blijft verrassen en verwonderen. Hoewel we de eigenschappen van het subatomaire deeltje tot extreme precisie hebben gemeten, en we precies kunnen voorspellen wat een elektron in vacuüm zal doen, tonen elektronen in materialen bijzonder en vaak afstembaar gedrag waar we nog veel over kunnen leren. Dit laatste vormt de focus van dit proefschrift.

Het eerste wat je moet weten van elektronen in materie is dat ze weinig lijken op de 'vrije' elektronen waar deeltjesfysici het over hebben. Wisselwerkingen tussen een elektron en de miljarden atoomkernen en andere elektronen die hem in een materiaal omringen kunnen hem doen gedragen alsof hij bijvoorbeeld een compleet andere (effectieve) massa heeft. De wisselwerkingen toveren zo het vrije elektron om naar een *quasideeltje*.[2] In veel materialen zijn de atoomkernen netjes gerangschikt, zodat ze een periodiek rooster vormen; we noemen deze materialen *kristallen*. De (quasi)elektronen van de atomen in een kristal bevinden zich in een periodiek elektrisch veld gegenereerd door de positief geladen atoomkernen, en kunnen rondbewegen door van de ene atoomkern naar de volgende te springen (oftewel quantum-mechanisch te *tunnellen*). Hieruit is meteen duidelijk dat de structuur van het kristalrooster het gedrag van elektronen in het kristal sterk kan beïnvloeden. In dit proefschrift onderzoeken we welke soorten elektronische fases mogelijk worden gemaakt door de invloed van het atoomrooster op de elektronen in dat rooster.

In Deel I verdiepen we ons in de rol van de symmetrieën van het kristalrooster. Een voorbeeld hiervan is de discrete translatiesymmetrie die gegenereerd

[1] ;)

[2] In sommige gevallen, zoals bij sterke wisselwerkingen, werkt de beschrijving in termen van quasideeltjes ook niet meer.

wordt door de periodiciteit van het rooster. Deze zorgt ervoor dat de quantummechanische golffuncties die elektronische toestanden beschrijven[3] ook periodiek zijn. Belangrijk is dat dergelijke symmetrieën bepalen op welke manieren elektronische golffuncties 'gedraaid' mogen worden, waarbij draaien verwijst naar hoe de fase van de golffunctie varieert over een gesloten cyclus. Een gedraaide golffunctie kan zijn draaiing niet veranderen zonder een symmetrie te breken of het aantal elektronen in het systeem te veranderen. Hiermee vormt de draaiing van de golffunctie een zogeheten *topologische* eigenschap, waarbij de hoeveelheid draaiing een indicator is van de *topologische fase* van het kristal. Dit leidt tot exotische fases zoals topologische isolatoren: materialen die alleen elektriciteit geleiden via speciale, door-symmetrie-beschermde elektronische toestanden op hun oppervlakten.

Op dit moment naderen we de voltooiing van de volledige topologische classificatie van kristallijne isolatoren, inclusief de topologische fases die worden gestabiliseerd door (naast translatiesymmetrie) alle andere mogelijke roostersymmetrieën. Dit omvat symmetrieën zoals discrete rotaties, reflecties en inversies, waarvan de aanwezigheid de draaiing van elektronische golffuncties verder beperkt. Hoewel we nu weten hoeveel topologische fases er moeten bestaan, kunnen we ze nog niet allemaal van elkaar onderscheiden. In Hoofdstuk 3 presenteren we een verenigend raamwerk waarmee we geloven dat alle kristallijne topologische invarianten (die topologische fases onderscheiden) kunnen worden geïdentificeerd. We demonstreren dit voor tweedimensionale kristallen met drievoudige rotatiesymmetrie, en bespreken de generalisatie van onze methode naar andere symmetriegroepen.

In Deel II van dit proefschrift laten we zien hoe de interacties tussen elektronen en het rooster waarin ze zich bevinden kunnen leiden tot geordende elektronische fases die de kristalsymmetrieën juist doen veranderen. We bestuderen fases waarin elektronen staande golven vormen, geheten *ladingsdichtheidsgolven* (CDWs), met golflengtes van enkele eenheidscellen van het rooster. Dat de elektronen zo ophopen is iets dat je nooit van vrije elektronen zou verwachten, omdat ze elkaar afstoten met hun negatieve lading. Een CDW wordt mogelijk gemaakt doordat elektronen wisselwerken met trillingsmodi van het atoomrooster, zogeheten *fononen*. Door aan elkaar te koppelen, vinden de quasielektronen en fononen een nieuwe grondtoestand, waarin de CDW gepaard gaat met verplaatsingen van de positief geladen atoomkernen met dezelfde periodiciteit als de CDW. Omdat de overgang naar een CDW-toestand de atoomstructuur en geleidingseigenschappen van een materiaal veranderen, kan deze soort elektronische orde ook relevant zijn voor technologische toepassingen.

Bijna alle conventionele wijsheid met betrekking tot CDWs is afgeleid van een eenvoudig, eendimensionaal model van een kristal. Iets belangrijks dat dit model verwaarloost is dat de sterkte van de koppeling tussen elektronen en fononen zal afhangen van hun impuls, evenals in welke atomaire orbitaal het

[3]Formeler gezegd: een golffunctie $\psi(\mathbf{r})$ beschrijft de waarschijnlijkheidsamplitude dat je op positie $\mathbf{r}$ een elektron zult treffen.

elektron zich bevindt, en mogelijk zelfs zijn spin. In die zin zeggen we dat de elektron-fononkoppeling *gestructureerd* is. Om zo'n gestructureerde koppeling mee te kunnen nemen, gebruiken wij een algemeen toepasbare methode om de vorming van CDWs te beschrijven, gebaseerd op quantumveldentheorie. We passen deze methode toe op het materiaal VSe_2. Dit is een merkwaardig materiaal, omdat het een driedimensionale elektronenstructuur heeft die het geen typische kandidaat maakt voor het vormen van CDWs, als we de conventionele wijsheid zouden toepassen. Daarbovenop hebben experimenten aangetoond dat de golfvectoren van de CDWs veranderen met de temperatuur, wat leidde tot de suggestie dat het materiaal in feite twee verschillende CDW-fases zou kunnen bevatten. Wij laten zien dat beide ogenschijnlijk afwijkende kenmerken gemakkelijk kunnen worden verklaard door een gestructureerde koppeling te beschouwen. Vervolgens bekijken we wat er met dit materiaal gebeurt als we het verdunnen tot twee dimensies. Wanneer we het kristal reduceren tot een dikte van twee lagen, vormen er CDWs met dezelfde periodiciteit als in het bulkmateriaal. Dit verandert echter in de limiet van een enkele laag van VSe_2: de CDWs houden op met het respecteren van de drievoudige rotatiesymmetrie van het rooster, en we kunnen twee verschillende CDW-soorten identificeren. Één daarvan lijkt op de bulk-CDWs, terwijl de andere niet verklaard kan worden met alleen elektron-fononkoppeling. Deze laatste wordt hoogstwaarschijnlijk veroorzaakt door Coulomb-interacties, waardoor monolaag-VSe_2 het eerste materiaal is waarvan bekend is dat het twee soorten CDWs herbergt met hun oorsprong in verschillende mechanismen.

Dit proefschrift vormt een stap in de richting van een volledig begrip van het samenspel van elektronen en het rooster, en geeft een duidelijke richting aan voor toekomstig onderzoek – zowel theoretisch als in het belang van mogelijke toepassingen. De unieke omgeving die door een kristalrooster aan elektronen wordt geboden, vormt de kern van bijna alle exotische fases van materie, inclusief die waarin er veel verschillende soorten interacties bestaan die moeilijk te ontwarren zijn. Hoewel we ons hebben geconcentreerd op de twee meest fundamentele soorten elektronische orde, namelijk topologie en de vorming van ladingsdichtheidsgolven, zijn onze conclusies algemeen. We verwachten dat de hier gedemonstreerde benaderingen, gecombineerd met moderne rekenkracht, zullen bijdragen aan een vollediger begrip van nog vele andere, en allicht nog exotischere, fases der materie.

Acknowledgements

As is the case for any doctoral thesis, this work would not have been possible without the support of (many) others. It goes without saying that I owe credit to all my collaborators – the co-authors listed on page i – without whom none of my publications would have been possible. However, beyond professional collaboration, the support I have received from those around me has been amazing. First of all, I would like to express my endless gratitude for my supervisor, Jasper van Wezel. You've been my guide and my role model since we first started working together at the start of 2015, when I was still a bachelor student. Thanks for always making time for answering my questions, and for carrying me through all the ups and downs of my PhD. I admire your endless optimism, and I hope I've grown up to be a little bit more like you. And Felix, as far as role models go, you're high up on my list, too. I hope my research has done justice to the work you started with your PhD, and I hope to one day be the source of as many epic stories as you.

Despite the isolating influence of the coronavirus pandemic, it was my colleagues and friends who made my time at the UvA so enjoyable. I want to thank my academic siblings Ana, Jorrit, Joris, Mariia, Ananya, Corentin, Lotte and Aritro for all the fun group lunches and BBQs, the group meetings with their ever-changing format, and the adventurous outings – remember axe-throwing?! Corentin, you really embodied the definition of a co-worker, and being able to discuss any tiny physics detail with you was amazing. I already miss you as my dedicated online conference and pub quiz buddy, and I wish you all the best in Paris. Bart, thanks for keeping the CMT Journal Club alive with me, the CMT group would be nothing without you. And please keep twerking! Daniel and Rebekka, thanks for reminding me to keep a work-life balance ;) Dora, Evita, Carlos, Gabriele and Antonio, you were there from the first year of my PhD, thanks for being my connection to the dark side of physics, and showing me that High-Energy physicists can be cool, too. Steef, you're my PhD buddy and one of my best friends, and I am thankful for all the good times we've had in the last five years. You know, I think we're going to make it! To Mark and all the other QMatters that kept me in the loop of what's happening in the lab, thanks for making me feel like I'm part of your academic family. I will miss the after-work drinks from the magically replenishing lab fridge and at Oerknal. To the Friday Drinks group, the constancy offered by your presence, despite the ever-changing list of members, made sure I never felt alone.

I've been lucky to have support outside Science Park, too. My football team (Dames $5 \to 4 \to 3$) and bouldering buddies have kept me sane by making sure I don't spend too much time in the same seated position in front of my laptop.

During the lockdown, the virtual hiking competition to CERN was a lifesaver. On a more personal level, I have amazing friends who have been there for me as entertainers, co-adventurers, party-goers and advisers. Nila, Lily and Shreya, in the last twelve years we've transformed from silly teenagers into silly adults, but I am super grateful that when I'm with you, I get to feel sixteen again. Let's never stop bingeing and bitching and yes, fine, dressing up. Maggie, Maya and Roos, AUC seems like a long time ago now, but I foresee many more art afternoons, couch-potatoing, and having dinner together. Maybe even a bike holiday, Maggie? And hiking in Norway? Jack, thanks for still letting me make the most of, and inspiring me by, your happy-go-lucky-ness. Noor, you're a true power woman. You'll always impress me, and it's nice to have a friend who makes meaner jokes than me, especially when you're on my side. Magda, I'm so happy that you came to live with me, and that you stayed in Amsterdam after your PhD. You're kind and smart and beautiful, and I hope I'll be as successful as you at new beginnings. Nika, thanks for all the board gaming and cooking/crafting/cleaning inspiration, you're more than just a Magda 2.0 ;) Alona, I miss and admire your explosive energy. It's an uncertain time right now, but things will get better and I know we'll have many more adventures together. Tim, you pack an amazing amount of brains, nerdiness, kindness and enthusiasm into that tiny body of yours. Thanks for the karaoke and emotional analyses these last few years. Joris, I admire you for being someone who will always get things done; I hope some of this has rubbed off on me. Max, Bram, Fokel and Vicky, let's go on many more trips to places where we can go swimming (somehow that's what almost all our joint trips have in common). I look forward to Texel this summer!

And lastly, I could not have done any of this without my loved ones. Ferran, thanks for your unwavering support and for dealing with all my emotions, especially when I wasn't able to. Your patience and calming presence has been a godsend. And Alpha, our home would have been so much emptier without you. As resident lap-warmer, attention-hogger, frantic paper ball-swatter and loud-meowing toy-fetcher, you've brought me so much joy in the last four years. Thanks for reminding me to make the most of the simple things in life. Mam en pap, het maakt niet uit waar jullie wonen, want bij jullie voel ik me altijd thuis. Ik ben heel blij dat we elkaar de afgelopen paar jaar zo vaak hebben kunnen zien, en ik kijk uit naar onze gezamenlijke werkloosheid! Keiko, Lilo en Piet, ik zal altijd naar jullie op blijven kijken. Dank voor alle goede voorbeelden van hoe het eigenlijk moet, het leven en zo. Dorien en opa, dank voor jullie peetouderschap wanneer de Henkes allemaal ver weg waren. Zonder jullie was ik niet gekomen waar ik nu ben.

References

[1] J. Henke, M. Kurttutan, J. Kruthoff, and J. van Wezel, *Topological invariants of rotationally symmetric crystals*, Phys. Rev. B **104**, L201110 (2021).

[2] J. Henke, F. Flicker, J. Laverock, and J. van Wezel, *Charge order from structured coupling in VSe_2*, SciPost Phys. **9**, 56 (2020).

[3] R. Chua, J. Henke, S. Saha, Y. Huang, J. Gou, X. He, T. Das, J. van Wezel, A. Soumyanarayanan, and A. T. S. Wee, *Coexisting charge-ordered states with distinct driving mechanisms in monolayer VSe_2*, ACS Nano **16**, 783–791 (2022).

[4] X. Guo, A. Kogar, J. Henke, S. X.-L. Sun, I. Khayr, Y. Peng, S. Lee, M. J. Krogstad, D. Robinson, S. Rosenkranz, R. Osborn, J. P. C. Ru, D. B. Lioi, G. Karapetrov, D. J. Campbell, J. Paglione, J. van Wezel, T.-C. Chiang, and P. Abbamonte, *In-plane anisotropy of charge density wave fluctuations in $1T$-$TiSe_2$*, in preparation (2022).

[5] X. Feng, J. Henke, C. Morice, C. J. Sayers, E. Da Como, J. van Wezel, and E. van Heumen, *Signatures of the charge density wave collective mode in the infrared optical response of VSe_2*, Phys. Rev. B **104**, 165134 (2021).

[6] S. V. Ramankutty, J. Henke, A. Schiphorst, R. Nutakki, S. Bron, G. Araizi-Kanoutas, S. K. Mishra, L. Li, Y. K. Huang, T. K. Kim, M. Hoesch, C. Schlueter, T. L. Lee, A. de Visser, Z. Zhong, J. van Wezel, E. van Heumen, and M. S. Golden, *Electronic structure of the candidate 2D Dirac semimetal $SrMnSb_2$: a combined experimental and theoretical study*, SciPost Phys. **4**, 010 (2018).

[7] A. Silva, J. Henke, and J. van Wezel, *Elemental chalcogens as a minimal model for combined charge and orbital order*, Phys. Rev. B **97**, 045151 (2018).

[8] A. Nikitin, V. Grinenko, R. Sarkar, J.-C. Orain, M. Salis, J. Henke, Y. Huang, H.-H. Klauss, A. Amato, and A. de Visser, *Macroscopic phase separation of superconductivity and ferromagnetism in $Sr_{0.5}Ce_{0.5}FBiS_{2-x}Se_x$ revealed by μSR*, Sci. Rep. **7**, 1–7 (2017).

[9] S. de Haro, J. Henke, and D. Tang, *A. Cappelli, E. Castellani, F. Colomo and P. Di Vecchia (Eds.): The Birth of String Theory*, Found. Phys. **45**, 657–660 (2015).

[10] A. Fert, *Nobel lecture: Origin, development, and future of spintronics*, Rev. Mod. Phys. **80**, 1517–1530 (2008).

[11] C. H. Marrows and B. J. Hickey, *New directions in spintronics*, Philos. Trans. R. Soc. A **369**, 3027–3036 (2011), https://royalsocietypublishing.org/doi/pdf/10.1098/rsta.2011.0156 .

[12] W. Han, *Perspectives for spintronics in 2d materials*, APL Mater. **4**, 032401 (2016), https://doi.org/10.1063/1.4941712 .

[13] A. Avsar, H. Ochoa, F. Guinea, B. Özyilmaz, B. J. van Wees, and I. J. Vera-Marun, *Colloquium: Spintronics in graphene and other two-dimensional materials*, Rev. Mod. Phys. **92**, 021003 (2020).

[14] A. I. Buzdin, *Proximity effects in superconductor-ferromagnet heterostructures*, Rev. Mod. Phys. **77**, 935–976 (2005).

[15] J. Son, S. Rajan, S. Stemmer, and S. James Allen, *A heterojunction modulation-doped mott transistor*, J. Appl. Phys. **110**, 084503 (2011), https://doi.org/10.1063/1.3651612 .

[16] J. Chakhalian, J. W. Freeland, A. J. Millis, C. Panagopoulos, and J. M. Rondinelli, *Colloquium: Emergent properties in plane view: Strong correlations at oxide interfaces*, Rev. Mod. Phys. **86**, 1189–1202 (2014).

[17] D. V. Efremov, J. van den Brink, and D. I. Khomskii, *Bond-versus site-centred ordering and possible ferroelectricity in manganites*, Nat. Mater. **3**, 853 (2004).

[18] M. Gajek, M. Bibes, S. Fusil, K. Bouzehouane, J. Fontcuberta, A. Barthelemy, and A. Fert, *Tunnel junctions with multiferroic barriers*, Nat. mater. **6**, 296–302 (2007).

[19] S. W. E. Riester, I. Stolichnov, H. J. Trodahl, N. Setter, A. W. Rushforth, K. W. Edmonds, R. P. Campion, C. T. Foxon, B. L. Gallagher, and T. Jungwirth, *Toward a low-voltage multiferroic transistor: Magnetic (Ga,Mn)As under ferroelectric control*, Appl. Phys. Lett. **94**, 063504 (2009), https://doi.org/10.1063/1.3076107 .

[20] K.-T. Ko, M. H. Jung, Q. He, J. H. Lee, C. S. Woo, K. Chu, J. Seidel, B.-G. Jeon, Y. S. Oh, K. H. Kim, *et al.*, *Concurrent transition of ferroelectric and magnetic ordering near room temperature*, Nat. Commun. **2**, 567 (2011).

[21] P. Yu, Y. H. Chu, and R. Ramesh, *Emergent phenomena at multiferroic heterointerfaces*, Philos. Trans. R. Soc. A **370**, 4856–4871 (2012), https://royalsocietypublishing.org/doi/pdf/10.1098/rsta.2012.0199 .

[22] E. Tsymbal, A. Gruverman, V. Garcia, M. Bibes, and A. Barthélémy, *Ferroelectric and multiferroic tunnel junctions*, MRS Bull. **37**, 138–143 (2012).

[23] B.-K. Jang, J. H. Lee, K. Chu, P. Sharma, G.-Y. Kim, K.-T. Ko, K.-E. Kim, Y.-J. Kim, K. Kang, H.-B. Jang, *et al.*, *Electric-field-induced spin disorder-to-order transition near a multiferroic triple phase point*, Nat. Phys. **13**, 189 (2017).

[24] E. K. H. Salje, *Ferroelastic domain walls as templates for multiferroic devices*, J. Appl. Phys. **128**, 164104 (2020), https://doi.org/10.1063/5.0029160 .

[25] E. Dagotto, *Correlated electrons in high-temperature superconductors*, Rev. Mod. Phys. **66**, 763–840 (1994).

[26] S. Sachdev, *Colloquium: Order and quantum phase transitions in the cuprate superconductors*, Rev. Mod. Phys. **75**, 913–932 (2003).

[27] D. J. Scalapino, *A common thread: The pairing interaction for unconventional superconductors*, Rev. Mod. Phys. **84**, 1383–1417 (2012).

[28] E. Fradkin, S. A. Kivelson, and J. M. Tranquada, *Colloquium: Theory of intertwined orders in high temperature superconductors*, Rev. Mod. Phys. **87**, 457–482 (2015).

[29] N. E. Hussey, J. Buhot, and S. Licciardello, *A tale of two metals: contrasting criticalities in the pnictides and hole-doped cuprates*, Rep. Prog. Phys. **81**, 052501 (2018).

[30] J. Zaanen, *Planckian dissipation, minimal viscosity and the transport in cuprate strange metals*, SciPost Phys. **6**, 61 (2019).

[31] C. M. Varma, *Colloquium: Linear in temperature resistivity and associated mysteries including high temperature superconductivity*, Rev. Mod. Phys. **92**, 031001 (2020).

[32] F. Bloch, *Über die Quantenmechanik der Elektronen in Kristallgittern*, Zeitschrift für physik **52**, 555–600 (1929).

[33] N. P. Armitage, E. J. Mele, and A. Vishwanath, *Weyl and dirac semimetals in three-dimensional solids*, Rev. Mod. Phys. **90**, 015001 (2018).

[34] Y. Aharonov and D. Bohm, *Significance of electromagnetic potentials in the quantum theory*, Phys. Rev. **115**, 485–491 (1959).

[35] J. Kruthoff, J. de Boer, J. van Wezel, C. L. Kane, and R.-J. Slager, *Topological classification of crystalline insulators through band structure combinatorics*, Phys. Rev. X **7**, 041069 (2017).

[36] J. Kruthoff, J. de Boer, and J. van Wezel, *Topology in time-reversal symmetric crystals*, Phys. Rev. B **100**, 075116 (2019).

[37] A. Akhmerov, J. Sau, B. van Heck, S. Rubbert, R. Skolasiński, B. Nijholt, I. Muhammad, and T. Ö. Rosdahl, Topology in condensed matter: tying quantum knots, TU Delft (2021).

[38] M. Z. Hasan and C. L. Kane, *Colloquium : Topological insulators*, Rev. Mod. Phys. **82**, 3045–3067 (2010).

[39] X.-L. Qi and S.-C. Zhang, *Topological insulators and superconductors*, Rev. Mod. Phys. **83**, 1057–1110 (2011).

[40] D. Vanderbilt, *Berry Phases in Electronic Structure Theory: Electric Polarization, Orbital Magnetization and Topological Insulators*, Titolo collana (Cambridge University Press, 2018).

[41] J. H. Hannay, *Angle variable holonomy in adiabatic excursion of an integrable Hamiltonian*, J. Phys. A **18**, 221–230 (1985).

[42] Geek3, Sphere wireframe, Wikipedia (2009).

[43] M. V. Berry, *Quantal phase factors accompanying adiabatic changes*, Proceedings of the Royal Society of London. A. Mathematical and Physical Sciences **392**, 45–57 (1984).

[44] J. Zak, *Berry's phase for energy bands in solids*, Phys. Rev. Lett. **62**, 2747–2750 (1989).

[45] T. Kato, *On the adiabatic theorem of quantum mechanics*, J. Phys. Soc. Japan **5**, 435–439 (1950).

[46] S. Pancharatnam, *Generalized theory of interference, and its applications*, Proc. Ind. Acad. Sci. - Sect. A **44**, 247–262 (1956).

[47] H. C. Longuet-Higgins, U. Öpik, M. H. L. Pryce, and R. Sack, *Studies of the Jahn-Teller effect .II. the dynamical problem*, Proceedings of the Royal Society Lond. A **244**, 1–16 (1958).

[48] S.-S. Chern, *A simple intrinsic proof of the Gauss-Bonnet formula for closed Riemannian manifolds*, Ann. Math. **45**, 747–752 (1944).

[49] D. J. Thouless, M. Kohmoto, M. P. Nightingale, and M. den Nijs, *Quantized Hall conductance in a two-dimensional periodic potential*, Phys. Rev. Lett. **49**, 405–408 (1982).

[50] J. E. Avron and R. Seiler, *Quantization of the Hall conductance for general, multiparticle Schrödinger Hamiltonians*, Phys. Rev. Lett. **54**, 259–262 (1985).

[51] K. v. Klitzing, G. Dorda, and M. Pepper, *New method for high-accuracy determination of the fine-structure constant based on quantized Hall resistance*, Phys. Rev. Lett. **45**, 494–497 (1980).

[52] F. D. M. Haldane, *Model for a quantum hall effect without Landau levels: Condensed-matter realization of the "parity anomaly"*, Phys. Rev. Lett. **61**, 2015–2018 (1988).

[53] C.-Z. Chang, J. Zhang, X. Feng, J. Shen, Z. Zhang, M. Guo, K. Li, Y. Ou, P. Wei, L.-L. Wang, Z.-Q. Ji, Y. Feng, S. Ji, X. Chen, J. Jia, X. Dai, Z. Fang, S.-C. Zhang, K. He, Y. Wang, L. Lu, X.-C. Ma, and Q.-K. Xue, *Experimental observation of the quantum anomalous Hall effect in a magnetic topological insulator*, Science **340**, 167–170 (2013).

[54] H. Weng, R. Yu, X. Hu, X. Dai, and Z. Fang, *Quantum anomalous Hall effect and related topological electronic states*, Adv. Phys. **64**, 227–282 (2015).

[55] H. A. Kramers, *Théorie générale de la rotation paramagnétique dans les cristaux*, Proc. Acad. Amst **33** (1930).

[56] E. Wigner, *And its Applications to the Quantum Mechanics of Atomic Spectra* (Academic Press, 1959) p. 386.

[57] F. J. Dyson, *The threefold way. algebraic structure of symmetry groups and ensembles in quantum mechanics*, J. Math. Phys. **3**, 1199–1215 (1962).

[58] E. Shuryak and J. Verbaarschot, *Random matrix theory and spectral sum rules for the Dirac operator in QCD*, Nucl. Phys. A **560**, 306–320 (1993).

[59] J. Verbaarschot, *Spectrum of the QCD Dirac operator and chiral random matrix theory*, Phys. Rev. Lett. **72**, 2531–2533 (1994).

[60] A. Altland and M. R. Zirnbauer, *Nonstandard symmetry classes in mesoscopic normal-superconducting hybrid structures*, Phys. Rev. B **55**, 1142–1161 (1997).

[61] A. P. Schnyder, S. Ryu, A. Furusaki, and A. W. W. Ludwig, *Classification of topological insulators and superconductors in three spatial dimensions*, Phys. Rev. B **78**, 195125 (2008).

[62] S. Ryu, A. P. Schnyder, A. Furusaki, and A. W. W. Ludwig, *Topological insulators and superconductors: tenfold way and dimensional hierarchy*, New J. Phys. **12**, 065010 (2010).

[63] J. C. Slater and G. F. Koster, *Simplified LCAO method for the periodic potential problem*, Phys. Rev. **94**, 1498–1524 (1954).

[64] L. Fu, C. L. Kane, and E. J. Mele, *Topological insulators in three dimensions*, Phys. Rev. Lett. **98**, 106803 (2007).

[65] L. Fu and C. L. Kane, *Time reversal polarization and a Z_2 adiabatic spin pump*, Phys. Rev. B **74**, 195312 (2006).

[66] L. Fu and C. L. Kane, *Topological insulators with inversion symmetry*, Phys. Rev. B **76**, 045302 (2007).

[67] S.-S. Lee and S. Ryu, *Many-body generalization of the Z_2 topological invariant for the quantum spin Hall effect*, Phys. Rev. Lett. **100**, 186807 (2008).

[68] R. Yu, X. L. Qi, A. Bernevig, Z. Fang, and X. Dai, *Equivalent expression of F_2 topological invariant for band insulators using the non-abelian Berry connection*, Phys. Rev. B **84**, 075119 (2011).

[69] A. Alexandradinata, X. Dai, and B. A. Bernevig, *Wilson-loop characterization of inversion-symmetric topological insulators*, Phys. Rev. B **89**, 155114 (2014).

[70] B. Bradlyn, Z. Wang, J. Cano, and B. A. Bernevig, *Disconnected elementary band representations, fragile topology, and wilson loops as topological indices: An example on the triangular lattice*, Phys. Rev. B **99**, 045140 (2019).

[71] C. L. Kane and E. J. Mele, *Quantum spin hall effect in graphene*, Phys. Rev. Lett. **95**, 226801 (2005).

[72] C. L. Kane and E. J. Mele, *Z_2 topological order and the quantum spin hall effect*, Phys. Rev. Lett. **95**, 146802 (2005).

[73] S. Bader and S. Parkin, *Spintronics*, Annu. Rev. Condens. Matter Phys. **1**, 71–88 (2010).

[74] M. König, S. Wiedmann, C. Brüne, A. Roth, H. Buhmann, L. W. Molenkamp, X.-L. Qi, and S.-C. Zhang, *Quantum spin hall insulator state in HgTe quantum wells*, Science **318**, 766–770 (2007).

[75] B. A. Bernevig, T. L. Hughes, and S.-C. Zhang, *Quantum spin Hall effect and topological phase transition in HgTe quantum wells*, Science **314**, 1757–1761 (2006).

[76] C. Fang, M. J. Gilbert, and B. A. Bernevig, *Bulk topological invariants in noninteracting point group symmetric insulators*, Phys. Rev. B **86**, 115112 (2012).

[77] R.-J. Slager, A. Mesaros, V. Juričić, and J. Zaanen, *The space group classification of topological band-insulators*, Nat Phys **9**, 98–102 (2013).

[78] L. Fu, *Topological crystalline insulators*, Phys. Rev. Lett. **106**, 106802 (2011).

[79] A. Alexandradinata and B. A. Bernevig, *Berry-phase description of topological crystalline insulators*, Phys. Rev. B **93**, 205104 (2016).

[80] W. A. Benalcazar, B. A. Bernevig, and T. L. Hughes, *Quantized electric multipole insulators*, Science **357**, 61–66 (2017).

[81] F. Schindler, A. M. Cook, M. G. Vergniory, Z. Wang, S. S. P. Parkin, B. A. Bernevig, and T. Neupert, *Higher-order topological insulators*, Sci. Adv. **4**, eaat0346 (2018).

[82] W. A. Benalcazar, T. Li, and T. L. Hughes, *Quantization of fractional corner charge in C_n-symmetric higher-order topological crystalline insulators*, Phys. Rev. B **99**, 245151 (2019).

[83] S. H. Kooi, G. van Miert, and C. Ortix, *Hybrid-order topology of weak topological insulators*, Phys. Rev. B **102**, 041122 (2020).

[84] S. Kooi, G. van Miert, and C. Ortix, *The bulk-corner correspondence of time-reversal symmetric insulators*, npj Quantum Materials **6**, 1–12 (2021).

[85] K. Shiozaki and M. Sato, *Topology of crystalline insulators and superconductors*, Phys. Rev. B **90**, 165114 (2014).

[86] K. Shiozaki, M. Sato, and K. Gomi, *Topology of nonsymmorphic crystalline insulators and superconductors*, Phys. Rev. B **93**, 195413 (2016).

[87] B. Bradlyn, L. Elcoro, J. Cano, M. Vergniory, Z. Wang, C. Felser, M. Aroyo, and B. A. Bernevig, *Topological quantum chemistry*, Nature **547**, 298–305 (2017).

[88] K. Shiozaki, M. Sato, and K. Gomi, Atiyah-Hirzebruch spectral sequence in band topology: General formalism and topological invariants for 230 space groups (2018), arXiv:1802.06694 [cond-mat.str-el] .

[89] D. S. Freed and G. W. Moore, *Twisted equivariant matter*, Annales Henri Poincaré **14**, 1927–2023 (2013).

[90] G. C. Thiang, *On the K-theoretic classification of topological phases of matter*, Ann. Henri Poincaré **17**, 757–794 (2016).

[91] L. Stehouwer, J. de Boer, J. Kruthoff, and H. Posthuma, Classification of crystalline topological insulators through K-theory (2018), arXiv:1811.02592 [cond-mat.mes-hall] .

[92] E. Cornfeld and S. Carmeli, *Tenfold topology of crystals: Unified classification of crystalline topological insulators and superconductors*, Phys. Rev. Research **3**, 10.1103/physrevresearch.3.013052 (2021).

[93] L. P. Bouckaert, R. Smoluchowski, and E. Wigner, *Theory of Brillouin zones and symmetry properties of wave functions in crystals*, Phys. Rev. **50**, 58–67 (1936).

[94] T. Hahn, The 17 plane groups (two-dimensional space groups), in *International Tables for Crystallography Volume A: Space-group symmetry* (Springer Netherlands, Dordrecht, 2002) pp. 92–109.

[95] A. Lau, J. van den Brink, and C. Ortix, *Topological mirror insulators in one dimension*, Phys. Rev. B **94**, 165164 (2016).

[96] S. H. Kooi, G. van Miert, and C. Ortix, *Classification of crystalline insulators without symmetry indicators: Atomic and fragile topological phases in twofold rotation symmetric systems*, Phys. Rev. B **100**, 115160 (2019).

[97] G. De Nittis and K. Gomi, *Classification of "quaternionic" Bloch–bundles*, Commun. Math. Phys. **339**, 1–55 (2015).

[98] A. Bouhon, A. M. Black-Schaffer, and R.-J. Slager, *Wilson loop approach to fragile topology of split elementary band representations and topological crystalline insulators with time-reversal symmetry*, Phys. Rev. B **100**, 195135 (2019).

[99] Y. Hwang, J. Ahn, and B.-J. Yang, *Fragile topology protected by inversion symmetry: Diagnosis, bulk-boundary correspondence, and Wilson loop*, Phys. Rev. B **100**, 205126 (2019).

[100] A. Bouhon, G. F. Lange, and R.-J. Slager, *Topological correspondence between magnetic space group representations and subdimensions*, Phys. Rev. B **103**, 245127 (2021).

[101] G. F. Lange, A. Bouhon, and R.-J. Slager, *Subdimensional topologies, indicators, and higher order boundary effects*, Phys. Rev. B **103**, 195145 (2021).

[102] H. C. Po, A. Vishwanath, and H. Watanabe, *Symmetry-based indicators of band topology in the 230 space groups*, Nat. Commun. **8**, 10.1038/s41467-017-00133-2 (2017).

[103] H. Watanabe, H. C. Po, and A. Vishwanath, *Structure and topology of band structures in the 1651 magnetic space groups*, Sci. Adv. **4**, eaat8685 (2018).

[104] A. Alexandradinata, C. Fang, M. J. Gilbert, and B. A. Bernevig, *Spin-orbit-free topological insulators without time-reversal symmetry*, Phys. Rev. Lett. **113**, 116403 (2014).

[105] S. M. Young and C. L. Kane, *Dirac semimetals in two dimensions*, Phys. Rev. Lett. **115**, 126803 (2015).

[106] H. C. Po, H. Watanabe, and A. Vishwanath, *Fragile topology and Wannier obstructions*, Phys. Rev. Lett. **121**, 126402 (2018).

[107] Z.-D. Song, L. Elcoro, and B. A. Bernevig, *Twisted bulk-boundary correspondence of fragile topology*, Science **367**, 794–797 (2020).

[108] D. Sticlet and F. Piéchon, *Distant-neighbor hopping in graphene and Haldane models*, Phys. Rev. B **87**, 115402 (2013).

[109] U. Bhattacharya, J. Hutchinson, and A. Dutta, *Quenching in Chern insulators with satellite Dirac points: The fate of edge states*, Phys. Rev. B **95**, 144304 (2017).

[110] D. Moldovan, M. Anđelković, and F. Peeters, pybinding v0.9.5: a Python package for tight- binding calculations (2020).

[111] C. Morice, T. Kopp, and A. P. Kampf, *Nonunique connection between bulk topological invariants and surface physics*, Phys. Rev. B **100**, 235427 (2019).

[112] Y. Kakehashi, Antiferromagnetism and spin density waves, in *Modern Theory of Magnetism in Metals and Alloys* (Springer Berlin Heidelberg, Berlin, Heidelberg, 2013) pp. 149–180.

[113] J. Chang, E. Blackburn, A. Holmes, N. B. Christensen, J. Larsen, J. Mesot, R. Liang, D. Bonn, W. Hardy, A. Watenphul, M. Zimmermann, E. Forgan, and S. Hayden, *Direct observation of competition between superconductivity and charge density wave order in* $YBa_2Cu_3O_6$.67, Nat. Phys. **8**, 871 (2012).

[114] G. Ghiringhelli, M. Le Tacon, M. Minola, S. Blanco-Canosa, C. Mazzoli, N. B. Brookes, G. M. De Luca, A. Frano, D. G. Hawthorn, F. He, T. Loew, M. M. Sala, D. C. Peets, M. Salluzzo, E. Schierle, R. Sutarto, G. A. Sawatzky, E. Weschke, B. Keimer, and L. Braicovich, *Long-range incommensurate charge fluctuations in (Y,Nd)*$Ba_2Cu_3O_{6+x}$, Science **337**, 821–825 (2012).

[115] A. Achkar, F. He, R. Sutarto, C. McMahon, M. Zwiebler, M. Hücker, G. Gu, R. Liang, D. Bonn, W. Hardy, J. Geck, and D. Hawthorn, *Orbital symmetry of charge-density-wave order in* $La_1.875Ba_0.125CuO_4$ *and* $YBa_2Cu_3O_6$.67, Nat. Mater. **15**, 616 (2016).

[116] E. P. Rosenthal, E. F. Andrade, C. J. Arguello, R. M. Fernandes, L. Y. Xing, X. Wang, C. Jin, A. J. Millis, and A. N. Pasupathy, *Visualization of electron nematicity and unidirectional antiferroic fluctuations at high temperatures in NaFeAs*, Nat. Phys. **10**, 225 (2014).

[117] T. Shimojima, W. Malaeb, A. Nakamura, T. Kondo, K. Kihou, C.-H. Lee, A. Iyo, H. Eisaki, S. Ishida, M. Nakajima, S.-i. Uchida, K. Ohgushi, K. Ishizaka, and S. Shin, *Antiferroic electronic structure in the nonmagnetic superconducting state of the iron-based superconductors*, Sci. Adv. **3**, 10.1126/sciadv.1700466 (2017).

[118] M. Hervieu, A. Barnabé, C. Martin, A. Maignan, F. Damay, and B. Raveau, *Evolution of charge ordering in manganites*, Eur. Phys. J. B **8**, 31–41 (1999).

[119] I. El Baggari, B. H. Savitzky, A. S. Admasu, J. Kim, S.-W. Cheong, R. Hovden, and L. F. Kourkoutis, *Nature and evolution of incommensurate charge order in manganites visualized with cryogenic scanning transmission electron microscopy*, Proc. Natl. Acad. Sci. U.S.A. **115**, 1445–1450 (2018).

[120] Y. Cao, Z. Wang, S. Y. Park, Y. Yuan, X. Liu, S. M. Nikitin, H. Akamatsu, M. Kareev, S. Middey, D. Meyers, *et al.*, *Artificial two-dimensional polar metal at room temperature*, Nat. Commun. **9**, 1547 (2018).

[121] C. W. Rischau, X. Lin, C. P. Grams, D. Finck, S. Harms, J. Engelmayer, T. Lorenz, Y. Gallais, B. Fauqué, J. Hemberger, *et al.*, *A ferroelectric quantum phase transition inside the superconducting dome of* $Sr_{1-x}Ca_xTiO_{3-\delta}$, Nat. Phys. **13**, 643 (2017).

[122] Á. Pásztor, A. Scarfato, C. Barreteau, E. Giannini, and C. Renner, *Dimensional crossover of the charge density wave transition in thin exfoliated* VSe_2, 2D Mater. **4**, 041005 (2017).

[123] S. Manzeli, D. Ovchinnikov, D. Pasquier, O. V. Yazyev, and A. Kis, *2D transition metal dichalcogenides*, Nat. Rev. Mater. **2**, 17033 (2017).

[124] W. Jolie, T. Knispel, N. Ehlen, K. Nikonov, C. Busse, A. Grüneis, and T. Michely, *Charge density wave phase of* VSe_2 *revisited*, Phys. Rev. B **99**, 115417 (2019).

[125] R. Peierls, *Quantum Theory of Solids* (Oxford University Press, 1955).

[126] R. Peierls, *More Surprises in Theoretical Physics*, Vol. 19 (Princeton University Press, 1991).

[127] G. Mahan, *Many-Particle Physics*, 3rd ed. (Kluwer Academic/Plenum Publishers, 2000).

[128] A. Kotani, *Continuity of self-consistent solutions between commensurate and incommensurate phases of the Peierls instability. I. analytic investigations*, J. Phys. Soc. Japan **42**, 408–415 (1977).

[129] K. Rossnagel, *On the origin of charge-density waves in select layered transition-metal dichalcogenides*, JJ. Phys. Condens. Matter **23**, 213001 (2011).

[130] A. Kotani, *Continuity of self-consistent solutions between commensurate and incommensurate phases of the Peierls instability. II. numerical calculations at zero temperature*, J. Phys. Soc. Japan **42**, 416–423 (1977).

[131] A. Kotani and I. Harada, *Mean-field theory of Peierls and spin-Peierls instabilities – commensurability, harmonics and dimerized-state pinning*, J. Phys. Soc. Japan **49**, 535–544 (1980).

[132] W. Kohn, *Image of the Fermi surface in the vibration spectrum of a metal*, Phys. Rev. Lett. **2**, 393–394 (1959).

[133] J. van Wezel, *Chirality and orbital order in charge density waves*, EPL **96**, 67011 (2011).

[134] J. Ishioka, Y. H. Liu, K. Shimatake, T. Kurosawa, K. Ichimura, Y. Toda, M. Oda, and S. Tanda, *Chiral charge-density waves*, Phys. Rev. Lett. **105**, 176401 (2010).

[135] B. Hildebrand, T. Jaouen, M.-L. Mottas, G. Monney, C. Barreteau, E. Giannini, D. R. Bowler, and P. Aebi, *Local real-space view of the achiral* $1T$*-*$TiSe_2$ $2 \times 2 \times 2$ *charge density wave*, Phys. Rev. Lett. **120**, 136404 (2018).

[136] F. J. Di Salvo, D. E. Moncton, and J. V. Waszczak, *Electronic properties and superlattice formation in the semimetal* $TiSe_2$, Phys. Rev. B **14**, 4321–4328 (1976).

[137] N. Wakabayashi, H. Smith, K. Woo, and F. Brown, *Phonons and charge density waves in* $1T$*-*$TiSe_2$, Solid State Commun. **28**, 923–926 (1978).

[138] G. Margaritondo, C. M. Bertoni, J. H. Weaver, F. Lévy, N. G. Stoffel, and A. D. Katnani, *Density-of-states changes near the Fermi level and the lattice instability in* $TiSe_2$, Phys. Rev. B **23**, 3765–3769 (1981).

[139] O. Anderson, G. Karschnick, R. Manzke, and M. Skibowski, *The phase transition in the electronic structure of* $1T$*-*$TiSe_2$, Solid State Commun. **53**, 339–342 (1985).

[140] J.-P. Castellan, S. Rosenkranz, R. Osborn, Q. Li, K. E. Gray, X. Luo, U. Welp, G. Karapetrov, J. P. C. Ruff, and J. van Wezel, *Chiral phase transition in charge ordered* $1T$*-*$TiSe_2$, Phys. Rev. Lett. **110**, 196404 (2013).

[141] M.-K. Lin, J. A. Hlevyack, P. Chen, R.-Y. Liu, and T.-C. Chiang, *Comment on "Chiral phase transition in charge ordered* $1T$*-*$TiSe_2$*"*, Phys. Rev. Lett. **122**, 229701 (2019).

[142] S. Rosenkranz, R. Osborn, and J. van Wezel, *Rosenkranz, Osborn, and van Wezel reply:*, Phys. Rev. Lett. **122**, 229702 (2019).

[143] H. Ueda, M. Porer, J. R. L. Mardegan, S. Parchenko, N. Gurung, F. Fabrizi, M. Ramakrishnan, L. Boie, M. J. Neugebauer, B. Burganov, M. Burian, S. L. Johnson, K. Rossnagel, and U. Staub, *Correlation between electronic and structural orders in* $1T$*-*$TiSe_2$, Phys. Rev. Research **3**, L022003 (2021).

[144] S.-Y. Xu, Q. Ma, Y. Gao, A. Kogar, A. Zong, A. M. M. Valdivia, T. H. Dinh, S.-M. Huang, B. Singh, C.-H. Hsu, T.-R. Chang, J. P. C. Ruff, K. Watanabe, T. Taniguchi, H. Lin, G. Karapetrov, D. Xiao, P. Jarillo-Herrero, and N. Gedik, *Spontaneous gyrotropic electronic order in a transition-metal dichalcogenide*, Nature **578**, 545–549 (2020).

[145] Y. Peng, X. Guo, Q. Xiao, Q. Li, J. Strempfer, Y. Choi, D. Yan, H. Luo, Y. Huang, S. Jia, O. Janson, P. Abbamonte, J. van den Brink, and J. van Wezel, Observation of orbital order in the van der Waals material $1T$-$TiSe_2$ (2021), arXiv:2105.13195 [cond-mat.str-el] .

[146] A. Kogar, M. S. Rak, S. Vig, A. A. Husain, F. Flicker, Y. I. Joe, L. Venema, G. J. MacDougall, T. C. Chiang, E. Fradkin, J. van Wezel, and P. Abbamonte, *Signatures of exciton condensation in a transition metal dichalcogenide*, Science **358**, 1314–1317 (2017).

[147] B. Zenker, H. Fehske, H. Beck, C. Monney, and A. R. Bishop, *Chiral charge order in* $1T$*-*$TiSe_2$*: Importance of lattice degrees of freedom*, Phys. Rev. B **88**, 075138 (2013).

[148] X. Zhu, Y. Cao, J. Zhang, E. W. Plummer, and J. Guo, *Classification of charge density waves based on their nature*, Proc. Natl. Acad. Sci. U.S.A. **112**, 2367–2371 (2015).

[149] M. H. Whangbo, E. Canadell, and C. Schlenker, *Band electronic structure of the purple potassium molybdenum bronze* $K_{0.9}Mo_6O_17$, J. Am. Chem. Soc. **109**, 6308–6313 (1987).

[150] M.-H. Whangbo, E. Canadell, P. Foury, and J.-P. Pouget, *Hidden Fermi surface nesting and charge density wave instability in low-dimensional metals*, Science **252**, 96–98 (1991).

[151] L. Su, C.-H. Hsu, H. Lin, and V. M. Pereira, *Charge density waves and the hidden nesting of purple bronze* $K_{0.9}Mo_6O_{17}$, Phys. Rev. Lett. **118**, 257601 (2017).

[152] H. Yao, J. A. Robertson, E.-A. Kim, and S. A. Kivelson, *Theory of stripes in quasi-two-dimensional rare-earth tellurides*, Phys. Rev. B **74**, 245126 (2006).

[153] H. P. Hughes, *Structural distortion in TiSe2and related materials-a possible jahn-teller effect?*, J. Phys. C: Solid State Phys. **10**, L319–L323 (1977).

[154] K. Rossnagel, L. Kipp, and M. Skibowski, *Charge-density-wave phase transition in 1T-$TiSe_2$: Excitonic insulator versus band-type Jahn-Teller mechanism*, Phys. Rev. B **65**, 235101 (2002).

[155] B. I. Halperin and T. M. Rice, *Possible anomalies at a semimetal-semiconductor transistion*, Rev. Mod. Phys. **40**, 755–766 (1968).

[156] T. M. Rice and G. K. Scott, *New mechanism for a charge-density-wave instability*, Phys. Rev. Lett. **35**, 120–123 (1975).

[157] K. Rossnagel, O. Seifarth, L. Kipp, M. Skibowski, D. Voß, P. Krüger, A. Mazur, and J. Pollmann, *Fermi surface of 2H-$NbSe_2$ and its implications on the charge-density-wave mechanism*, Phys. Rev. B **64**, 235119 (2001).

[158] F. Flicker and J. van Wezel, *Charge order from orbital-dependent coupling evidenced by $NbSe_2$*, Nat. Commun. **6**, 7034 (2015).

[159] F. Flicker and J. van Wezel, *Charge order in $NbSe_2$*, Phys. Rev. B **94**, 235135 (2016).

[160] J. Berges, E. G. C. P. van Loon, A. Schobert, M. Rösner, and T. O. Wehling, *Ab initio phonon self-energies and fluctuation diagnostics of phonon anomalies: Lattice instabilities from Dirac pseudospin physics in transition metal dichalcogenides*, Phys. Rev. B **101**, 155107 (2020).

[161] A. Altland and B. D. Simons, *Condensed matter field theory* (Cambridge university press, 2010).

[162] F. Flicker, *The Geometry and Topology of Charge-Ordered Quantum Fields in Low-Dimensional Systems*, PhD dissertation, University of Bristol, Faculty of Science (2015).

[163] C. M. Varma and W. Weber, *Phonon dispersion in transition metals*, Phys. Rev. Lett. **39**, 1094–1098 (1977).

[164] N. J. Doran, *A calculation of the electronic response function in 2$H-NbSe_2$ including electron-phonon matrix element effects*, J. Phys. C: Solid State Phys. **11**, L959–L962 (1978).

[165] F. Giustino, *Electron-phonon interactions from first principles*, Rev. Mod. Phys. **89**, 015003 (2017).

[166] C. M. Varma, E. I. Blount, P. Vashishta, and W. Weber, *Electron-phonon interactions in transition metals*, Phys. Rev. B **19**, 6130 (1979).

[167] C. M. Varma and A. L. Simons, *Strong-coupling theory of charge-density-wave transitions*, Phys. Rev. Lett. **51**, 138–141 (1983).

[168] H. Yoshiyama, Y. Takaoka, N. Suzuki, and K. Motizuki, *Effects on lattice fluctuations on the charge-density-wave transition in transition-metal dichalcogenides*, J. Phys. C: Solid State Phys. **19**, 5591–5606 (1986).

[169] A. Damascelli, Z. Hussain, and Z.-X. Shen, *Angle-resolved photoemission studies of the cuprate superconductors*, Rev. Mod. Phys. **75**, 473–541 (2003).

[170] S. Hüfner, *Photoelectron spectroscopy: principles and applications* (Springer Science & Business Media, 2013).

[171] Y. Nambu, *Quasi-particles and gauge invariance in the theory of superconductivity*, Phys. Rev. **117**, 648–663 (1960).

[172] L. P. Gor'kov, *On the enery spectrum of superconductors*, Sov. Phys. JETP **7**, 158 (1958).

[173] N. Bogoliubov, *A new method in the theory of superconductivity. I, III*, Sov. Phys. JETP **34**, 73 (1958).

[174] P. De Gennes and P. Pincus(*Trans.*), *Superconductivity Of Metals And Alloys*, edited by D. Pines (W.A. Benjamin, Inc. New York, 1966).

[175] J.-X. Zhu, *Bogoliubov-de Gennes Method and Its Applications* (Springer, Cham, 2016).

[176] T. Straub, T. Finteis, R. Claessen, P. Steiner, S. Hüfner, P. Blaha, C. S. Oglesby, and E. Bucher, *Charge-density-wave mechanism in $2H$-$NbSe_2$: Photoemission results*, Phys. Rev. Lett. **82**, 4504–4507 (1999).

[177] S. Borisenko, A. Kordyuk, V. Zabolotnyy, D. Inosov, D. Evtushinsky, B. Büchner, A. Yaresko, A. Varykhalov, R. Follath, W. Eberhardt, *et al.*, *Two energy gaps and Fermi-surface "arcs" in $NbSe_2$*, Phys. Rev. Lett. **102**, 166402 (2009).

[178] D. J. Rahn, S. Hellmann, M. Kalläne, C. Sohrt, T. K. Kim, L. Kipp, and K. Rossnagel, *Gaps and kinks in the electronic structure of the superconductor $2H$-$NbSe_2$ from angle-resolved photoemission at 1 K*, Phys. Rev. B **85**, 224532 (2012).

[179] M. D. Johannes and I. I. Mazin, *Fermi surface nesting and the origin of charge density waves in metals*, Phys. Rev. B **77**, 165135 (2008).

[180] B. Guster, M. Pruneda, P. Ordejón, E. Canadell, and J.-P. Pouget, *Evidence for the weak coupling scenario of the Peierls transition in the blue bronze*, Phys. Rev. Mater. **3**, 055001 (2019), In their Sec. IV C, they note

that they added a shift to their Lindhard function to make it fit to experimental data, which exhibits a temperature dependence their calculations cannot account for.

[181] K. Tsutsumi, *X-ray-diffraction study of the periodic lattice distortion associated with a charge-density wave in* $1T$-VSe_2, Phys. Rev. B **26**, 5756–5759 (1982).

[182] F. Di Salvo and J. Waszczak, *The effect of Fe substitution on the charge density wave in* VSe_2, J. Phys. Colloq. **37**, C4–157–C4–161 (1976).

[183] F. J. DiSalvo and J. V. Waszczak, *Magnetic studies of* VSe_2, Phys. Rev. B **23**, 457–461 (1981).

[184] K. Terashima, T. Sato, H. Komatsu, T. Takahashi, N. Maeda, and K. Hayashi, *Charge-density wave transition of* $1T$-VSe_2 *studied by angle-resolved photoemission spectroscopy*, Phys. Rev. B **68**, 155108 (2003).

[185] V. N. Strocov, M. Shi, M. Kobayashi, C. Monney, X. Wang, J. Krempasky, T. Schmitt, L. Patthey, H. Berger, and P. Blaha, *Three-dimensional electron realm in* VSe_2 *by soft-X-ray photoelectron spectroscopy: Origin of charge-density waves*, Phys. Rev. Lett. **109**, 086401 (2012).

[186] M. Cattelan and N. A. Fox, *A perspective on the application of spatially resolved ARPES for 2D materials*, Nanomaterials **8**, 10.3390/nano8050284 (2018).

[187] A. Jones, C. Sayers, M. Cattelan, N. Fox, E. da Como, and J. Laverock (2018), unpublished.

[188] P. Chen, W. W. Pai, Y.-H. Chan, V. Madhavan, M. Y. Chou, S.-K. Mo, A.-V. Fedorov, and T.-C. Chiang, *Unique gap structure and symmetry of the charge density wave in single-layer* VSe_2, Phys. Rev. Lett. **121**, 196402 (2018).

[189] N. V. Smith, S. D. Kevan, and F. J. DiSalvo, *Band structures of the layer compounds* $1T$-TaS_2, *and* $2H$-$TaSe_2$, *in the presence of commensurate charge-density waves*, J. Phys. C: Solid State Phys. **18**, 3175 (1985).

[190] D. J. Eaglesham, R. L. Withers, and D. M. Bird, *Charge-density-wave transitions in* $1T$-VSe_2, J. Phys. C: Solid State Phys. **19**, 359–367 (1986).

[191] J.-J. Kim, C. Park, and H. Olin, *A study of charge-density-waves associated with the periodic lattice distortion in* $1T$-VSe_2 *using a low temperature scanning tunneling microscope*, J. Korean Phy. Soc. **31**, 713–716 (1997).

[192] A. Pásztor, A. Scarfato, M. Spera, C. Barreteau, E. Giannini, and C. Renner, *Holographic imaging of the complex charge density wave order parameter*, Phys. Rev. Research **1**, 033114 (2019).

[193] R. V. Coleman, B. Giambattista, P. K. Hansma, A. Johnson, W. W. McNairy, and C. G. Slough, *Scanning tunnelling microscopy of charge-density waves in transition metal chalcogenides*, Adv. Phys. **37**, 559–644 (1988).

[194] B. Giambattista, C. G. Slough, W. W. McNairy, and R. V. Coleman, *Scanning tunneling microscopy of atoms and charge-density waves in* $1T$-TaS_2, $1T$-$TaSe_2$, *and* $1T$-VSe_2, Phys. Rev. B **41**, 10082 (1990).

[195] J. K. Dewhurst, S. Sharma, L. Nordström, F. Cricchio, O. Grånäs, and E. K. U. Gross, The Elk Code, `http://elk.sourceforge.net/` (2019), http://elk.sourceforge.net .

[196] C. S. Yadav and A. K. Rastogi, *Electronic transport and specific heat of* $1T$-VSe_2, Solid State Commun. **150**, 648 (2010).

[197] I. Taguchi, M. Asai, Y. Watanabe, and M. Oka, *Transport properties of iodine-free* $TiSe_2$, Physica B+C **105**, 146 (1981).

[198] D. Zhang, J. Ha, H. Baek, Y. H. Chan, F. D. Natterer, A. F. Myers, J. D. Schumacher, W. G. Cullen, A. V. Davydov, Y. Kuk, M. Y. Chou, N. B. Zhitenev, and J. A. Stroscio, *Strain engineering a* $4a \times \sqrt{3}a$ *charge-density-wave phase in transition-metal dichalcogenide* $1T-VSe_2$, Phys. Rev. Mater. **1**, 1–10 (2017).

[199] A. Migdal, *Interaction between electrons and lattice vibrations in a normal metal*, Sov. Phys. JETP **7**, 996–1001 (1958).

[200] Y. Feng, J. van Wezel, J. Wang, F. Flicker, D. M. Silevitch, P. B. Littlewood, and T. F. Rosenbaum, *Itinerant density wave instabilities at classical and quantum critical points*, Nat. Phys. **11**, 865–871 (2015).

[201] R. Jaramillo, Y. Feng, J. Wang, and T. F. Rosenbaum, *Signatures of quantum criticality in pure Cr at high pressure*, Proc. Natl Acad. Sci. USA **107**, 13631–13635 (2010).

[202] J. C. Campuzano, M. R. Norman, and M. Randeria, Photoemission in the high-T_c superconductors (Springer, Berlin, 2008) Chap. 17.

[203] U. Chatterjee, J. Zhao, M. Iavarone, R. D. Capua, J. P. Castellan, G. Karapetrov, C. D. Malliakas, M. G. Kanatzidis, H. Claus, J. P. C. Ruff, F. Weber, J. v. Wezel, J. C. Campuzano, R. Osborn, M. Randeria, N. Trivedi, M. R. Norman, and S. Rosenkranz, *Emergence of coherence in the charge-density wave state of* $2H$-$NbSe_2$, Nat. Commun. **6**, 6313 (2015).

[204] N. J. Doran, D. Titterington, B. Ricco, M. Schreiber, and G. Wexler, *The electronic susceptibility and charge density waves in 2H layer compounds*, J. Phys. C: Solid State Phys. **11**, 699–705 (1978).

[205] M. Maschek, S. Rosenkranz, R. Heid, A. H. Said, P. Giraldo-Gallo, I. R. Fisher, and F. Weber, *Wave-vector-dependent electron-phonon coupling and the charge-density-wave transition in $TbTe_3$*, Phys. Rev. B **91**, 235146 (2015).

[206] H.-M. Eiter, M. Lavagnini, R. Hackl, E. A. Nowadnick, A. F. Kemper, T. P. Devereaux, J.-H. Chu, J. G. Analytis, I. R. Fisher, and L. Degiorgi, *Alternative route to charge density wave formation in multiband systems*, Proc. Natl. Acad. Sci. U.S.A. **110**, 64–69 (2013).

[207] E. Fawcett, *Spin-density-wave antiferromagnetism in chromium*, Rev. Mod. Phys. **60**, 209 (1988).

[208] F. Weber, S. Rosenkranz, J.-P. Castellan, R. Osborn, R. Hott, R. Heid, K.-P. Bohnen, T. Egami, A. H. Said, and D. Reznik, *Extended phonon collapse and the origin of the charge-density wave in $2H$-$NbSe_2$*, Phys. Rev. Lett. **107**, 107403 (2011).

[209] M. Hossain, Z. Zhao, W. Wen, X. Wang, J. Wu, and L. Xie, *Recent advances in two-dimensional materials with charge density waves: Synthesis, characterization and applications*, Crystals **7**, 298 (2017).

[210] C.-W. Chen, J. Choe, and E. Morosan, *Charge density waves in strongly correlated electron systems*, Rep. Prog. Phys. **79**, 084505 (2016).

[211] C. Steinke, T. O. Wehling, and M. Rösner, *Coulomb-engineered heterojunctions and dynamical screening in transition metal dichalcogenide monolayers*, Phys. Rev. B **102**, 115111 (2020).

[212] K. S. Novoselov, D. Jiang, F. Schedin, T. J. Booth, V. V. Khotkevich, S. V. Morozov, and A. K. Geim, *Two-dimensional atomic crystals*, Proc. Natl. Acad. Sci. U.S.A. **102**, 10451–3 (2005).

[213] L. J. Li, E. C. T. O'Farrell, K. P. Loh, G. Eda, B. Özyilmaz, and A. H. Castro Neto, *Controlling many-body states by the electric-field effect in a two-dimensional material*, Nature **529**, 185–189 (2015).

[214] A. W. Tsen, R. Hovden, D. Wang, Y. D. Kim, J. Okamoto, K. A. Spoth, Y. Liu, W. Lu, Y. Sun, J. C. Hone, L. F. Kourkoutis, P. Kim, and A. N. Pasupathy, *Structure and control of charge density waves in two-dimensional $1T-TaS_2$*, Proc. Natl. Acad. Sci. U.S.A. **112**, 15054–15059 (2015).

[215] S. Gao, F. Flicker, R. Sankar, H. Zhao, Z. Ren, B. Rachmilowitz, S. Balachandar, F. Chou, K. S. Burch, Z. Wang, J. van Wezel, and I. Zeljkovic, *Atomic-scale strain manipulation of a charge density wave*, Proc. Natl. Acad. Sci. U.S.A. **115**, 6986–6990 (2018).

[216] M. Abram, M. Zegrodnik, and J. Spałek, *Antiferromagnetism, charge density wave, and d-wave superconductivity in the extended tJU model: Role of intersite Coulomb interaction and a critical overview of renormalized mean field theory*, JJ. Phys. Condens. Matter **29**, 365602 (2017).

[217] C. J. Butler, M. Yoshida, T. Hanaguri, and Y. Iwasa, *Doublonlike excitations and their phononic coupling in a Mott charge-density-wave system*, Phys. Rev. X **11**, 011059 (2021).

[218] N. Lopes, D. Reyes, M. A. Continentino, and C. Thomas, *Interplay between charge density wave and superconductivity in multi-band systems with inter-band Coulomb interaction*, Phys. Rev. B **103**, 195150 (2021).

[219] X. Xi, L. Zhao, Z. Wang, H. Berger, L. Forró, J. Shan, and K. F. Mak, *Strongly enhanced charge-density-wave order in monolayer $NbSe_2$*, Nat. Nanotechnol. **10**, 765–769 (2015).

[220] S. Barja, S. Wickenburg, Z. F. Liu, Y. Zhang, H. Ryu, M. M. Ugeda, Z. Hussain, Z.-X. Shen, S. K. Mo, E. Wong, M. B. Salmeron, F. Wang, M. F. Crommie, D. F. Ogletree, J. B. Neaton, and A. Weber-Bargioni, *Charge density wave order in 1D mirror twin boundaries of single-layer $MoSe_2$*, Nat. Phys. **12**, 751–756 (2016).

[221] M. Bonilla, S. Kolekar, Y. Ma, H. C. Diaz, V. Kalappattil, R. Das, T. Eggers, H. R. Gutierrez, M.-H. Phan, and M. Batzill, *Strong room-temperature ferromagnetism in VSe_2 monolayers on van der Waals substrates*, Nat. Nanotechnol. **13**, 289–293 (2018).

[222] G. Duvjir, B. K. Choi, I. Jang, S. Ulstrup, S. Kang, T. Thi Ly, S. Kim, Y. H. Choi, C. Jozwiak, A. Bostwick, E. Rotenberg, J.-G. Park, R. Sankar, K.-S. Kim, J. Kim, and Y. J. Chang, *Emergence of a metal–insulator transition and high-temperature charge-density waves in VSe_2 at the monolayer limit*, Nano Lett. **18**, 5432–5438 (2018).

[223] T. T. Ly, G. Duvjir, N. H. Lam, J. Kim, B. K. Choi, and Y. J. Chang, *$\sqrt{3} \times 2$ and $\sqrt{3} \times \sqrt{7}$ charge density wave driven by lattice distortion in monolayer VSe_2*, J. Korean Phys. Soc. **76**, 412–415 (2020).

[224] P. K. J. Wong, W. Zhang, F. Bussolotti, X. Yin, T. S. Herng, L. Zhang, Y. L. Huang, G. Vinai, S. Krishnamurthi, D. W. Bukhvalov, Y. J. Zheng, R. Chua, A. T. N'Diaye, S. A. Morton, C.-Y. Yang, K.-H. Ou Yang, P. Torelli, W. Chen, K. E. J. Goh, J. Ding, M.-T. Lin, G. Brocks, M. P. de Jong, A. H. Castro Neto, and A. T. S. Wee, *Evidence of spin frustration*

in a vanadium diselenide monolayer magnet, Adv. Mater. **31**, 1901185 (2019).

[225] P. M. Coelho, K. Nguyen Cong, M. Bonilla, S. Kolekar, M.-H. Phan, J. Avila, M. C. Asensio, I. I. Oleynik, and M. Batzill, *Charge density wave state suppresses ferromagnetic ordering in VSe_2 monolayers*, J. Phys. Chem. C **123**, 14089–14096 (2019).

[226] R. Chua, J. Yang, X. He, X. Yu, W. Yu, F. Bussolotti, P. K. J. Wong, K. P. Loh, M. B. H. Breese, K. E. J. Goh, Y. L. Huang, and A. T. S. Wee, *Can reconstructed Se-deficient line defects in monolayer VSe_2 induce magnetism?*, Adv. Mater. **32**, 2000693 (2020).

[227] G. Binnig and H. Rohrer, *Scanning tunneling microscopy – from birth to adolescence*, Rev. Mod. Phys. **59**, 615–625 (1987).

[228] B. Voigtländer, *Scanning Probe Microscopy* (Springer, Berlin, Heidelberg, 2015).

[229] C. J. Arguello, S. P. Chockalingam, E. P. Rosenthal, L. Zhao, C. Gutiérrez, J. H. Kang, W. C. Chung, R. M. Fernandes, S. Jia, A. J. Millis, R. J. Cava, and A. N. Pasupathy, *Visualizing the charge density wave transition in $2H$-$NbSe_2$ in real space*, Phys. Rev. B **89**, 235115 (2014).

[230] G. Chen, S. T. Howard, A. B. Maghirang, K. Nguyen Cong, R. A. B. Villaos, L.-Y. Feng, K. Cai, S. C. Ganguli, W. Swiech, E. Morosan, I. I. Oleynik, F.-C. Chuang, H. Lin, and V. Madhavan, *Correlating structural, electronic, and magnetic properties of epitaxial VSe_2 thin films*, Phys. Rev. B **102**, 115149 (2020).

[231] G. Duvjir, B. K. Choi, T. T. Ly, N. H. Lam, K. Jang, D. D. Dung, Y. J. Chang, and J. Kim, *Multiple charge density wave phases of monolayer VSe_2 manifested by graphene substrates*, Nanotechnology **32**, 364002 (2021).

[232] G. Kresse and J. Furthmüller, *Efficient iterative schemes for ab initio total-energy calculations using a plane-wave basis set*, Phys. Rev. B **54**, 11169–11186 (1996).

[233] J. P. Perdew, K. Burke, and M. Ernzerhof, *Generalized Gradient Approximation made simple*, Phys. Rev. Lett. **77**, 3865–3868 (1996).

[234] F. Li, K. Tu, and Z. Chen, *Versatile electronic properties of VSe_2 bulk, few-layers, monolayer, nanoribbons, and nanotubes: A computational exploration*, J. Phys. Chem. C **118**, 21264–21274 (2014).

[235] J. Feng, D. Biswas, A. Rajan, M. D. Watson, F. Mazzola, O. J. Clark, K. Underwood, I. Marković, M. McLaren, A. Hunter, D. M. Burn, L. B. Duffy, S. Barua, G. Balakrishnan, F. Bertran, P. Le Fèvre, T. K. Kim,

G. van der Laan, T. Hesjedal, P. Wahl, and P. D. C. King, *Electronic structure and enhanced charge-density wave order of monolayer VSe_2*, Nano Lett. **18**, 4493–4499 (2018).

[236] Y. Umemoto, K. Sugawara, Y. Nakata, T. Takahashi, and T. Sato, *Pseudogap, Fermi arc, and Peierls-insulating phase induced by 3D–2D crossover in monolayer VSe_2*, Nano Research **12**, 165–169 (2019).

[237] D. Biswas, A. J. H. Jones, P. Majchrzak, B. K. Choi, T.-H. Lee, K. Volckaert, J. Feng, I. Marković, F. Andreatta, C.-J. Kang, H. J. Kim, I. H. Lee, C. Jozwiak, E. Rotenberg, A. Bostwick, C. E. Sanders, Y. Zhang, G. Karras, R. T. Chapman, A. S. Wyatt, E. Springate, J. A. Miwa, P. Hofmann, P. D. C. King, Y. J. Chang, N. Lanata, and S. Ulstrup, *Ultrafast triggering of insulator-metal transition in two-dimensional VSe_2*, Nano Lett. **21**, 1968–1975 (2021).

[238] M. J. Trott and C. A. Hooley, Can Fermi surface nesting alone drive the charge-density-wave transition in monolayer vanadium diselenide? (2020), arXiv:2004.06665 [cond-mat.str-el] .

[239] P. Nozieres, *Theory Of Interacting Fermi Systems* (Westview Press, New York, 1964).

[240] A. K. Geim and I. V. Grigorieva, *van der Waals heterostructures*, Nature **499**, 419–425 (2013).

[241] K. S. Novoselov, A. Mishchenko, A. Carvalho, and A. H. Castro Neto, *2D materials and van der waals heterostructures*, Science **353**, aac9439 (2016).

[242] J. Zaanen, Y. Liu, Y.-W. Sun, and K. Schalm, *Holographic duality in condensed matter physics* (Cambridge University Press, 2015).

[243] J. Thomson, *Cathode rays*, Lond. Edinb. Dublin Philos. Mag. J. Sci. **44**, 293–316 (1897).